Distribution Agreement

In presenting this thesis or dissertation as a partial fulfillment of the requirements for an advanced degree from Emory University, I hereby grant to Emory University and its agents the non-exclusive license to archive, make accessible, and display my thesis or dissertation in whole or in part in all forms of media, now or hereafter known, including display on the world wide web. I understand that I may select some access restrictions as part of the online submission of this thesis or dissertation. I retain all ownership rights to the copyright of the thesis or dissertation. I also retain the right to use in future works (such as articles or books) all or part of this thesis or dissertation.

Signature:

_____ _____

Mallory L. Green Date

Understanding the Chemistry of Beryllium Using Velocity Map Imaging Spectroscopy

By

Mallory L. Green

Doctor of Philosophy

Chemistry

Michael C. Heaven, Ph.D.
Advisor

Francesco Evangelista, Ph.D.
Committee Member

Tianquan Lian, Ph.D.
Committee Member

Accepted:

Dean of the Graduate School
Lisa A. Tedesco, Ph.D.

Date

Understanding the Chemistry of Beryllium Using Velocity Map Imaging Spectroscopy

By

Mallory L. Green

B.S., Georgia Southern University, 2014

Advisor: Michael C. Heaven, Ph.D.

An abstract of
A dissertation submitted to the Faculty of the
James T. Laney School of Graduate Studies of Emory University
in partial fulfillment of the requirements for the degree of
Doctor of Philosophy
in Chemistry
2020

Abstract

Understanding the Chemistry of Beryllium Using Velocity Map Imaging Spectroscopy

By: Mallory L. Green

Contrary to its small size, beryllium has been known to participate in anomalous bonding, which disregards periodic trends and can present numerous theoretical challenges. Due to toxicity concerns, experimental study of beryllium has historically been avoided. However, here we present the use of a photoelectron velocity map imaging spectrometer, used to provide new information about previously unexplored beryllium containing anions. For all anions studied, neutral electron affinities and anion spectroscopic constants were established and the experimental results were found to be in good agreement with our *ab initio* calculations.

Each of the species described, herein, exhibited unusual bonding behavior, expected of beryllium species: BeO^- and BeS^- were found to sustain a dipole bound excited state, a state where the parent molecule experiences long range attractions to the departing electron, to form a bound state 100-200 cm^{-1} below the threshold of electron detachment. The BeF^- anion demonstrated beryllium's Lewis acidity and ability to participate in closed shell bonding, as the strong dative bond ($D_0^- > 28460$ cm^-) between Be ($^1S_0$) and F^- ($^1S_0$) was found to be supported by back donation of electron density from the F^- to the Be. Also, the confirmation of the ground state geometry of BeC_2 and BeC_2^- (T-shaped) demonstrated propensity for covalent bonding of beryllium, even as a metal, as the bond between the Be and C_2 subunit, in both molecules, was found to be polar covalent with strong electrostatic contributions.

Other small beryllium containing anions, as well as, thorium oxide clusters ($Th_nO_m^-$) were explored using our velocity map instrument. However, resolved spectra could not be obtained for these species. Indications of hot source conditions, are believed to be hindering the elucidation of spectra for more electronically complicated species. Inclusion of a cold trap to the instrument will improve resolution for these species, as well as pave the way for studying Be_n and Be_n^- clusters.

Understanding the Chemistry of Beryllium Using Velocity Map Imaging Spectroscopy

By

Mallory L. Green

B.S., Georgia Southern University, 2014

Advisor: Michael C. Heaven, Ph.D.

A dissertation submitted to the Faculty of the
James T. Laney School of Graduate Studies of Emory University
in partial fulfillment of the requirements for the degree of
Doctor of Philosophy
in Chemistry
2020

Acknowledgements

To my family, thank you for giving me a healthy self-esteem and sense of optimism to push through the lows and aim for high achievements.

To my friends and lab mates, thank you for you companionship and providing advice and laughter over the years.

To my husband, thank you for your love and support. I could not get where I'm going without you to lean on.

And to my advisor, Dr. Heaven, thank you for your mentorship and flexibility. I would not be the scientist I am today without your guidance over the past five years.

Table of Contents

List of Figures

List of Tables

Chapter 1

Introduction

1.1 The Chemistry of Beryllium

An understanding of the chemistry of beryllium has been a sought after endeavor for many decades. Interest in this element flourished with the pursuit of comprehending the evolution of metallic clusters from the single molecule to the bulk phase. [1-8] Propelled by the advent of nanomaterials, there was, and still is, a desire to determine the onset of metallic behavior in metal containing clusters. By evaluating the changes in geometry, bond energies, and the HOMO-LUMO energy gap, it is possible to define the inception of metallic character. [1]

Beryllium and Be_n (n = 2,3,4,...) clusters were expected to be an ideal candidate for studying metallic evolution. Given beryllium has only four electrons, it can easily be treated with a nonrelativistic Hamiltonian, suggesting theoretical analysis of beryllium containing molecules would be relatively straightforward. Also, due to it's small atomic size, Be_n clusters can be studied through spectroscopic methods with enough resolution to provide geometric information.

The evolution of behavior in beryllium clusters is believed to be non-monatomic, given the bond energy of the simplest pure beryllium cluster, the beryllium dimer (Be_2) has been experimentally determined to be quite weak ($D_e = 929.7 \pm 2.0$ cm^{-1}), [9] whereas the melting point of bulk beryllium metal is quite high (1287 °C), indicating a much stronger bond between beryllium atoms. Theoretical work on the small Be_n clusters (n= 2-6) has demonstrated an increase in average bond dissociation energy with increase in cluster size. [1-3,6] This correlation was attributed to an increase in many-body interactions within the larger cluster sizes. Additionally, an increase in sp hybridization for the larger clusters was evident. [1]

Hybridization is a common phenomenon for beryllium-containing molecules, due to the near degeneracy of the 2s and 2p atomic orbitals of the beryllium atom. Hybridization enables this effectively closed shell species to engage in covalent bonding. Due to beryllium's high

ionization energy and small atomic radius, the degree of this covalency is often much higher than its Group IIA counterparts. For example, of the Group IIA hydroxides (MOH), only beryllium hydroxide (BeOH) exhibits a bent geometric structure, indicating covalent bond participation. [10] The other alkaline earth hydroxides exhibit a linear structure (Mg being quasilinear), indicative of ionic bonding of the form $M^{+}(OH)^{-}$.

Due to beryllium's unique characteristics, it has been known to participate in numerous anomalous bonds, which are, also, of considerable theoretical and experimental interest. Beryllium has been shown to be a strong Lewis acid, leading to predictions of beryllium containing molecules, like BeO, to be able to bond noble gases. [11,12] It has also been thoroughly investigated for the binding and storage of transient molecules, CO and H_2. [13-17] Also, it's Lewis acidity is thought to provide acidity enhancement to some species, to modulate reactivity. [18-21] Because beryllium is able to accommodate extra electron density within its 2p orbitals, there have been recent studies investigating the possibility of this element forming double and triple bonds, which has not been shown for any other s-block metal. [22-24] Additionally, beryllium is being pursued as a building block for a new class of "super" molecules, known as superhalogens. [25-26]

Despite the numerous theoretical work that has been attempted in elucidating the chemistry of this element, one concern has been revealed: Although beryllium appears to be a simple system for theoretical investigation, it suffers complications which prevent a straightforward analysis, such as static and dynamic correlation effects. Static correlation arises from the mixing of determinants to fully describe the wavefunction (Ψ) of the molecule, whereas

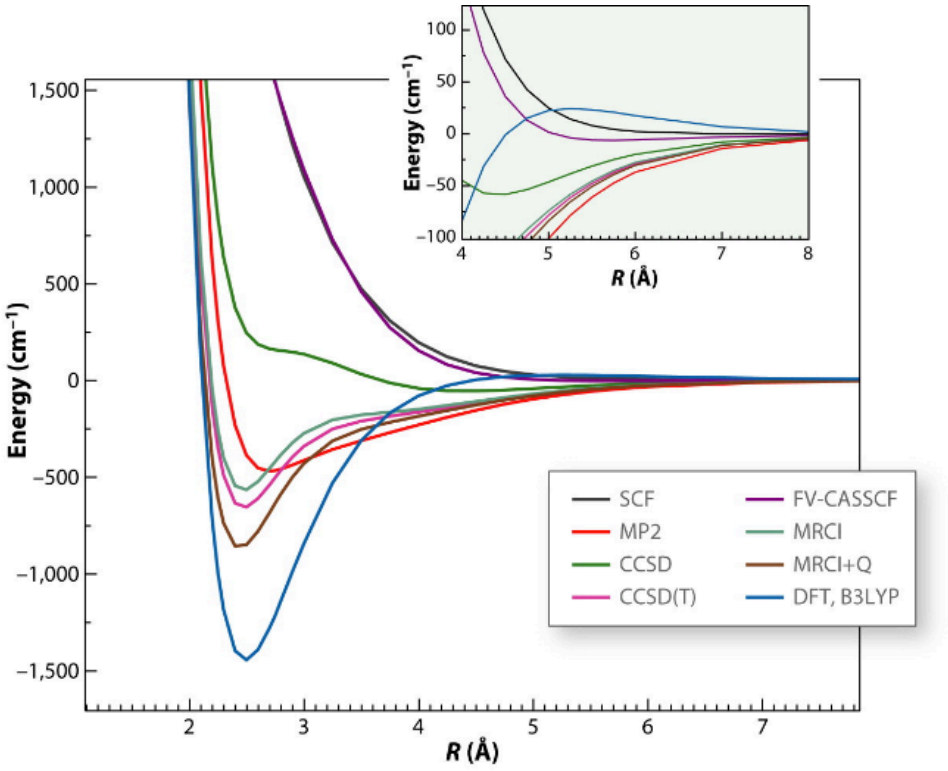

Heaven MC, et al. 2011.
Annu. Rev. Phys. Chem. 62:375–93

Figure 1.1. Potential Energy Curves (PECs) of the Be_2 dimer, at different levels of theory, using a consistent basis set. Reprinted from Ref [1]

dynamic correlation describes the movement of electrons to avoid interactions with other electrons. Both forms of correlation require treatment beyond the Hartree Fock level, increasing the difficulty of characterizing molecules containing this element.

The need for correlation treatment has been determined to be necessary for even the smallest beryllium species. The Be_2 dimer is an example of a deceptively simple beryllium molecule, containing only 4 valence electrons, which has a history of disagreement among theoretical chemists regarding the nature of its bond. [10, 28-31] Initially, all the Group IIA dimers were thought to be unbound, due to their atomic closed shell nature. However, the discovery of Mg_2 by Balfour and Douglas in 1970 sparked the search for the other homonuclear alkaline earth

dimers. [10] It was initially assumed that the Group IIA elements would follow the bond energy trend of their more purely covalent counterparts in Group IA. The alkali metals (Li-Cs) showed a clear increase in dissociation energy (D_e) with increase in atomic number. The experimental determination of the dissociation energy of Ca_2 (D_e = 1095.0 cm^{-1}) supported this hypothesis, as the dissociation energy of Mg_2 was much lower (D_e = 403.0 cm^{-1}) . Given the low dissociation energy of Mg_2 with respect to Ca_2, it was expected that Be_2 would be an unbound system.

At first, lower level calculations seemed to support this theory, as Be_2 was predicted to be unbound at the Self Consistent Field (SCF) level of theory. [1] However, as higher levels of theory began to be employed to characterize Be_2, it was clear conclusions about the nature of the Be_2 bond were not as unambiguous as expected. Figure 1.1 shows the predicted potential energy curve of Be_2 at various levels of theory, using an identical basis set. As previously stated, SCF, as well as the configuration interaction method (CI), FV-CASSCF (full valence-complete active space SCF), predict the ground state of Be_2 to be unbound. The pertubative Møller-Plesset method (MP2), and the coupled cluster method with single and double excitations (CCSD) show a stronger interaction, albeit still weak, suggesting a van der Waals interaction between the two atoms, similar to the noble gas dimers. The higher level methods, coupled cluster with pertubative triples (CCSD(T)), multireference configuration interaction (MRCI) and MRCI with Davidson correction (MRCI+Q), all predict a bound ground state of Be_2. Comparison to the, long awaited, experimental determination of the dissociation energy of ground state of Be_2 (D_e = 929.7 ± 2 cm^{-1}), confirmed the MRCI+Q prediction was the most accurate.

It is important to note the performance of Density Functional Theory (DFT) for studying beryllium clusters, as it will be necessary to employ more cost effective theoretical methods to the understanding of metallic clusters as cluster size increases. As demonstrated in Figure 1.1,

DFT accurately predicts the ground state geometry of Be_2, but greatly overestimates the D_e. This circumstance of proper prediction of geometries, but overestimation of the bond energy by DFT was also found for Be_2^+, Be_3, Be_4, and Be_5. However, there are indications that DFT methods begin to perform better with larger cluster sizes. [1, 32]

The varied results of different theoretical methods, as shown in Figure 1.1, make evident that the study of the bonding in Be_2 is very sensitive to correlation treatment. Other small beryllium molecules have exhibited similar sensitivities. Beryllium monocarbide, BeC, is known to have a very multiconfigurational ground state. [10] BeOBe is another case of closed shell species (Be and BeO) interacting. This molecule's ground state assignment of either singlet or triplet depends heavily on the theoretical method used. [10] Also, BeH^- is well defined by a single determinant at its equilibrium point, and its dissociation limit. However, BeH^- has midrange multiconfigurational character, due to the switch of localization of the extra electron, on the beryllium atom at the point of association (HBe^-) and on the hydrogen atom at the point of dissociation ($Be + H^-$) . [33] The theoretical challenges encountered while studying these small molecules have brought the field a new motivation: Beryllium-containing molecules can be used to refine current high level theoretical techniques, in terms of correlation treatment, without further complications, such as relativistic effects, given their small size.

In order to use beryllium molecules to verify the robust nature of theoretical techniques, it is necessary to provide experimental confirmation of the electronic structure of such molecules. Experimental studies of beryllium species are often limited due to the toxicity of this metal, which makes handling of the material quite intimidating. Few experimental studies have been conducted on beryllium containing species. Those limited studies include mass spectrometry studies, [34] matrix isolation studies, [11,12] and gas phase studies of neutral and cationic

beryllium molecules. [9,10] Although mass spectrometry allows us to see what kind of clusters we are able to form, unless it is coupled to a spectroscopic technique, we are not provided any energetic information of our molecules. Many have been successful in generating small beryllium containing molecules in rare gas matrices. [11,12] However, due to interactions that can occur between the molecule of interest and the matrix environment, experimental results can be skewed from their true "isolated" behavior, limiting the comparison to *ab initio* methods. Also, matrices are known to inhibit the rotation of molecules confined within the matrix. Rotational restriction limits the amount of geometric information that can be gathered about the probed molecule.

Gas phase studies of beryllium containing molecules are the most appropriate for direct comparison to theoretical methods. Successful cases include stimulated emission pumping (SEP) to determine the D_0 of Be_2 [9] and laser induced fluorescence (LIF) of BeOBe to confirm the ground state assignment of $^1\Sigma^+$. [10] Also, pulsed field ionization- zero electron kinetic energy (PFI-ZEKE) photoelectron spectroscopy has been used to determine the ionization energy of the Be_2 neutral molecule, and provided accurate spectroscopic constants of the cation, Be_2^+. [1] There has been almost no work conducted on beryllium anions in the gas phase.

The limitations of conducting these gas phase studies are often mass selectivity, and spectral congestion due to density of states. In the study of neutral species, it is impossible to separate the different neutral molecules, without ionization to form charged species, which can then be mass separated using electric fields. However, ionization often prevents spectroscopic analysis of the parent neutral species. Also, many of these spectroscopic methods require excitation into higher excited states for characterization. As the cluster size increases, so does the number of states. It can, therefore, become very difficult to deconvolute the spectra of more

complicated molecules. A spectroscopic technique that can circumvent these pitfalls is anion photoelectron velocity map imaging spectroscopy (aPES-VMI).

1.2 Advent of Photoelectron Velocity Map Imaging Spectroscopy

Velocity map imaging spectroscopy of anions is a high resolution variant of anion photoelectron spectroscopy (aPES). In aPES, mass selected anions are intercepted using a fixed frequency laser. If the photon energy of the laser (hν) exceeds the binding energy of the electron (eBE), the electron will be photodetached, leaving behind a neutral molecule:

$$A^- \xrightarrow{h\nu} A + e^- \qquad \text{Equation 1.1}$$

Due to conservation of energy, the energy not absorbed by the anion to induce photodetachment is imparted to the leaving electron as kinetic energy (eKE):

$$eKE = h\nu - eBE \qquad \text{Equation 1.2}$$

By recording the eKE of the detached electron, Equation 1.2 can be rearranged in order to determine the eBE, giving the transition energy for $A^- \rightarrow A$. The resulting information provides the electron affinity (EA) of the neutral species, information about electronically excited states, and in best case scenarios, vibrational information. An electronic scheme of this process can be found in Figure 1.2.

Anion PES is a very robust experimental technique. Given its feasibility is only restricted by the ability of the molecule of interest to initially form an anion, and the accessibility of the EA of the molecule by conventional lasers, it has been used to explore a range of systems, including biomolecules, [36-38] neutral transition states, [39,40] and size-selected clusters. [41-45] Although this technique's versatility is immense, it has been known to suffer from poor collection efficiencies, and poor resolution.

The first aPES experiments were conducted using a intracavity, continuous wave (cw) Ar laser, with a hemispherical energy analyzer to measure the eKE. [46-48] Although this experiment's flexibility to coupling with numerous ion sources was useful in determining the EA's for many small species, it was limited by the photon energy produced by the laser. When

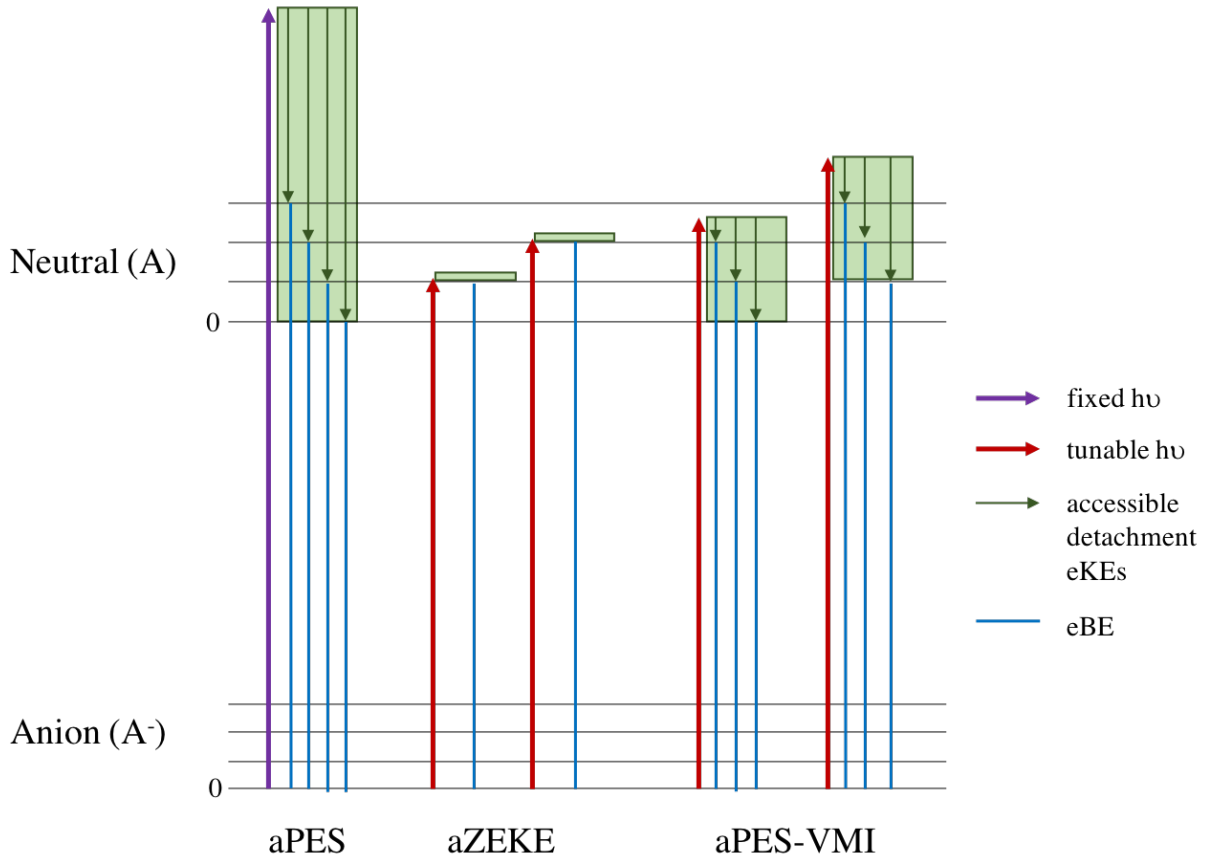

Figure 1.2. Energy diagram of the aPES, aZEKE, and aPES-VMI

pulsed laser systems producing higher energy photons became available, the field of photoelectron spectroscopy expanded, and time of flight (TOF) detection became popular. Both field free TOF and magnetic bottle TOF were used to record electrons upon detachment. [49,50] Field free TOF provided reasonable resolution (5-10 meV), but only a small fraction of the photodetached electrons were recorded, leading to very low collection efficiencies. Magnetic bottle TOF collected a wider angular distribution of photoelectrons produced, but the decrease in

resolution due to Doppler broadening could produce features with resolution as low as in the keV range.

The significant increase in resolution for neutral species using a new technique known as zero electron kinetic energy (ZEKE) spectroscopy, sparked the search for a similar method for the use of anions, known as anion ZEKE (aZEKE). In aZEKE, an anion is mass selected and intercepted with the output of a pulsed laser. Instead of using a single photon energy well above the threshold of detachment for all detachment channels, as is used for aPES, aZEKE uses a tunable laser source that can be stepped in very small increments (see Figure 1.2). Like aPES, when the anion packet is intercepted by the laser, electrons are photodetached, but in aZEKE, there is a time delay to allow for the spatial separation of electrons of different eKEs. Only electrons with eKEs near zero remain in the interaction region, where after the time delay, a pulsed field is applied to extract the ZEKE electrons for detection. Only when the scanning laser is resonant with a transition from the anion to the neutral species will photoelectron signal detected. Given the very narrow eKE range detected in a single experimental shot, the resolution of aZEKE can be as high as 1 cm^{-1}, a factor of 40 times better than the best aPES experiments mentioned earlier.[51]

Although the improvement in resolution of aZEKE over aPES was a major step forward in the field, there were a few drawbacks to this technique. As previously mentioned, the photodetachment laser is required to be scanned over a long energy range at very small energy intervals. Therefore, in order to produce a full spectrum, acquisition times can be very long. Also, electrons with eKE near zero are susceptible to distortion by stray electric and magnetic fields, leading to experimental difficulties. Finally, aZEKE is limited in its versatility, due to

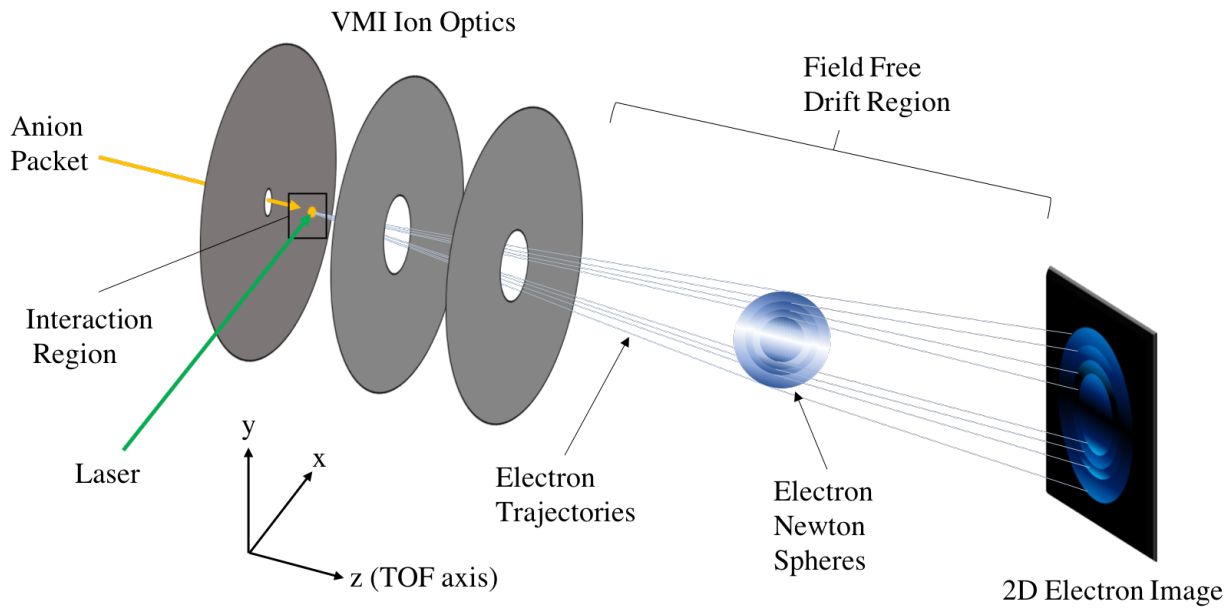

Figure 1.3. Velocity map imaging optical setup.

restrictions to the types of photodetachment processes it can undergo. In aZEKE, the cross section for photodetachment (σ) is constrained by the Wigner Threshold Law:

$$\sigma \propto (eKE)^{l+1/2} \qquad \text{Equation 1.3}$$

where l is the angular momentum of the photodetached electron, with electron kinetic energy given by eKE. In aZEKE, the eKE of the detected electron is approximately zero. Therefore, the photodetachment cross section will be negligible for any detachment process, other than where l=0 (ie. s wave detachment of the electron). For any detachment processes with p-wave or d-wave type photodetachment, aZEKE cannot be used.[51]

Velocity map imaging spectroscopy of anions is a technique known to be able to produce the resolution of aZEKE, with the flexibility of aPES. [51,52] Velocity map imaging ion optics were first pioneered by Eppink and Parker in 1997. [53] A typical velocity map imaging scheme, modelled after Eppink's and Parker's original design, is shown in Figure 1.3. The VMI ion optics consist of a set of 3 disks (electrodes). The back two electrodes are held at a negative voltage,

and the front electrode is grounded. The mass selected anions float into the interaction region, where they are intercepted by a pulsed laser. Electrons are photodetached and extracted down the TOF axis. The equipotential surface created by the varied voltages of the electrodes causes the electrons of differing velocities to spatially separate in velocity space, as they travel down the TOF axis. As the electrons travel down the drift region, they form nested spheres, known as Newton spheres, where each sphere consists of electrons of the same velocity. As the electrons continue to travel, the radial separation between spheres increases, until the electron packet is focused onto a 2-dimensional position sensitive detector. The resulting detector image is a set of concentric rings, where the radius of a given ring (R_i) is related to the velocity of the incident electron packet (v_i) by:

$$R_i = N v_i t \qquad \text{Equation 1.4}$$

where N is a magnification factor and t is the time of flight of the electron packet. Given the kinetic energy equation,

$$KE = \frac{1}{2} m v^2 \qquad \text{Equation 1.5}$$

it is possible to determine the relationship between eKE and the radius of a ring projected onto the detector. Therefore, the innermost ring is comprised of electrons with the slowest velocities and lowest eKE's, and the outermost ring is comprised of electrons with the fastest velocities and highest eKE's. The end result is a method of separating eKE's spatially as opposed to temporally, which leads to a higher resolution detection of molecular transitions.

Due to the position sensitivity of the VMI detection method, it is also possible to extract information about the photoelectrons' angular distributions (PADs). A PAD is a function of the electron distribution, or signal intensity (I), at an angle, θ, with respect to the polarization axis of the photodetachment light given by:

$$I(\theta) = \frac{\sigma}{4\pi} * (1 + \beta P_2(cos\theta)) \qquad \text{Equation 1.6}$$

where σ is the photodetachment cross section, $P_2(cos\theta)$ is the second-order Legendre polynomial, and β is an anisotropy parameter ranging from $\beta = -1$ for a PAD with peak intensity perpendicular to the photon polarization, and $\beta = 2$ for a PAD with peak intensity parallel to the photon polarization. An electron is detached from an orbital of angular momentum, l, as a superposition of spherical harmonic partial waves with $\Delta l = \pm 1$. The PAD is a representation of the interference of these partial waves, and can, therefore, be used to exact information about the angular momentum of the parent molecule.

In comparing VMI techniques with other experimental methods, VMI offers many advantages. Collection efficiencies of VMI experiments are ~100%, surpassing the high resolution aPES TOF methods. Selection rules are relaxed due to conservation of energy by the electron (ie. no need for electronic selection rules), and the eKE for a given transition can be adjusted through tuning the photon energy to avoid complications with the Wigner threshold law. Energy resolution for a simple 3-electrode VMI set up (as shown in Fig. 1.3) has been determined to be a function of the eKE, as $\frac{\Delta eKE}{eKE} = 3\%$, leading to a resolution limit for slow moving electrons of a few wavenumbers.

Additionally, the field of VMI imaging continues to grow, as new techniques are developed to further improve the resolution of the instrumentation. Many scientists have transitioned from the original 3-electrode VMI design, to an electrode scheme incorporating more charged plates, to further improve focusing of the quantized eKE's onto the detector. [54] As the resolution of the final spectrum is a function of the eKE of detached electron's the Neumark group at Berkley university uses low extraction voltages and images only slow moving electrons (<1000 cm^{-1}) in small energy intervals to form a final composite high resolution spectrum in a

technique known as slow electron velocity map imaging (SEVI). [51] Furthermore, resolution has been improved with the inclusion of cryogenic cooling of anions before detachment. [55] The incorporation of these improvements should only make the study of clusters with high density of states more accessible.

1.3 Chapter 1 References

(1) Heaven, M. C.; Merritt, J. M.; Bondybey, V. E., Bonding in Beryllium Clusters. In *Annual Review of Physical Chemistry, Vol 62*, Leone, S. R.; Cremer, P. S.; Groves, J. T.; Johnson, M. A., Eds. 2011; Vol. 62, pp 375-393.

(2) Ascik, P. N.; Wilke, J. J.; Simmonett, A. C.; Yamaguchi, Y.; Schaefer, H. F., The Beryllium tetramer: Profiling an elusive molecule. *Journal of Chemical Physics* **2011,** *134* (7).

(3) Ascik, P. N.; Rugango, R.; Simmonett, A. C.; Compaan, K. R.; Schaefer, H. F., The Beryllium Pentamer: Trailing an Uneven Sequence of Dissociation Energies. *Chemphyschem* **2012,** *13* (5), 1255-1260.

(4) Fioressi, S. E.; Binning, R. C.; Bacelo, D. E., Structures and energetics of BenCn (n=1-5) and Be2nCn (n=1-4) clusters. *Chemical Physics* **2014,** *443*, 76-86.

(5) Huran, A. W.; Ben Amor, N.; Evangelisti, S.; Hoyau, S.; Leininger, T.; Brumas, V., The Electronic Structure of Beryllium Chains. *Journal of Physical Chemistry A* **2018,** *122* (24), 5321-5332.

(6) Kalemos, A., The nature of the chemical bond in Be-2(+), Be-2, Be-2(-), and Be-3. *Journal of Chemical Physics* **2016,** *145* (21).

(7) Martin-Somer, A.; Lamsabhi, A.; Mo, O.; Yanez, M., The importance of deformation on the strength of beryllium bonds. *Computational and Theoretical Chemistry* **2012,** *998*, 74-79.

(8) Sanchez-Castro, M. E.; Sanchez-Vazquez, M., Structure and reactivity of Be-n cycles (n=3-12): A DFT study. *Computational and Theoretical Chemistry* **2011,** *967* (1), 136-139.

(9) Merritt, J. M.; Bondybey, V. E.; Heaven, M. C., Beryllium Dimer-Caught in the Act of Bonding. *Science* **2009,** *324* (5934), 1548-1551.

(10) Heaven, M. C.; Bondybey, V. E.; Merritt, J. M.; Kaledin, A. L., The unique bonding characteristics of beryllium and the Group IIA metals. *Chemical Physics Letters* **2011,** *506* (1-3), 1-14.

(11) Zhang, Q. N.; Chen, M. H.; Zhou, M. F.; Andrada, D. M.; Frenking, G., Experimental and Theoretical Studies of the Infrared Spectra and Bonding Properties of NgBeCO(3) and a Comparison with NgBeO (Ng = He, Ne, Ar, Kr, Xe). *Journal of Physical Chemistry A* **2015,** *119* (11), 2543-2552.

(12) Wang, Q.; Wang, X. F., Infrared Spectra of NgBeS (Ng = Ne, Ar, Kr, Xe) and BeS2 in Noble-Gas Matrices. *Journal of Physical Chemistry A* **2013,** *117* (7), 1508-1513.

(13) Allouche, A., Carbon monoxide adsorption on beryllium surfaces. *Surface Science* **2013,** *608*, 265-274.

(14) Beheshtian, J.; Ravaei, I., Toxic CO detection by Li-encapsulated fullerene-like BeO. *Structural Chemistry* **2018,** *29* (1), 231-241.

(15) Deshmukh, A.; Konda, R.; Titus, E.; Chaudhari, A., Electronic structure calculations and molecular dynamics simulations of hydrogen adsorption on Beryllium doped complexes. *International Journal of Hydrogen Energy* **2017,** *42* (37), 23708-23715.

(16) Naumkin, F. Y.; Wales, D. J., Trapping of hydrogen atoms inside small beryllium clusters and their ions. *Chemical Physics Letters* **2016,** *659*, 282-288.

(17) Shinde, R.; Tayade, M., Remarkable Hydrogen Storage on Beryllium Oxide Clusters: First-Principles Calculations. *Journal of Physical Chemistry C* **2014,** *118* (31), 17200-17204.

(18) Albrecht, L.; Boyd, R. J.; Mo, O.; Yanez, M., Changing Weak Halogen Bonds into Strong Ones through Cooperativity with Beryllium Bonds. *Journal of Physical Chemistry A* **2014,** *118* (23), 4205-4213.

(19) Mo, O.; Yanez, M.; Alkorta, I.; Elguero, J., Spontaneous proton transfers induced by beryllium bonds. *Molecular Physics* **2014,** *112* (5-6), 592-600.

(20) Montero-Campillo, M. M.; Sanz, P.; Mo, O.; Yanez, M.; Alkorta, I.; Elguero, J., Alkaline-earth (Be, Mg and Ca) bonds at the origin of huge acidity enhancements. *Physical Chemistry Chemical Physics* **2018,** *20* (4), 2413-2420.

(21) Valadbeigi, Y.; Rouhani, M., Borane and beryllium derivatives of sulfuric and phosphoric acids: Strong inorganic acids. *Computational and Theoretical Chemistry* **2019,** *1164*.

(22) Rohman, S. S.; Kashyap, C.; Ullah, S. S.; Guha, A. K.; Mazumder, L. J.; Sharma, P. K., Ultra-Weak Metal-Metal Bonding: Is There a Beryllium-Beryllium Triple Bond? *Chemphyschem* **2019,** *20* (4), 516-518.

(23) Liu, X. M.; Zhang, M.; Yu, S.; Geng, Y.; Zhang, X. X.; Ding, Y. H.; Su, Z. M., Beryllium-beryllium double-pi bonds in the octahedral cluster of Be-2(mu(2)-X)(4) (X = Li, Cu, BeF). *Physical Chemistry Chemical Physics* **2018,** *20* (37), 23898-23902.

(24) Villanueva, E. F.; Mo, O.; Yanez, M., On the existence and characteristics of pi-beryllium bonds. *Physical Chemistry Chemical Physics* **2014,** *16* (33), 17531-17536.

(25) Anusiewicz, I.; Skurski, P., An ab initio study on BeX3- superhalogen anions (X = F, Cl, Br). *Chemical Physics Letters* **2002,** *358* (5-6), 426-434.

(26) Elliott, B. M.; Koyle, E.; Boldyrev, A. I.; Wang, X. B.; Wang, L. S., MX3- superhalogens (M = Be, Mg, Ca; X = Cl, Br): A photoelectron spectroscopic and ab initio theoretical study. *Journal of Physical Chemistry A* **2005,** *109* (50), 11560-11567.

(27) Deible, M. J.; Kessler, M.; Gasperich, K. E.; Jordan, K. D., Quantum Monte Carlo calculation of the binding energy of the beryllium dimer. *Journal of Chemical Physics* **2015,** *143* (8).

(28) El Khatib, M.; Bendazzoli, G. L.; Evangelisti, S.; Helal, W.; Leininger, T.; Tenti, L.; Angeli, C., Beryllium Dimer: A Bond Based on Non-Dynamical Correlation. *Journal of Physical Chemistry A* **2014,** *118* (33), 6664-6673.

(29) El Khatib, M.; Bendazzoli, G. L.; Evangelisti, S.; Helal, W.; Leininger, T.; Tenti, L.; Angeli, C., Beryllium Dimer: A Bond Based on Non-Dynamical Correlation. *Journal of Physical Chemistry A* **2014,** *118* (33), 6664-6673.

(30) Koput, J., The ground-state potential energy function of a beryllium dimer determined using the single-reference coupled-cluster approach. *Physical Chemistry Chemical Physics* **2011,** *13* (45), 20311-20317.

(31) Lesiuk, M.; Przybytek, M.; Balcerzak, J. G.; Musial, M.; Moszynski, R., Ab initio Potential Energy Curve for the Ground State of Beryllium Dimer. *Journal of Chemical Theory and Computation* **2019,** *15* (4), 2470-2480.

(32) Xu, L.; Xu, Y. Q.; Cheung, N. H.; Wong, K. Y., Practical approach for beryllium atomic clusters: TD-DFT potential energy surfaces from equilibrium to dissociation for excited states of 2s -> 2p. *Theoretical Chemistry Accounts* **2018,** *137* (10).

(33) Verdicchio, M.; Bendazzoli, G. L.; Evangelisti, S.; Leininger, T., Surprising Electronic Structure of the BeH- Dimer: a Full-Configuration-Interaction Study. *Journal of Physical Chemistry A* **2013,** *117* (1), 192-199.

(34) Fu, Y. C.; Zhang, L.; Zhou, W. J.; Zhao, X. L.; Wu, Z. K.; Zhao, G. Q.; Liu, Q.; Lu, X. F.; Zhao, W. N.; Huang, C. H., A preliminary study of direct Be-10(2+) counting in AMS using the super-halogen anion BeF3. *Nuclear Instruments & Methods in Physics Research Section B-Beam Interactions with Materials and Atoms* **2015,** *361*, 207-210.

(35) Markovich, G.; Pollack, S.; Giniger, R.; Cheshnovsky, O. J. Chem. Phys. 1994, 101, 9344.

(36) Castleman, A. W., Jr.; Bowen, K. H., Jr J. Phys. Chem. 1996, 100, 12911.

(37) Hendricks, J. H.; Lyapustina, S. A.; Declercq, H. L.; Snodgrass, J. T.; Bowen, K. H. J. Chem. Phys. 1996, 104, 7788.

(38) Schiedt, J.; Weinkauf, R.; Neumark, D. M.; Schlag, E. W. Chem. Phys. 1998, 239, 511.

(39) Polanyi, J. C.; Zewail, A. H. Acc. Chem. Res. 1995, 28, 119.

(40) Neumark, D. M. Phys. Chem. Chem. Phys. 2005, 7, 433.

(41) Cheshnovsky, O.; Yang, S. H.; Pettiette, C. L.; Craycraft, M. J.; Liu, Y.; Smalley, R. E. Chem. Phys. Lett. 1987, 138, 119.

(42) Gantefor, G.; Gausa, M.; Meiwesbroer, K. H.; Lutz, H. O. Faraday Disc. 1988, 197.

(43) Handschuh, H.; Cha, C. Y.; Bechthold, P. S.; Gantefor, G.; Eberhardt, W. J. Chem. Phys. 1995, 102, 6406.

(44) Wu, H. B.; Desai, S. R.; Wang, L. S. Phys. ReV. Lett. 1996, 77, 2436.

(45) Busani, R.; Folkers, M.; Cheshnovsky, O. Phys. ReV. Lett. 1998, 81, 3836.

(46) Brehm, B.; Gusinow, M. A.; Hall, J. L., ELECTRON AFFINITY OF HELIUM VIA LASER PHOTODETACHMENT OF ITS NEGATIVE ION. *Physical Review Letters* **1967,** *19* (13), 737-&.

(47) Kasdan, A.; Lineberger, W. C., ALKALI-METAL NEGATIVE-IONS .2. LASER PHOTOELECTRON SPECTROMETRY. *Physical Review A* **1974,** *10* (5), 1658-1664.

(48) Siegel, M. W.; Bennett, R. A.; Celotta, R. J.; Hall, J. L.; Levine, J., MOLECULAR PHOTODETACHMENT SPECTROMETRY .1. ELECTRON AFFINITY OF NITRIC-OXIDE AND MOLECULAR CONSTANTS OF NO. *Physical Review A* **1972,** *6* (2), 607-&.

(49) Posey, L. A.; Deluca, M. J.; Johnson, M. A. Chem. Phys. Lett. 1986, 131, 170.

(50) Metz, R. B.; Weaver, A.; Bradforth, S. E.; Kitsopoulos, T. N.; Neumark, D. M. J. Phys. Chem. 1990, 94, 1377.

(51) Neumark, D. M., Slow Electron Velocity-Map Imaging of Negative Ions: Applications to Spectroscopy and Dynamics. *Journal of Physical Chemistry A* **2008,** *112*, 13287-13301.

(52) Osterwalder, A.; Nee, M. J.; Zhou, J.; Neumark, D. M., High resolution photodetachment spectroscopy of negative ions via slow photoelectron imaging. *Journal of Chemical Physics* **2004,** *121* (13), 6317-6322.

(53) Eppink, A. T. J. B.; Parker, D. H. ReV. Sci. Instrum. 1997, 68, 3477.

(54) Leon, I.; Yang, Z.; Liu, H. T.; Wang, L. S., The design and construction of a high-resolution velocity-map imaging apparatus for photoelectron spectroscopy studies of size-selected clusters. *Review of Scientific Instruments* **2014,** *85* (8).

(55) Weichman, M. L.; Neumark, D. M., Slow Photoelectron Velocity-Map Imaging of Cryogenically Cooled Anions. In *Annual Review of Physical Chemistry, Vol 69*, Johnson, M. A.; Martinez, T. J., Eds. 2018; Vol. 69, pp 101-124.

Chapter 2

Experimental Methods

2.1 Experimental Overview

The construction of the anion photoelectron velocity map imaging instrument has been described elsewhere. [1,2] In this section, the current instrumental setup will be detailed, as it pertains to studying small beryllium-containing anions. Figure 2.1 shows the current configuration of the instrument, and can be divided into three regions, or chambers.

In the first chamber, molecules are produced using laser ablation of a metallic rod, backed by a pulsed buffer gas entrained with an oxidant source. The molecules are supersonically expanded into a time-of-flight mass spectrometer. The anions are accelerated, perpendicular to their initial trajectory, down the time of flight axis to allow for separation due to their differing mass-to-charge ratio (m/z).

In the second chamber, perpendicular sets of deflectors allow for the control of direction and angle of the travelling molecular beam. An Einzel lens is used for beam focusing, and a final pulsed deflector is used to act as a mass gate.

In the final chamber, anions are photodetached within the VMI interaction region and voltages on the VMI electrodes allow for the spatial separation of electrons of differing eKEs.

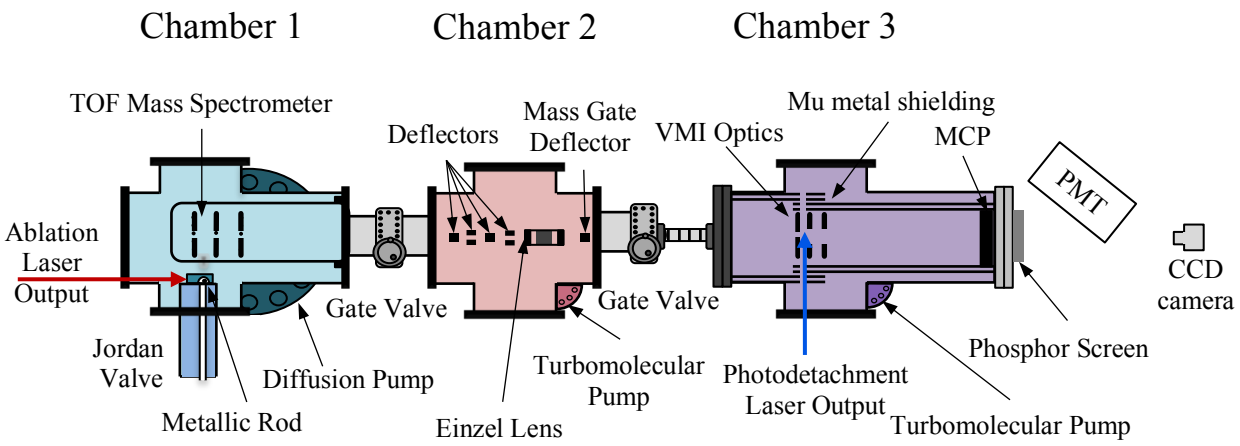

Figure 2.1. Bird's eye view of current configuration of the VMI apparatus.

The photoelectron Newton spheres are projected onto the detector and recorded by a CCD camera. Electronic events are accumulated into a complete image. The accumulated 2D image can be analyzed to reconstruct to original 3D velocity distribution to create a final spectrum.

The repetition rate of instrument is 10 Hz. Typical trigger settings and voltage settings all experimental components can be found in Tables 2.1 and 2.2.

Table 2.1. Typical triggered timings of experimental components.

Delay Generator	**Channel**	**Component**	**Timing Delay**	**Trigger Width**
Quantum Composers (QM)	C1	Minilite Q-switch	T_0 + 750-850 μs	10 μs
	C2	Minilite flashlamp	C1 – 150-200 μs	10 μs
	C3	**T_0**	**--**	**--**
	C4	MCP [a]	T_0 + 0-1000 μs	15 ns-1000 μs [b]
	C5	FL3000 excimer laser*	T_0 + 850-950 μs	10 μs
	C6	Continuum Nd:YAG Q-switch [a]	T_0 + 850-950 μs	10 μs
	C7	Continuum Nd:YAG Flashlamp	C6 – 250-390μs	10 μs
	C8	CCD camera	T_0 + 570 μs	Rising edge
SRS #1 (trigger synced to C3 on QM)	1A 1B	Jordan pulse valve	T_0 + 400-550 μs	Rising edge
	1C 1D	Mass gate deflector [a]	1C = 2C + 5-10 μs	1D = 1C + 200 ns-1μs
SRS #2 (trigger synced to C3 on QM)	2A 2B	WM-TOFMS repeller	2A = 2C – 5-20 μs	2B = 2A + 250 μs
	2C 2D	WM-TOFMS extractor	2C = T_0 + 850-930 μs	2D = 2C + 250 μs

[a] Photodetachment laser, mass gate deflector, and image acquisition timings are all dependent on the ion of interest and scale with the ion's specific time of flight.

[b] Long trigger widths (1000 μs) are used to monitor overall molecular signal. Very short trigger widths (15 ns) are used to discriminate photoelectron signal from general ion signal.

Table 2.2 Typical voltage settings for various experimental components.

Chamber Location	Component	Voltage
1	WM-TOFMS repeller	-2.10 kV– -2.30 kV
	WM-TOFMS extractor	-1.90 kV– -2.05 kV
2	V_1 deflector	0 – -20 V
	V_2 deflector	0 – -4V
	H_1 deflector	Not in use
	H_2 deflector	Not in use
	Einzel lens	-755 V
	Mass gate deflector	-10 – -50 V
3	VMI repeller	-350 V
	VMI extractor	-253.6 V
	MCP low voltage	800 V – 900 V
	MCP high voltage	1.65 kV – 1.90 kV
	Phosphor screen	4.85 kV
	PMT	-500 V

2.2 Laser Ablation

Laser ablation is a widely used method for the generation of molecular clusters in the gas phase, including ionic metallic species.[3] Compared to other techniques, such as discharge and thermal methods, generation of clusters through laser ablation requires less extreme working conditions, which could lead to difficulties in cooling of the molecules. Also, laser ablation is well suited to pulsed experimentation, as it is inherently a pulsed process. Laser ablation techniques have been employed in many anion photoelectron spectroscopy experiments, with favorable results. For these reasons, this technique was determined to be a sufficient method of producing our anions of interest.

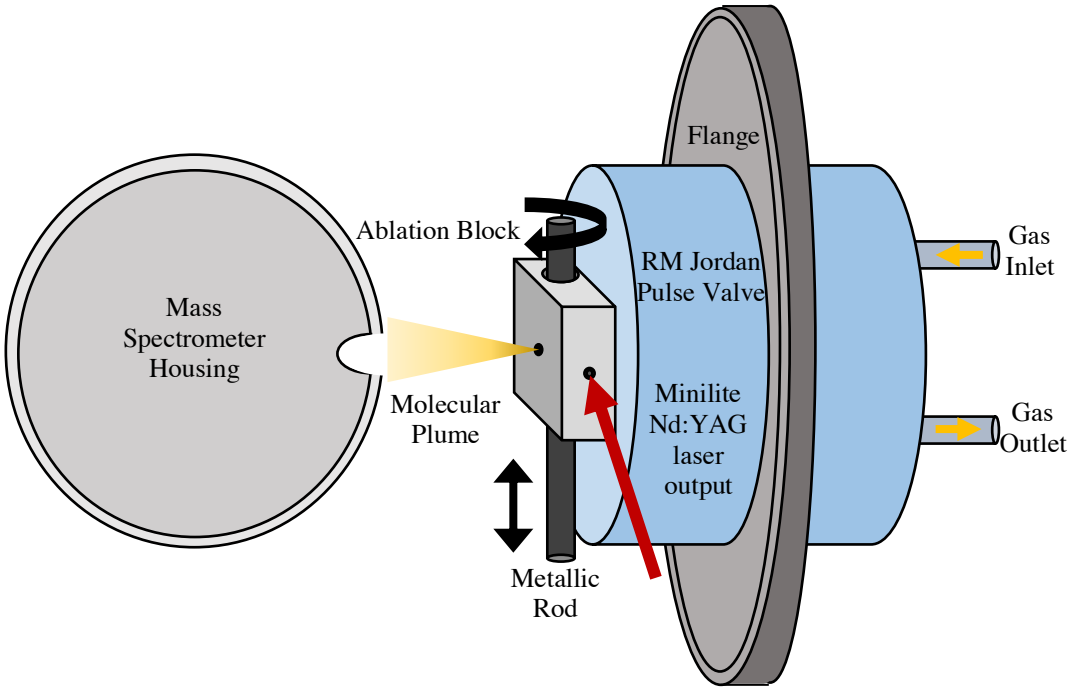

Figure 2.2 Diagram of the laser ablation setup, located in chamber 1.

A diagram for the laser ablation setup used in this experiment can be found in Figure 2.2. An ablation block, is mounted to the face of a RM Jordan pulsed supersonic valve (PSV-C211). This pulse valve produces pulse widths of 40-60 μs, a relatively short pulse duration which allows for the balance between necessary collisional cooling of the molecules, and avoidance of accidental detachment of our anions. Adjustments to the pulse duration can be made by tuning the current supplied to the top spring and return conductor of the pulse valve. Additionally, the timing of the pulse is controlled through a connected delay generator.

The gas channel of the pulse valve is aligned to the main reaction channel axis of the ablation block. Aligned perpendicular to the main channel, in the vertical direction, lies a much larger opening, containing our metallic rod. Rods are very common metallic targets used for laser ablation, as they are readily machined, and provide a smooth surface to ensure consistent signal production. In order to preserve rod uniformity over time, the rod is continuously translated and

rotated using a dual stepper motor arrangement. Consistent movement of the rod has the added benefit of preventing clogging of the block in short intervals of time, which would be detrimental to our data acquisition.

A final channel, aligned perpendicular to both the main channel and the rod channel, is used to guide the laser output to the molecular target. The laser used for ablation of material is a Minilite Nd:YAG laser. We have found the use of either the fundamental (1064 nm) or the second harmonic frequency (532 nm) to be sufficient for producing our molecules of interest. We have not observed a significant difference in signal generation between the two wavelengths. However, laser power has been found to have a much more obvious effect on our molecular densities. As such, we have found powers ranging from 8-30 mJ to produce sufficient densities, depending on the anion of interest.

A focused laser pulse vaporizes the surface of the metal rod, creating a vapor of neutrals, charged particles, and electrons in the main channel. Helium buffer gas, containing a molecular target we wish to interact with the ablated metal, is pulsed down the main channel, over the ablated material. The buffer gas entrains the ablated vapor, and as it flows down the main channel, metallic clusters form, the molecules are collisionally cooled and electron attachment occurs. As the molecules exit the ablation block, they are further cooled by supersonic jet expansion.

The cooling of anions is necessary, as it reduces spectral congestion, by narrowing rotational contours, and eliminating hot band structure. This reduction becomes exceedingly important as the size of your molecular cluster increases. The use of cryogenic ion traps have been demonstrated in the literature to aid in the study of many complicated species. For example, the Neumark group has combined cryogenic cooling with SEVI to obtain energy resolution down

to 2-3 cm^{-1} FWHM for molecular systems.[4] As the ongoing motivation for this project is to develop efficient methods to study larger beryllium clusters, plans have been made to implement a Paul ion trap into the existing experiment. Details on the design of the cold trap can be found in the dissertation of Amanda Dermer (MS).[2]

2.3 Mass Separation

Orthogonal to the jet expansion lies the housing of our Wiley McLaren Time of Flight Mass Spectrometer (WM-TOFMS). [5] The housing of our mass spectrometer consists of a steel tube, encapsulating the mass spectrometer and the drift region, with a small hole on axis to the jet expansion, to allow for molecules to enter the acceleration region of the mass spectrometer. Encapsulation is necessary to prevent electrical discharging of the mass spectrometer plates, caused by high pressures.

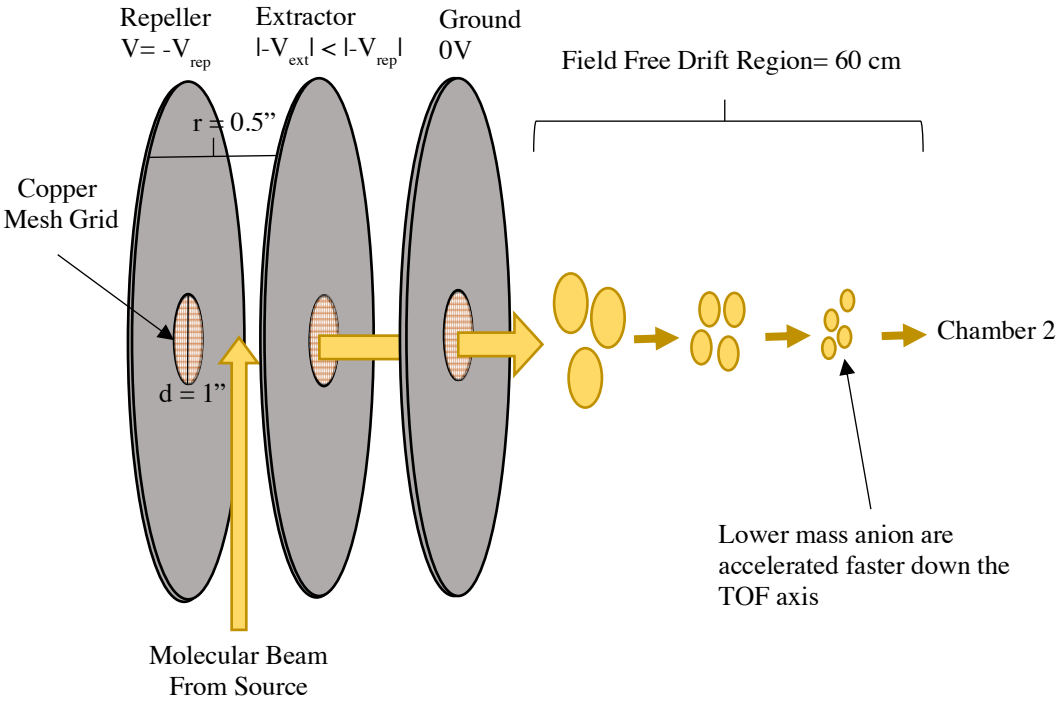

Figure 2.3. Schematic of the instrument's WM-TOFMS.

The WM-TOFMS, proposed by Wiley and McLaren in 1955, provided a method of collecting a full mass spectrum in minimal time, with significant improvement in the resolved mass range over previous mass spectrometers.[5] The WM-TOFMS employs a dual field source to temporally separate ions of different masses. The use of dual electric fields has been shown to allow for mass resolution for masses above 300 amu. Additionally, the added spatial focusing of the ion packets by the WM-TOFMS, improves the overall focusing of the electrons onto the detector after photodetachment. (See Section 2.5).

A diagram of our WM-TOFMS can be found in Figure 2.3. The WM-TOFMS consists of 3, equally spaced, circular metal electrodes: a repeller, extractor, and a ground. The voltages of the repeller and extractor electrodes are typically set to -2.16kV and -2.0 kV, to provide 1 amu resolution for masses up to 100 amu. Adjustments can be made to the relative voltage difference between repeller and extractor to resolve a range of greater mass peaks (see Section 7.4). Each electrode contains a 1 in diameter center hole, covered with a 95% transmittance copper mesh. The copper mesh acts to form a consistent electric field through the electrodes, to prevent spread of the molecular packet off of the TOF axis. The final ground plate prevents electric field bleeding into the field free drift region of the instrument. The molecular plume enters the mass spectrometer between the repeller (back) and extractor (middle) electrodes. The pulsed voltage on our repeller and extractor electrodes accelerate our anions down the axis of our instrument, where they spatially separate along the TOF axis, based on their masses. Focusing of the molecular packet through our spectrometer has been improved by introducing a slight time delay (~ 10 ns) between the voltage pulse on our repeller and extractor plates.

As the anions travel through the electric field, the change in voltage (ΔV) between the repeller (~2.2 kV) and the extractor (~2.0 kV) causes the ion of charge, q, to acquire kinetic

energy, E, such that, $E = \Delta V q$. Given the relation between a particle's kinetic energy and its velocity ($E_k = ½\, mv^2$), we can derive a relationship between the change in voltage and the velocity of a particle (v), given the particle's mass, m, in our experiment by Equation 2.1.

$$v = \sqrt{\frac{2\Delta V q}{m}} \qquad \text{Equation 2.1}$$

With this equation, it is possible to see that the time (t) required for an ion to travel down a field free drift region, d, is directly proportional to the square root of the mass of the ion, $\sqrt{m}$, given that $v = d/t$. This relation allows us to infer the masses of peaks knowing the mass and timing of one peak. If the identity of more than one peak is known in the spectrum, it is possible to generate a second order polynomial calibration curve, as shown in Figure 2.4. A comparison of these two calibration techniques can be found in Table 2.3. Both calibration methods are sufficient at predicting lighter masses, specifically, masses close to our calibration species, sulfur anion (S^-). However, the predicted masses of the increasingly slower peaks (ie. heavier molecules) begin to deviate from their true value, using Method 1. Using the timing (t_1) and the mass (m_1) for S^- in calibration method 1, the predicted mass for species of only 60-70 amu are shifted by 1 amu. A full calibration curve (Method 2), including high mass data points, accurately predicts heavier masses above 70 amu, within a single amu accuracy. Given our need for species selectivity, it is imperative to know the mass of our peaks down to a single amu, to allow for correct characterization or our molecules.

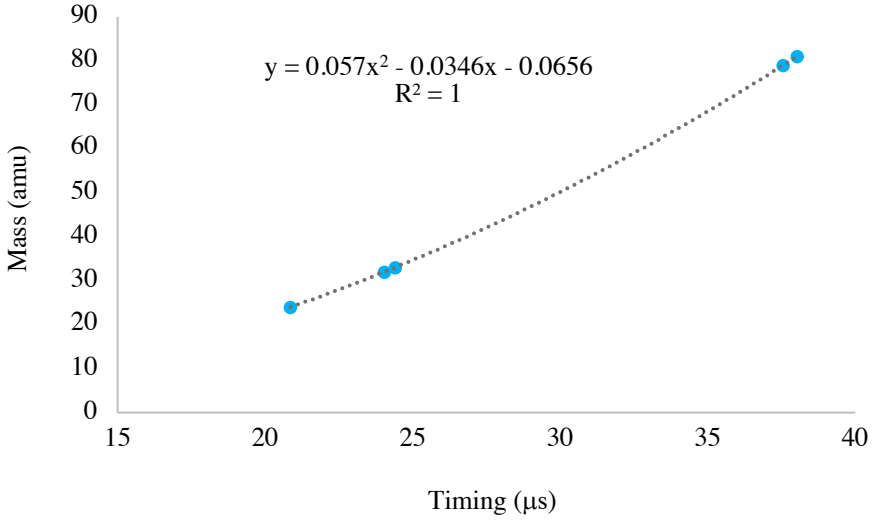

Figure 2.4 Sample mass spectrometer calibration curve, obtained using peak timings of known masses. The 2nd order polynomial function can be used to fit unknown peaks (see Column 3 of Table 2.3). The WM-TOFMS voltage settings for this sample calibration are V_R = -2.16 kV and V_E = -2.01 kV.

Table 2.3. Mass predictions by two methods: Method 1 (Column 2): Ratio of mass timings using the mass and time of flight of S^-. Method 2 (Column 3): polynomial fitting of mass to timing ratios, using a wide range masses of known species.

Timing (µs)	Mass predicted by $\frac{t_1}{t_2} \propto \frac{\sqrt{m_1}}{\sqrt{m_2}}$ (amu) [a]	Mass predicted by Calibration Curve (amu)	Actual Mass (amu)	Species [b]
24.04	**32**	**32.04**	**32.00**	**S**
20.86	24.09	24.02	24.00	C_2
21.30	25.12	25.06	25.00	BeO
21.70	26.07	26.02	26.00	BeOH
24.40	32.97	33.03	33.00	BeC_2
27.17	40.88	41.07	41.00	BeS
31.70	55.64	56.12	56.00	C_2S
36.20	72.56	73.37	73.00	BeS_2
37.56	78.11	79.05	79.00	^{79}Br
38.03	80.08	81.06	81.00	^{81}Br

[a] t_1 and m_1 are defined by S^-

[b] Assumes charge, z = -1

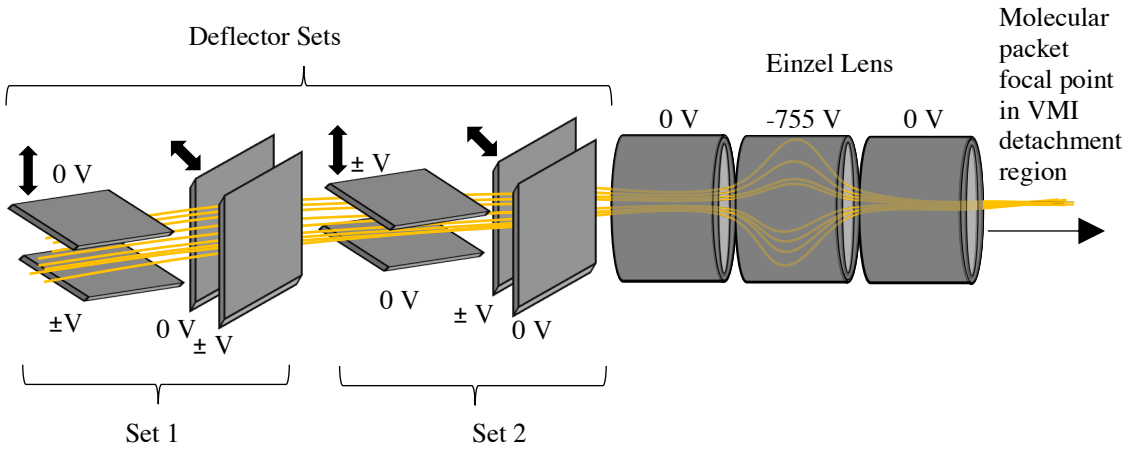

Figure 2.5. Arrangement of the ion optics present in chamber 2.

2.4 Molecular Packet Guiding

As has been previously mentioned, the focusing of the molecular packet into the VMI region is crucial for the resolution of our final electron image. In addition to the spatial focusing of the WM-TOFMS, 2 sets of deflector plates and an Einzel lens are present in the second chamber to aid in guiding the trajectory of the molecular packet, and improve focusing into the VMI region for detachment. A diagram of these ion optics can be found in Figure 2.5. As the molecular beam moves through the second chamber, it passes through two sets of perpendicular deflectors, which allow for vertical and horizontal adjustment of the molecular packet. By incorporating two sets of deflectors, we are able to control both the angle and position of the molecular packet as it continues to travel down the TOF axis. An Einzel lens is used to focus our molecular packet into the photodetachment region, located in the third chamber. Unlike the mass spectrometer, there is no advantage to pulsing voltages on these ion optics. Therefore, a continuous voltage is supplied to all electrodes just mentioned.

Conversely, A final pulsed deflector (not shown in Figure 2.5) is added to act as a mass gate for admission of molecules into the final chamber. The deflector plate is held at high voltage with respect to the charge of our ions (-40 to -120 V) to deflect all incoming molecules. Using a PSV 4150 pulse generator, couple to a high voltage supply, the voltage is rapidly turned off to allow for the transmission of our molecule of interest to pass into the photodetachment region, then the voltage is switched back on, to prevent any other molecules from entering the region. Given that two molecular masses, different by 1 amu, are separated in time by only 0.5 μs, with a time spread of ~0.01 μs, the fast rising and falling times (<25 ns) of the fast switching pulse generator were determined necessary to appropriately isolate a single mass.

2.5 Photodetachment and Velocity Map Imaging

Mass selected anions enter the VMI interaction region. They are photodetached by the vertically polarized output of either an excimer pumped dye laser, or a Continuum Nd:YAG with, or without, dye laser addition, ranging from UV to near IR light. The lowest resolution of all laser systems implemented is 0.4 cm^{-1}, well within the resolution of our VMI, and, therefore, not limiting. The laser power required for satisfactory photodetachment is 0.5-10 mJ. High laser powers can produce more photodetachment processes, but if the laser power becomes too great, it can cause electron detachment from metal surfaces inside the chamber, referred to here as "scatter." This scatter cannot be discriminated from the electrons originating from our molecule of interest, so it will lead to greater noise in our images. Also, large amounts of scatter generated can cause damage to our detector, when the MCPs are highly biased. Therefore, use of high laser power should be cautiously approached.

A detailed description of the implementation and configuration of our VMI spectrometer can be found in the theses of Dr. Kyle Mascaritolo and Amanda Dermer. [1,2] This section will

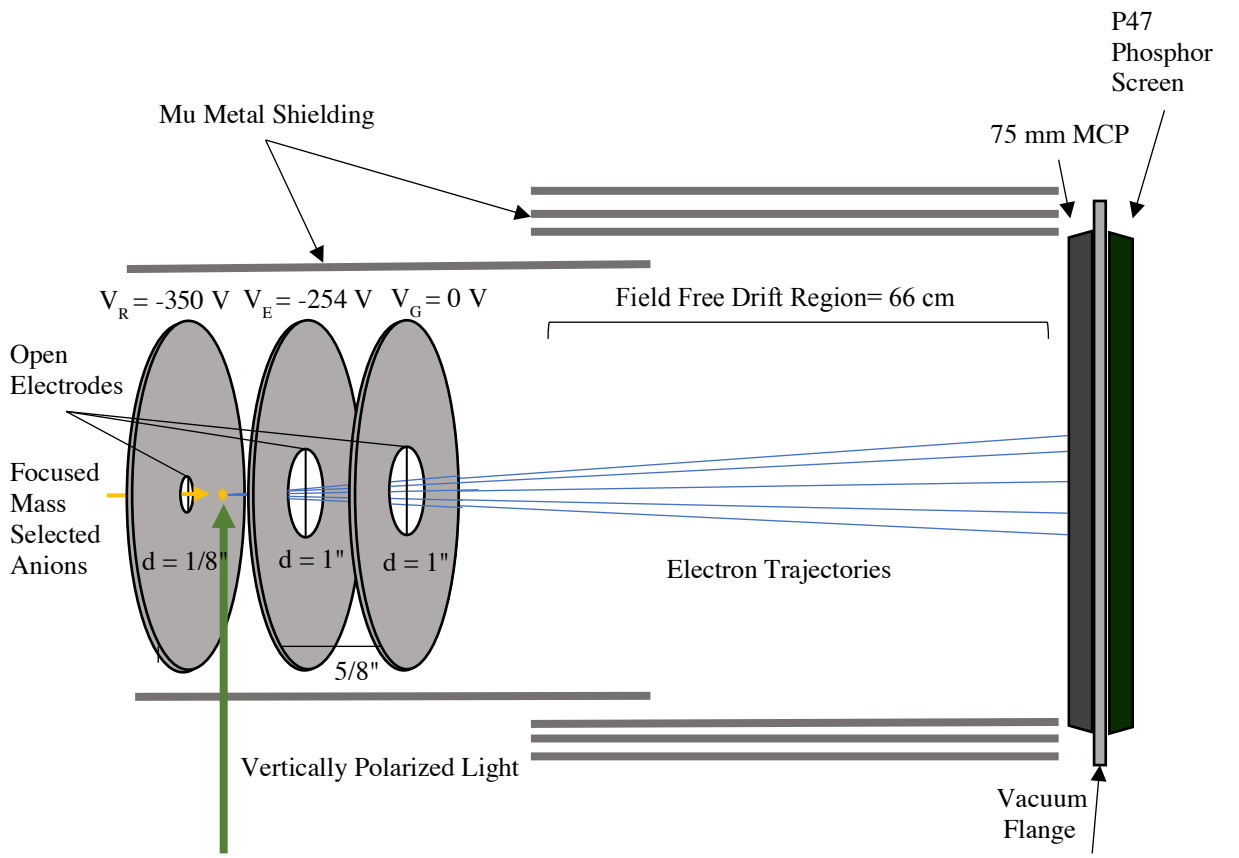

Figure 2.6. Design of the 3-electrode VMI arrangement in chamber 3. Schematic includes VMI setup, as well as, detector information.

detail the specifics of our instrument configuration as was used for the experiments described in this thesis. Currently, our VMI spectrometer is modeled after the original Eppink and Parker design,[6] and can be seen in Figure 2.6. The VMI consists of three stainless steel circular electrodes, (from back to front) the repeller, extractor and ground, to form 2 acceleration regions. A small aperture in the center of each electrode allows for transmission of ions and electrons through the optical setup. The center hole on the repeller is much smaller (1/8 in) than the center hole for the extractor and ground electrodes (1 in), as the second and third electrodes allow for the spread of electrons off the TOF axis. At first glance, the electrode setup may resemble that of our WM-TOFMS. However, one important difference is the lack of copper mesh covering the

center apertures of our VMI electrodes. The copper mesh in the TOFMS induces straight electric field lines, used to constrain molecules to the TOF axis. Conversely, the bent equipotential surface present in the VMI, due to the open apertures, allows for the spatial separation of electrons of different kinetic energies, orthogonal to the TOF axis. Another difference worth mentioning is the voltage supplied to the VMI electrodes is continuous, unlike the TOFMS, which is pulsed.

Each electrode in the assembly is electrically isolated from one another. The voltage of the repeller (V_R) is set to -350 V, and the extractor voltage (V_E) is a fraction of the V_R, normally close to ¾ the voltage ($V_E = 0.75*V_R$). The repeller voltage controls the magnification of our image projected on our detector, and the extractor voltage controls the focus of the projection. When determining the V_R voltage to be used, it is important to consider its susceptibility to stray electric and magnetic fields, as well as, it's magnification factor. Using higher voltages for the repeller can constrain the deflection of the electrons from the TOF axis, effectively allowing for electrons of a larger range of kinetic energies to be imaged at once. However, if the angle of deflection is restricted too much, separate eKE's will be mapped to nearly the same pixel distance on the detector. Upon image processing, overlapping eKE's will not be able to be differentiated, leading to a loss in resolution. On the other hand, using very low acceleration voltages will allow for distinct separation of eKE's, that are very close together, but lower voltage accelerations are more susceptible to stray electric and magnetic fields, which can cause image distortions. As such, a V_R of -350 V has been found to strike a good balance between magnification and field immunity for our system.

At V_R = -350 V, the photoelectrons are accelerated down a 66 cm field free drift region. As the electrons travel down the drift region, they are protected from stray fields by four layers

of mu-metal shielding. Electrons of the same kinetic energy are mapped to the same pixel distance from the center of our detector. The resolution of our spectrometer is on par with the original 3-plate design: $\frac{\Delta eKE}{eKE} = 3\%$. The maximum eKE recorded with the given V_R is 4000 cm^{-1}, with ΔeKE = 120 cm^{-1}. The absolute resolution of our spectrometer is limited due to damage sustained by the MCP detector. Due to a dark spot present in the center of the detector, the lowest eKE we can record is 146 cm^{-1}. Therefore, the absolute resolution of our instrument is 4 cm^{-1}.

2.6 Detecting & Recording Electron Distributions

Photodetached electrons are projected onto a PHOTONIS USA, INC. 75mm Chevron stacked microchannel plates (MCP) with a fiberoptic P47 phosphor screen detector. Electrons can be easily discriminated from molecular signal by reducing the gate of the MCP, to only allow for the record of photoelectron events incident on the detector. The use of the mass gate, described in Section 2.4, was found beneficial in eliminating signal for anions with timings coincident to our electron signal, which could not be removed with simply minimizing the MCP pulse.

The incident electrons are recorded by an off-axis photomultiplier tube (PMT) and an IDS UI-2230SE-M-GL Rev. 3 CCD camera (1024 X 768) with 1 inch focal length lens. Both recording instruments are mounted to a 60 cm black aluminum tube, which is fixed to the detector flange. The aluminum tube prevents the camera and PMT from recording ambient light, as well as, provides a way to easily orient the camera, with respect to the detector. To further reduce ambient light from accidently being recorded by the camera and PMT, the tube is wrapped in dark wool.

The PMT is positioned 10 cm downstream and off axis from the detector screen. It is used to record signal production in real time. Connected to an oscilloscope, the PMT allows us to make adjustments to the settings for our laser ablation, mass spectrometer, and ion optics, to optimize production of our anion of interest. It provides us with the flight time of our molecules through the instrument.

The camera provides the spatial information required for velocity map imaging spectroscopy. The camera is oriented on axis to the face of the phosphor screen. When an event occurs on the detector, it is recorded by the camera, retaining the position information of the event. The camera is considerably inexpensive (>$1000) and readily integrates into the event counting program, NuACQ, developed by Arthur Suits. The NuACQ program allows for the direct control of the camera through the program. The camera is set to externally trigger, by the rising edge of a trigger off of T_0 on the QC delay generator (see Table 2.1). A pixel clock setting of 11 MHz is required to prevent image aberrations from improper binning of the camera signal, cause by higher pixel clock settings. An exposure time of 654 μs is used to captured all events incident on the detector.

Every experiment cycle, an electron distribution is recorded and stored by the NuACQ program.[7] Electron signal is accumulated over many cycles (20,000-500,000 cycles) to form a complete velocity map image. The NuACQ program allows for raw or centroid image accumulation. Raw accumulation is a straightforward event counting, whereas centroiding applies a center of mass calculation to events that cover multiple pixels, lowering the signal point size to subpixel limits. Reduction of electron spot size improves our image resolution, at a cost to the acquisition time. Due to the lengthy acquisition times already employed to accumulate raw images for our instrument, centroiding has not been implemented at this time.

2.7 Image Reconstruction

When electrons are photodetached from our anions with vertically polarized light, they form Newton spheres with cylindrical symmetry about the axis of polarization (in this section, this axis is referred to as the z axis). The projection of these spheres onto the planar detector creates a ion image, $D(z,x)$, which is a map of the position of all incident electrons. Due to the cylindrical symmetry about the z axis, it is possible to extract all necessary information about the 3D projection by simply rotating about the z axis. In order to find the relation between pixel location and eKE of a given distribution of electrons, it is necessary to construct a velocity map, $F(z,r)$, where r is the coordinate perpendicular to our z-coordinate, defined as $r = \sqrt{x^2 + y^2}$. Knowing the velocity map allows for the generation of an expected ion image, $A(z,x)$, through an Abel transformation:

$$A(z,x) = 2\int_x^\infty F(z,r)\frac{r\,dr}{\sqrt{r^2 - x^2}}$$ Equation 2.2

However, the velocity map distribution, $F(z,r)$, is not known, and must be determined from the image. By assuming $A(z,x) = D(z,x)$, it is possible to perform a inverse Abel transformation on the recorded ion image to determine the velocity distribution map:

$$F(z,r) = \frac{-1}{\pi}\int_r^\infty \frac{\partial A}{\partial x}\frac{dx}{\sqrt{x^2 - r^2}}$$ Equation 2.3

Applications of this method are known to suffer some complications. In reality, as A(z,x) is not exactly equivalent to $D(z,x)$, many times transformation of the data set will require some pre-transformation fitting or smoothing. This method is known to break down, leading to a center line artifact, where noise becomes very high for $F(z,r)$ where r approaches zero. Also, inverse Abel transformation does not work well on data sets with very little signal.

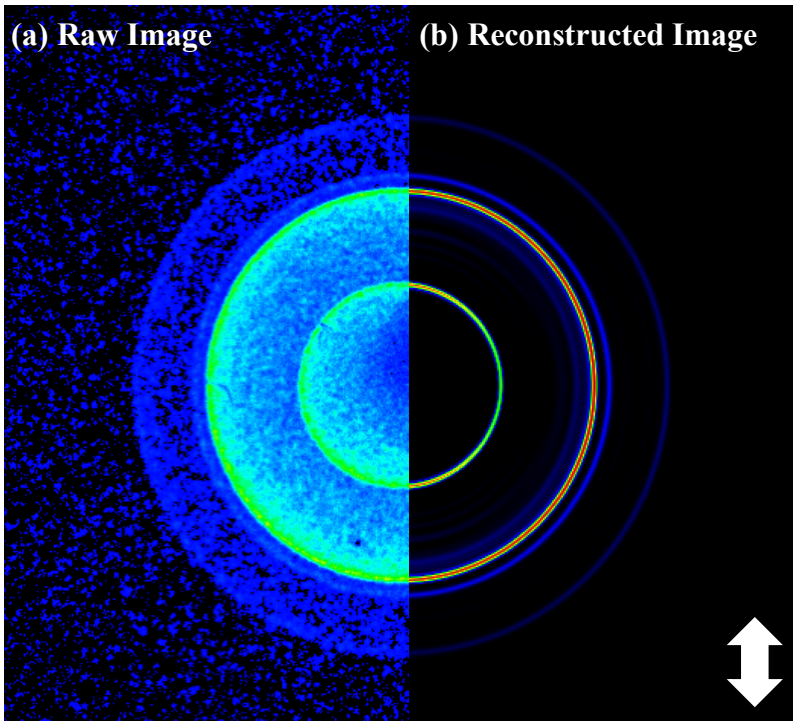

Figure 2.7. A comparison of an atomic sulfur raw image, after electron signal accumulation (a), and after the raw image has been processed using MEVELER and reconstructed using Mathematica (b). The double headed arrow indicated the polarization of photodetachment light.

Instead, we employ a method that bypasses the need for an inverse Abel transformation and pre-treatment smoothing, known as Maximum Entropy Velocity Legendre Reconstruction (MEVELER).[8] In MEVELER, the $F(z,r)$ velocity map is iteratively changed in order to increase the probability that a generated ion image, $A(z,x)$ will model the data set, $D(z,x)$. The likelihood

of matching $A(z,x)$ and $D(z,x)$ is based in Bayesian statistics, with an additional consideration for Poissonian statistics, which dictate pixel event counts. The angular dependence is determined through an expansion of the velocity distribution in Legendre polynomials, to provide a straightforward method of determining the anisotropy of our image.

Detailed explanations of the MEVELER algorithm can be found in other sources. [8] Briefly, the file generated from the NuACQ program (extension = .dat) can be converted into a text file representing the matrix describing $D(z, x)$. The MEVELER program first applies a centering algorithm to this matrix, and divides the matrix into four quadrants. The quadrants are assigned weights and contracted into a single quadrant for MEVELER analysis. It is important to note that weights can be manually assigned to the quadrants, in order to remove data from being analyzed, if there are concerns about part of the image's quality. Additionally, it was found helpful to also manually set the center, as opposed to using the centering algorithm, when using a file that only represented a half image.

After applying MEVELER to a data set, an image reconstruction program, created in the computing system, Mathematica,[9] can be used to construct a final image of the velocity distribution. A comparison of a raw image and a reconstructed image can be found in Figure 2.7.

2.8 VMI Calibration

Calibrations of the VMI focusing and VMI eKE to pixel ratio were carried out using the known transitions of atomic S^-. An energetic scheme of the $S^- \rightarrow S$ atomic transitions and sample calibration spectrum can be found in Figure 2.8. Sulfur has 6 anion to neutral atomic transitions in a very convenient wavelength range (577 nm- 614 nm). This wavelength range is easily accessed by the second harmonic of our Nd:YAG laser (532 nm) and by the highly efficient laser dye, Rhodamine 590 (Rhodamine 6G), ensuring photodetachment photon generation will not be a limiting factor. Also, generation of S^- anions in our instrument is more than sufficient through laser ablation of our metallic rod and helium buffer gas seeded with CS_2. Together, high laser fluency and significant atomic generation of S^-, allow for relatively expedient calibration.

For optimization of the VMI focusing, the VMI repeller voltage is held constant, and the VMI extractor voltage is tuned using a potentiometer in order to improve focusing of the same eKE electrons to the same radial distance on the detector. The ratio of V_E/V_R is expected to be approximately 0.75, so for a V_R = -350V, V_E should be close to -262.5 V. Multiple calibration images are taken at the same photodetachment wavelength (typically ~565 nm), and differing extractor voltages in the range of -262.5 ± 10 V. By eye, it is possible to evaluate the improvement of focusing by comparing the separation of peaks 3,4, and 5 in the sulfur calibration spectrum. Ideal focusing has been achieved when these peaks are sufficiently separated, and further adjustments to the extractor voltage do not lead to further separation of the three spectral features. Typically, an extractor voltage of -253.6 V is found to produce the best focusing for V_R = -350V .

Once optimization of the focusing of the VMI is complete, it is possible to move onto calibrating the pixel position of discrete eKE's for a set of VMI voltages. Multiple calibration images are taken at constant VMI voltages, but varied photodetachment energies in order to determine the radial pixel displacement for each transition evident in the image. Given the photodetachment energy ($h\nu$) and the atomic transition energies (eBEs) are known, we can calculate eKE = $h\nu$- eBE for each transition. By performing a least squares second order polynomial fit of the eKE to radial pixel distance from the center of the image, we obtain VMI calibration parameters.

(a)

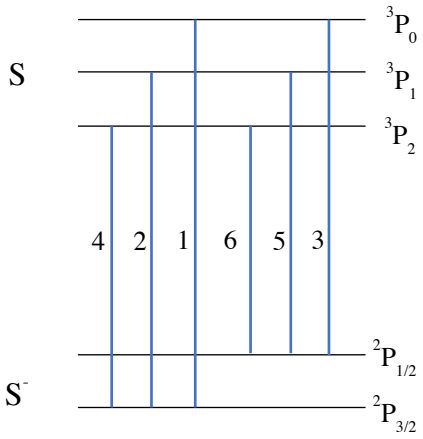

(b)

Transition Energies (cm^{-1})	
1	17327.376
2	17149.776
3	16842.276
4	16752.976
5	16665.5
6	16268.676

(c)

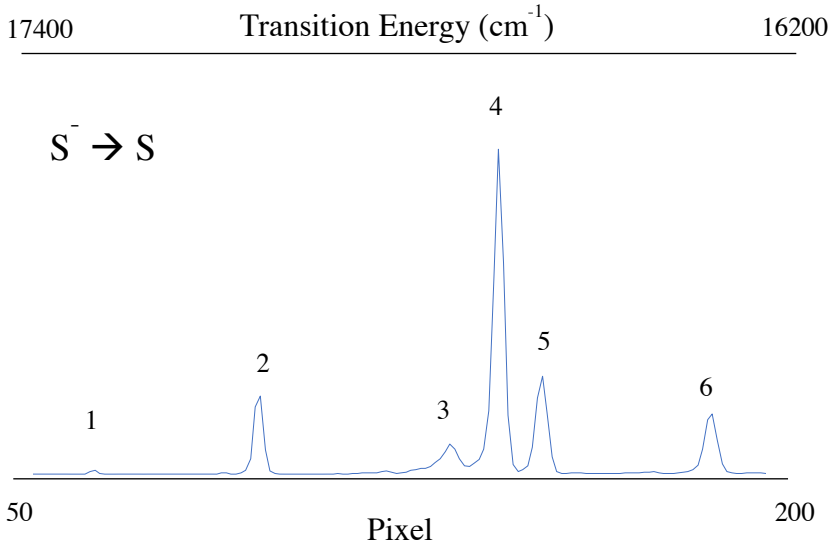

Figure 2.8 (a) Atomic S^- → S energy diagram. (b) Atomic S^- → S transition energies in wavenumbers. (c) Sample sulfur calibration spectrum, as a function of radial pixel position as well as transition energy (eBE = hν – eKE.)

2.9 Chapter 2 References

(1) Mascaritolo, K.J. PhD Thesis: A Journey towards the Construction and Operation of a Photoelectron Velocity-Map Imaging Spectrometer. **2016**

(2) Dermer, A.R. MS Thesis: Photoelectron Velocity Map Imaging Spectroscopy of Small Beryllium-Containing Anions. **2017**

(3) Duncan, M. A., Invited Review Article: Laser vaporization cluster sources. *Review of Scientific Instruments* **2012,** *83* (4).

(4) Weichman, M. L.; Neumark, D. M., Slow Photoelectron Velocity-Map Imaging of Cryogenically Cooled Anions. In *Annual Review of Physical Chemistry, Vol 69*, Johnson, M. A.; Martinez, T. J., Eds. 2018; Vol. 69, pp 101-124.

(5) Wiley, W. C.; McLaren, I. H., TIME-OF-FLIGHT MASS SPECTROMETER WITH IMPROVED RESOLUTION. *Review of Scientific Instruments* **1955,** *26* (12), 1150-1157.

(6) Eppink, A.; Parker, D. H., Velocity map imaging of ions and electrons using electrostatic lenses: Application in photoelectron and photofragment ion imaging of molecular oxygen. *Review of Scientific Instruments* **1997,** *68* (9), 3477-3484.

(7) W. Li, S. D. Chambreau, S. A. Lahankar, and A. G. Suits, *Rev. Sci. Instrum.* **2005**, *76*, 063106.

(8) Dick, B. Inverting ion images without Abel inversion: maximum entropy reconstruction of velocity maps. *Phys. Chem. Chem. Phys.* **2014**, *16*, 570–580.

(9) Wolfram Research, Inc., Mathematica, Version 12.0, Champaign, IL **2019**

Chapter 3

Photodetachment Spectroscopy of the Beryllium Oxide Anion, BeO^-

The contents and figures of this chapter are reprinted or adapted with permission from

Mascaritolo, K. J., Dermer, A. R., Green, M. L., Gardner, A. M., & Heaven, M. C. Photodetachment spectroscopy of the beryllium oxide anion, BeO^-. *The Journal of Chemical Physics*, **2017**, *146*(5), 054301.

The $X^2\Sigma^+ \rightarrow X^1\Sigma^+$ anion to neutral ground state photodetachment of BeO has been studied by means of photoelectron velocity map imaging spectroscopy in a newly constructed velocity map imaging spectroscopy apparatus. Vibrational intervals, rotational constants, and the electron detachment threshold of BeO^- were determined for the first time. The small moment of inertia of beryllium oxide allowed for the observation of partially resolved rotational contours. Analyses of these contours provided evidence of several detachment channels resulting from changes in the molecular rotational angular momenta of $\Delta N = 0, \pm 1, \pm 2$, and ± 3. The relative intensities of these detachment channels were found to be a function of the electron kinetic energy. Experimental results are compared to the predictions of high level *ab initio* calculations.

3.1 Introduction

The chemistry of beryllium is known to be significantly different from the behavior exhibited by the heavier Group IIA elements.[1-13] In part, this is due to the high ionization energy (9.32 eV) and small radius of Be. As a consequence, the bonds formed by beryllium have appreciably more covalent bonding character. Theoretical techniques have often been used to explore Be chemistry, conveniently circumventing the toxicity issues (see, for example, Ref. 1 and the references therein). At first glance, Be seems to be well suited for investigation using non-relativistic quantum chemical methods. It is a light element with only four electrons. However, calculations for Be-compounds often prove to be difficult, with the Be_2 dimer being a celebrated example.[14-23] Problems arise because the bonds involving beryllium can be dominated by electron correlation, such that they include significant contributions from doubly excited electron configurations.

Diatomic beryllium oxide (BeO) is an ideal species for studies of Be bonding. It has been the subject of both spectroscopic and theoretical investigations.[24-38] Based on theoretical calculations, Frenking and co-workers[6,39-41] have noted that BeO is an extraordinarily strong Lewis acid, with the ability to attract He with a bond energy of 1500 cm^{-1}. This prediction has been supported by subsequent theoretical studies.[42,43] Similarly, electronic structure calculations indicate that the electron affinity of BeO is relatively large (2.1–2.2 eV).[44,45] The electron binding energy is high enough for the BeO^- anion to support both valence and dipole-bound electronically excited states. The latter are stabilized by the 6.26 D permanent dipole moment of BeO.[44] To date, there have been no published experimental studies of BeO^-.

In the present work, we have used anion photodetachment spectroscopy to determine the electron affinity of BeO and molecular constants for the ground state of BeO^-. This effort was motivated by interest in testing the previous theoretical predictions for BeO and to provide data for further testing and refinement of the quantum chemistry models used for anions. Looking beyond these immediate objectives, this will be the first step towards studies of larger Be_nO_m clusters by means of anion photodetachment techniques. Studies of such clusters can reveal the degree of covalency and some of the unique electrostatic binding capabilities of small beryllium oxide species. For example, theoretical calculations predict that $(BeO)_n$ clusters can be used as a lightweight, reversible storage medium for H_2.[8,13,46] Hence, in addition to the fundamental science questions, the work on the oxide clusters relates to potential practical applications of these materials.

3.2 Experimental Procedure and Spectrometer Description

The data presented here were recorded using photoelectron velocity map imaging spectroscopy. The details of the technique have been described extensively in other publications.[47-49] The imaging apparatus used in this study was modified from an existing setup described elsewhere.[50] Only the new additions to the current spectrometer are discussed in detail here.

A diagram of the apparatus used to study BeO^- can be found in Chapter 2, Figure 2.1. Anions were produced in a laser ablation source[51] using a beryllium rod target and the focused, frequency doubled output of a Nd:YAG laser (532 nm, ~8 mJ). This source was coupled to a pulse valve that delivered 70%/30% Ne/He carrier gas seeded with 2.5% N_2O at a backing pressure of 55 psia. The anions produced by the ablation process were supersonically expanded into a differentially pumped vacuum chamber, where a Wiley-McLaren time of flight mass spectrometer (WM-TOFMS),[52] in a perpendicular orientation with respect to the direction of the expansion, was housed. Fast rising, negative pulsed voltages were applied to the repeller and extractor of the WM-TOFMS by high voltage switches, accelerating the anions into a drift region to allow for mass separation before reaching the photodetachment region of the velocity map imaging optics. The resolution of the mass spectrometer was $m/\Delta m = 690$ at masses around 40 amu.

Along the flight path of the anions from the WM-TOFMS, an Einzel lens and four sets of deflector plates were used to focus and guide the anions into the velocity map imaging (VMI) optics. Additionally, a fifth set of deflector plates could be pulsed to act as a mass gate to only allow the anion of interest to enter the detachment region. One plate of each pair was grounded while the opposite plate was connected to a dual polarity voltage source.

Once inside the VMI optics, the mass selected anions were intercepted by the polarized, focused output of a Nd:YAG pumped dye laser or an excimer pumped dye laser operating at a photon energy above the detachment threshold of the species of interest. Typical detachment laser pulse energies were in the range of 0.5–1.0 mJ, with a beam diameter of < 2 mm. The dye laser linewidths were approximately 0.3 cm^{-1} (FWHM). Wavelength calibrations of the lasers were established using the gas phase absorption spectrum of the B–X transition of room temperature I_2. The absolute energies of the I_2 lines were taken from the PGOPHER software package.[53]

The velocity map imaging electrodes were replicated from the original Eppink and Parker design[49] using 1/16 in. thick 304 stainless steel. The photoelectrons produced within the VMI lens were accelerated down a 66 cm long drift region, shielded from external electric and magnetic fields by layers of mu-metal, to the detector (Photonis USA, Inc., 75 mm Chevron stacked microchannel plates (MCPs) with a fiberoptic P47 phosphor screen). Images from the detector screen were recorded by a CCD camera (Physimetrics UI- 2230SE-M-GL, 1024 X 768). The photodetached electrons were discriminated from all other charged particles by pulsing the voltage (gain) on the MCPs at the appropriate arrival time. Individual cycles of the experiment were recorded and summed over several hundred thousand laser pulses to produce an image. The final image was saved using the imaging collection software developed by Li *et al*, called NuACQ.[54] The transformation of the image from velocity space to energy was done using the Maximum Entropy Velocity Legendre Reconstruction (MEVELER) technique.[55] The total emission of the screen from electron or anion impacts could also be monitored with a photomultiplier tube positioned off axis from the camera. This mode of detection produced a TOF-MS spectrum and was extremely useful in the optimization of anion and photoelectron

production. The repetition rate of the experiment was 10 Hz. All images were calibrated using the known transitions from the detachment of sulfur anion, S^-. [56-58]

3.3 Electronic Structure Calculations

The ground state electronic configurations of BeO and BeO^- are easily anticipated. BeO is a closed shell ionic species with an experimentally verified $X^1\Sigma^+$ ground state. The unpaired electron of BeO^- resides in an orbital that is primarily of Be 2s character, giving rise to a $X\ ^2\Sigma^+$ ground state. Electronic structure calculations were performed on both the anion and neutral beryllium oxide molecules. This was done to assist in the assignment of the spectra and to evaluate the suitability of the chosen electronic structure methods for the treatment of this prototypical small molecular anion. For both beryllium and oxygen, the aug-cc-pwCVXZ (X = T, Q, 5) basis sets were employed, denoted by awCVXZ herein. A second set of diffuse functions was added to these basis sets in order to better describe the diffuse nature of the BeO frontier orbitals. The exponents of the diffuse functions were determined from an even-tempered expansion of the two lowest exponent functions of the awCVXZ basis sets. The resulting basis sets are denoted d-awCVXZ in the following.

All calculations were performed with the MOLPRO suite of programs.[59] Potential energy curves (PECs) were calculated, pointwise, by means of the partially spin adapted coupled cluster method including single and double excitations and perturbative corrections for triple excitations (RCCSD(T)), and the complete active space self-consistent field followed by multireference configuration interaction (CASSCF+MRCI+Q) levels of theory. The PECs are shown in Figure. 3.1. In the RCCSD(T) calculations, all electrons were included in the correlation treatment. The active space in the complete active space self-consistent field (CASSCF) calculations consisted

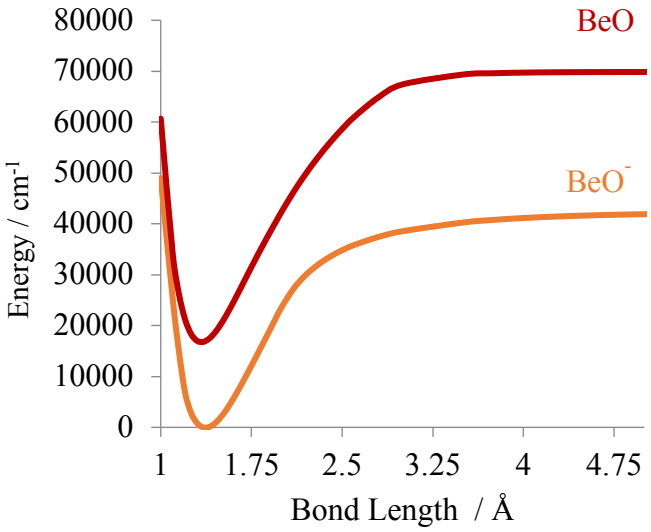

Figure 3.1. Potential energy curves (PECs) of neutral BeO and anionic BeO^-.

of the 2*s* and 2*p* orbitals of both Be and O, while the "core" orbitals, which are linear combinations of the 1*s* atoms orbitals, were constrained to be doubly occupied. Their wavefunctions were optimized in the CASSCF procedure to aid convergence. For both the anion and neutral BeO species, all electrons were included in the correlation treatment of the subsequent multireference configuration interaction with doubles (MRCID) calculation in an attempt to recover the core-valence correlation energy. The Davidson correction was applied in order to partially compensate for the size inconsistency of the MRCI calculations. Total RCCSD(T) and multireference configuration interaction with singles and doubles (MRCISD) interaction energies were extrapolated to estimate the complete basis set limit using the two point formula of Halkier *et al*.[60] (referred to as d-aV(Q,5)Z). The bound ro-vibrational levels of the resulting PECs were calculated using the LEVEL 8.0 program.[61] The lowest vibrational energy levels were least squares fit to the standard Morse energy level expression, yielding effective

values for ω_e and $\omega_e\chi_e$. Predictions for the electron affinity were made with the inclusion of the zero point vibrational energies.

Initially, restricted Hartree–Fock RCCSD(T) (RHF- RCCSD(T)) calculations were carried out for the expected $^2\Sigma^+$ ground state of BeO^-. Although the T_1 diagnostic, a commonly employed test of the degree of multi-reference character of the electronic wavefunction, had values of 0.022 at internuclear separations in the vicinity of the equilibrium bond length of the anion (1.3-1.5 Å), it increased to 0.04 at an internuclear separation of 1.8 Å. Additionally, the convergence of the RHF wavefunction became unstable at longer bond lengths. Values of the T_1 diagnostic lying above 0.04 suggest distinctly the multi-reference character. The T_1 diagnostic examines amplitudes of single excitation in the RCCSD procedure, based on a given self-consistent field (SCF) wavefunction. Large values of the T_1 diagnostic may be obtained when the reference wavefunction is a poor description of the electronic state of interest, and therefore large amplitude single electron excitations are apparent in the more representative RCCSD wavefunction (note that CCSD calculations using a spin unrestricted reference wavefunction are not supported by MOLPRO). As an alternative, initial wavefunctions obtained from a B3LYP (Becke, three-parameter, Lee-Yang- Parr exchange-correlation functional) calculation were used in subsequent RCCSD and RCCSD(T) calculations. These calculations displayed well-behaved convergence at internuclear separations of 1-50 Å, with values for the T_1 diagnostic below 0.04 being obtained at internuclear separation between 1.0 and 5 Å. This method is referred to as B3LYP- RCCSD(T) later in Section 3.4.

The results from calculations for both BeO and BeO^- are presented in Table 3.1. The predictions for BeO are in good agreement with previous theoretical predictions and reasonably close to experimental data. The equilibrium bond length was within the experimental error range,

Table 3.1. Experimental and theoretical spectroscopic parameters for BeO and BeO^-. All values are in units of wavenumbers (cm^{-1}), expect R_e which is given in Angstroms.

BeO			
	Exp [a]	B3LYP-CCSD(T)	MRCI
ω_e	1487.32	1493.5	1502.7
$\omega_e x_e$	11.83	11.2	11.6
R_e	1.331	1.330	1.329
BeO^-			
	Exp	B3LYP-CCSD(T)	MRCI
eBE	17535 ± 15	17487	17236
ω_e	1384 ± 10	1394.2	1397.6
$\omega_e x_e$	9.7 ± 2	9.7	10.9
$\Delta G_{1/2}$	1367 ± 7	1374.8	1375.8
$\Delta G_{3/2}$	1348 ± 5	1355.4	1354
$\Delta G_{5/2}$	1325 ± 10	1336.0	1332.2
$\Delta G_{7/2}$	1305 ± 5	1316.6	1310.4
$\Delta G_{9/2}$	1287 ± 5	1297.2	1288.6
$\Delta G_{11/2}$	1273 ± 5	1277.8	1266.8
$\Delta G_{13/2}$	1250 ± 5	1258.4	1245
$\Delta G_{15/2}$	1225 ± 5	1239	1223.2
R_e		1.364	
B_e		1.568	
α_e		0.017	
D_e		8.39×10^{-6}	
β_e		6.13×10^{-7}	

[a] Values reported from Ref [26].

while the harmonic vibrational frequency was slightly overestimated. Our calculations for BeO^- are also in agreement with earlier theoretical studies.[44,45] The additional electron, which primarily

resides in the Be 2*s* orbital, causes the bond to lengthen and the vibrational frequency to decrease by approximately 100 cm^{-1}. Lastly, the vertical electron detachment energy is predicted to be in the range of 17200–17500 cm^{-1} (2.13–2.17 eV).

3.4 Experimental Results and Discussion

Figure 3.2 shows photodetachment spectra for BeO^- , obtained by analyses of velocity map images. All of the stronger features in the images yielded near isotropic electron angular distributions, as can be seen in the reconstructed velocity map in Figure 3.3. The horizontal scale for these spectra, labeled as transition energy, is the photon energy minus the electron kinetic energy (eBE = hν – eKE). The traces correspond to images recorded using photon energies of 18110.48 cm^{-1}, 17733.93 cm^{-1}, 16744.75 cm^{-1}, and 16359.34 cm^{-1} , respectively. Note that the

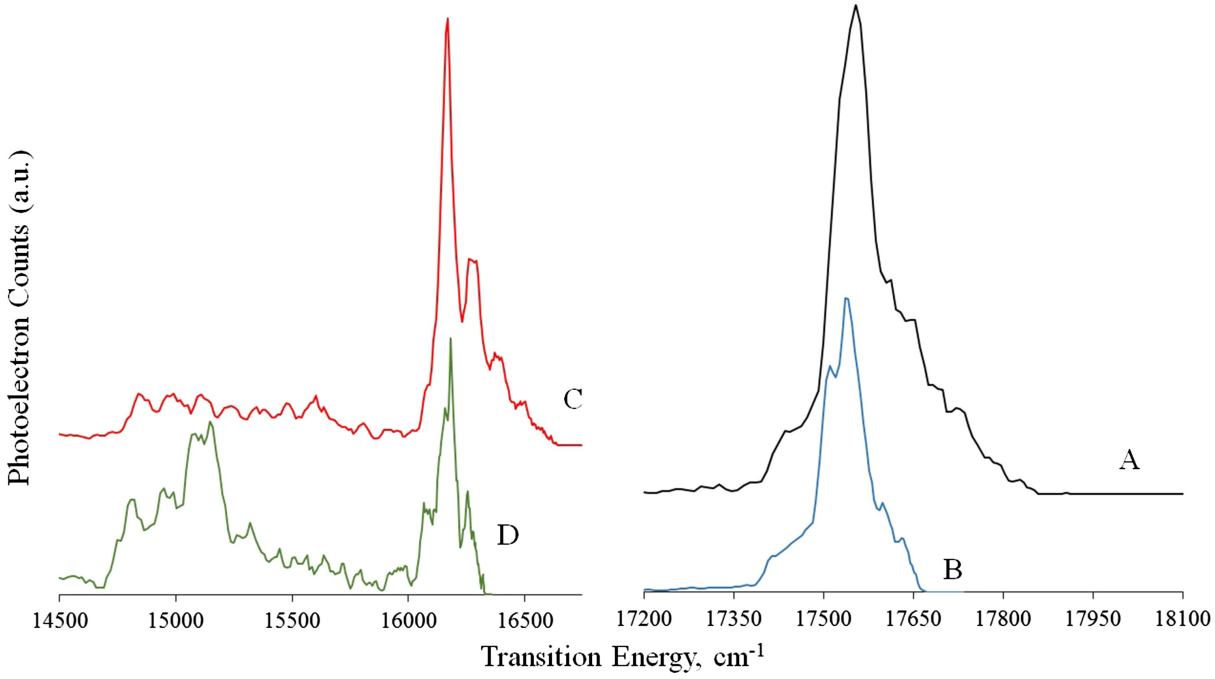

Figure 3.2. Photodetachment spectra of BeO^- at photon energies of (A, black) 18110.5 cm^{-1}, (B, blue) 17733.9 cm^{-1}, (C, red) 16744.8 cm^{-1}, and (D, green) 16359.3 cm^{-1}. The transition energy is defined as hv–eKE.

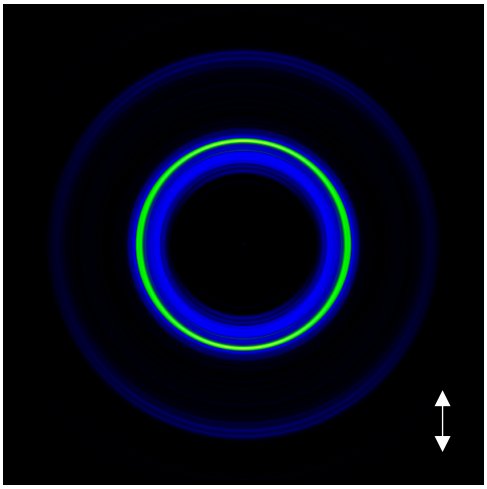

Figure 3.3. Velocity map image of BeO^- → BeO, taken at photon energy, 18110.5 cm^{-1}. The double headed arrow indicates vertical polarization of light

intensities of the four spectra were scaled for presentation purposes. Comparisons of intensities for spectra recorded using different detachment energies are not meaningful. However, the relative intensities of features within a single spectrum are valid.

Traces A and C, combined, show three groups of features. The analysis of trace A, which was recorded with the highest energy photons, is the most straightforward. Based on the molecular constants given in Table 3.1, the features in the 17400– 18000 cm^{-1} range are consistent with the $\Delta v = 0$; 0–0, 1–1, 2–2, 3–3 sequence bands. Similarly, the bands in the 16000-16700 cm^{-1} range (trace C) are the $\Delta v = -1$; 0–1, 1–2, 2–3, 3–4 transitions, while the bands in the 14600–15700 cm^{-1} range are the $\Delta v = -2$; 0–2, 1–3, …6–8 transitions. Clearly there was appreciable population of the excited vibrational states of the anion. Note that the $\Delta v = -2$ features of traces C and D show more extended vibrational sequence structure than the $\Delta v = -1$ and 0 features. Franck-Condon factor (FCF) calculations, based on the theoretical potential energy curves, account for this behavior. The 0–0 band is predicted to have the highest FCF for the $\Delta v = 0$ group, while the FCF maximum for the $\Delta v = -2$ was for the 3–5 band. Another

interesting detail of the Δv = -2 bands was the marked difference in the contours of traces C and D at energies near 15125 cm^{-1}. The reason for this anomaly will be considered following the analysis that yields the electron affinity (EA) of BeO.

The intensity contours of the photodetachment bands were found to be significantly dependent on the excess energy imparted to the electron (with some random fluctuations caused by day-to-day variations in the laser ablation source). For example, traces A and B of Fig. 3.2 were recorded using energies that differed by 376.6 cm^{-1}. As the photon energy was lower for trace B, the slightly higher resolution was expected. However, the shift in the peak positions was not anticipated. Modeling of the rotational contours provided an explanation for this effect. With higher energy photodetachment, the band contours were dominated by detachment events where there was no change in the rotational angular momentum (i.e., $\Delta N = 0$, where N is the Hund's case (b) quantum number for the angular momentum, exclusive of spin). When the photon energy was closer to the detachment threshold, transitions with ΔN = -1,- 2, and -3 became increasingly more important. Fig. 3.4 shows an expanded view of trace B, along with a rotational structure simulation described by the following equation:

$$I_v = P_{\mathrm{v}''} \sum_T I(v) = \sum_{\mathrm{v}',N',\mathrm{v}'',N''} A_{\Delta N} P_{\mathrm{v}'',N''} * G[v - v_0(\mathrm{v}', N', \mathrm{v}'', N'')]\sigma(eKE) \quad \text{Equation 3.1}$$

where $v_0(\mathrm{v}', N', \mathrm{v}'', N'')$ is the threshold energy required to detach an electron from BeO in ro-vibration state v'', N'' and produce the neutral molecule in statev', N'. This energy is defined by the expression:

$$v_0(\mathrm{v}', N', \mathrm{v}'', N'') = EA + E(\mathrm{v}', N') - E(\mathrm{v}'', N''), \quad \text{Equation 3.2}$$

where EA is the electron affinity of BeO and the ro-vibrational energies are given by

$$E(\mathrm{v}, N) = \omega_e \mathrm{v} - \omega_e \chi_e \mathrm{v}(\mathrm{v}+1) + B_{\mathrm{v}} N(N+1) - D_{\mathrm{v}}\big(N(N+1)\big)^2. \quad \text{Equation 3.3}$$

Each transition was assigned a Gaussian line shape

$$G[v - v_0] = \sqrt{\frac{2}{\pi}}\frac{1}{\Gamma}\exp\left[-2\left(\frac{v - v_0}{\Gamma}\right)^2\right] \qquad \text{Equation 3.4}$$

with a linewidth of Δv (FWHM) and $\Gamma = \Delta v/2\ln 2$. $P_{v'',N''}$ is the ro-vibrational Boltzmann population distribution function for the anion ground state. $A_{\Delta N}$ is an intensity scaling constant for transitions with like changes in the rotational angular momentum. Lastly, $\sigma(eKE)$ is a Wigner threshold law factor [62] simplified here as $\sigma(eKE) = eKE^{l+\frac{1}{2}}$, where eKE is the kinetic energy of the ejected electron. σ was implemented in Equation 3.1 to simulate the overall intensity profiles of the images.

A value of l = 2 was found to best represent the intensity profiles based on experimentally reasonable values found for $A_{\Delta N}$ and $P_{v'',N''}$. We do not attribute a physical meaning to l and consider it to be no more than a convenient model parameter. However, l = 2 does have the effect that there will be almost no signal from photodetachment processes that are very close to threshold. Consequently, transitions where the electron kinetic energy can be increased by transferring rotational energy from the molecule (negative ΔN processes) will become favored as the energy threshold for the ΔN = 0 processes is approached. The input data for the simulation consisted of the literature values for the molecular constants of BeO, and BeO^- rotational constants derived from our theoretical calculations (Table 3.1). The vibrational term energies of BeO^- , the electron binding energy, and the rotational temperature were treated as variable parameters. As indicated in Fig. 3.4, the sharpest features of trace B corresponded to the P- and Q-branch band heads, with a lower energy feature arising from the O-branch band head. The rotational temperature of this simulation was 750 K.

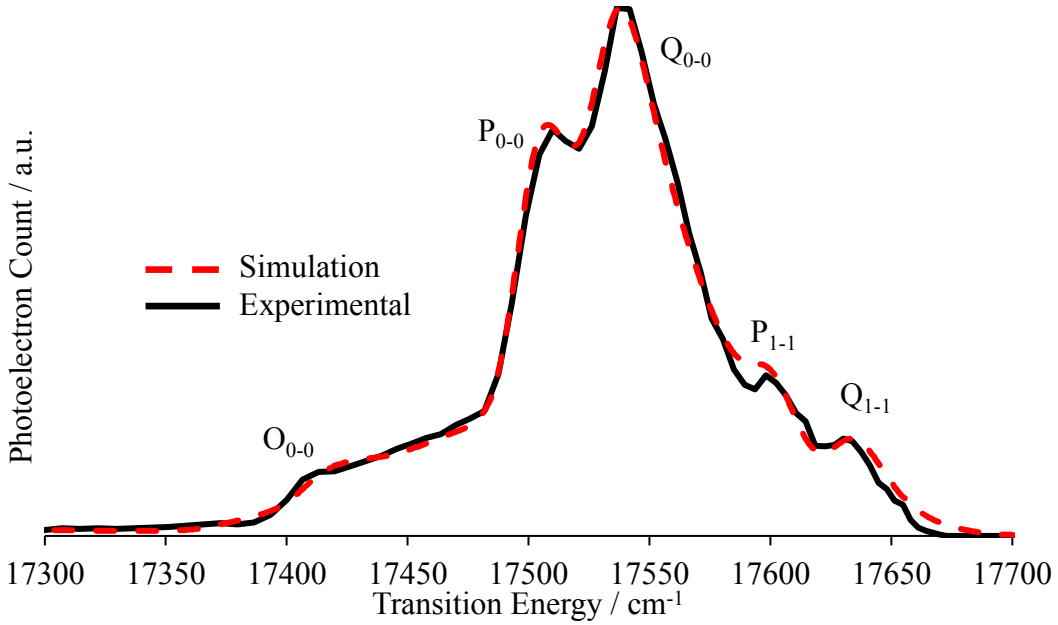

Figure 3.4. Photodetachment spectrum (solid, black) and simulation (dashed, red) of the $\Delta v = 0$ region of BeO versus transition energy. Detachment photon energy = 17733.93 cm^{-1}. Transition energy is defined as hv–eKE.

The contours of the $\Delta v = -1$ sequence bands, recorded using a detachment photon energy of 16744.75 cm^{-1}, were consistent with predominantly $\Delta N = 0$ transitions, as were the $\Delta v = -2$ bands. However, the 0 – 1 band $\Delta N = -2$ feature is observed near 16070 cm^{-1}. The intensity pattern for this $\Delta v = -1$ group was quite similar to that of the $\Delta v = 0$ sequence bands, as they appear in trace A. Note that the electron kinetic energies (energies above observed thresholds) probed in traces A and C were comparable. Likewise, when using photon energies close to threshold (traces B and D), the resulting images have similar rotational contours.

Simulations, like that shown in Fig. 3.4, were carried out for all four traces shown in Fig. 3.2. The most important fitting parameters were the anion vibrational term energies, the electron affinity of BeO, and the rotational temperature. These fits defined an electron affinity (detachment threshold) of 17535.15 cm^{-1} (2.1741 ± 0.0019 eV) and the anion vibrational

intervals listed in Table 3.1. Rotational temperatures between 600 and 750 K gave reasonable simulations. The rotational constants from the *ab initio* calculations (Table 3.1) were consistent with the observed spectrum and could not be further refined due to the limited resolution of the experimental data. It is believed that the calculated anion rotational constants are close to the true values based on the good agreement between the theory and experiment in the $\Delta G_{v+1/2}$ values and the electron affinity. Previous theoretical predictions from Jordan and Seeger[45] (2.162 eV) and Gutsev et al.[44] (2.15 eV) are also in agreement with the measured electron affinity.

Lastly, we return to the intensity anomaly exhibited near 15125 cm^{-1} within the $\Delta v = -2$ group of trace D. The anomaly corresponds to the 2–4 band and it is most likely caused by the accidental excitation of the BeO^- ($v = 3$) dipole bound state, which autodetaches to produce the BeO ($v = 2$) product. Using the above values for the EA and vibrational constants of BeO, we find that 16359 cm^{-1} excitation from BeO^- ($v = 4$) will terminate 180 ± 20 cm^{-1} below BeO ($v = 3$). This energy interval is consistent with the theoretical estimate[44] of 199 cm^{-1} for the binding energy of the electron in the first dipole bound state of BeO^-. Similar intensity anomalies, caused by the excitation of dipole bound states, were reported by Dao and Mabbs[63] in their study of the photodetachment spectrum of AuF^-.

3.5 Conclusions

The $X^2\Sigma^+ \rightarrow X^1\Sigma^+$ electronic transition of BeO^- was studied by means of photoelectron velocity map imaging spectroscopy. The detachment threshold (electron affinity) and vibrational and rotational constants of BeO^- were determined for the first time. *Ab initio* electronic structure calculations were in good agreement with the experimental results. The electron detachment characteristics were found to be dependent on the electron kinetic energy. For near threshold

detachment, channels involving multiple quanta changes in the rotational angular momenta had significant cross sections. These channels diminished as the detachment photon energy was increased, leaving $\Delta N = 0$ as the dominant channel.

3.6 Chapter 3 References

(1) S. A. Couchman, N. Holzmann, G. Frenking, D. J. D. Wilson, and J. L. Dutton. Beryllium chemistry the safe way: a theoretical evaluation of low oxidation state beryllium compounds. *Dalton Trans*. **2013,** *42*, 11375.

(2) K. J. Iversen, S. A. Couchman, D. J. D. Wilson, and J. L. Dutton. Modern organometallic and coordination chemistry of beryllium. *Coord. Chem. Rev*. **2015**, *40*, 297-298.

(3) M. C. Heaven, J. M. Merritt, and V. E. Bondybey. Bonding in beryllium clusters. *Annu. Rev. Phys. Chem*. **2011**, *62*, 375.

(4) M. C. Heaven, V. E. Bondybey, J. M. Merritt, and A. L. Kaledin. The unique bonding characteristics of beryllium and the Group IIA metals. *Chem. Phys. Lett*. **2011**, *1*, 506

(5) M. Srnec and R. Zahradnik. Diatomics AB (A = Be, Mg; B= O, S) and oligomers thereof: A theoretical study. *Chem. Phys. Lett*. **2005**, *283*, 407.

(6) A. Veldkamp and G. Frenking. STRUCTURES AND BOND-ENERGIES OF THE NOBLE-GAS COMPLEXES NGBEO (NG=AR, KR, XE). *Chem. Phys. Lett*. **1994**, *11*, 226.

(7) S. Borocci, N. Bronzolino, and F. Grandinetti. From OBeHe to $H_3BOBeHe$: Enhancing the stability of a neutral helium compound. *Chem. Phys. Lett*. **2005**, *179*, 406.

(8) R. Shinde and M. Tayade. Remarkable hydrogen storage on beryllium oxide clusters: First principles claculations. *J. Phys. Chem. C*, **2014**, *118*, 17200.

(9) M. Alipour. Theoretical determination of the differential polarizability and anisotropy of alkaline earth oxide nanoclusters (BeO)(n) [n=2-9]: The basis set and electron correlation effects. *Int. J. Quantum Chem*. **2014**, *114*, 255.

(10) L. Ren, L. Cheng, Y. Feng, and X. Wang. Geometric and electronic structures of (BeO)(N) (N=2-12, 16, 20, and 24): Rings, double rings, and cages. *J. Chem. Phys*. **2012**, *137*, 014309.

(11) Y. Qu and Y. Zhang. Structure and vibrations of BenOn (n=3-10) clusters. *Spectrochim. Acta, Part A*, **2007**, *67*, 350

(12) T. E. Field-Theodore, D. J. D. Wilson, and J. L. Dutton. Computational Predictions of the Beryllium Analogue of Borole, Cp+, and the Fluorenyl Cation: Highly Stabilized, non-Lewis Acidic Antiaromatic Ring Systems. *Inorg. Chem.* **2015**, *54*, 8035.

(13) J. Gebhardt, F. Vines, P. Bleiziffer, W. Hieringer, and A. Goerling. Hydrogen storage on metal oxide model clusters using density-functional methods and reliable van der Waals corrections. *Phys. Chem. Chem. Phys.* **2014**, *16*, 5382.

(14) V. V. Meshkov, A. V. Stolyarov, M. C. Heaven, C. Haugen, and R. J. LeRoy. Direct-potential-fit analyses yield improved empirical potentials for the ground X-1 Sigma(+)(g) state of Be-2. *J. Chem. Phys.* **2014**, *140*, 064315.

(15) J. M. Merritt, V. E. Bondybey, and M. C. Heaven. Beryllium dimer- caught in the act of bonding. *Science* **2009**, *324*, 1548.

(16) J. W. Mullinax, A. Y. Sokolov, and H. F. Schaefer. Can Density Cumulant Functional Theory Describe Static Correlation Effects? *J. Chem. Theory Comput.* **2015**, *11*, 2487.

(17) M. Lesiuk, M. Przybytek, M. Musial, B. Jeziorski, and R. Moszynski. Reexamination of the calculation of two-center, two-electron integrals over Slater-type orbitals. III. Case study of the beryllium dimer. *Phys. Rev. A: At., Mol., Opt. Phys.* **2015**, *91*, 012510.

(18) S. Chattopadhyay, R. K. Chaudhuri, and U. Sinha Mahapatra. State specific multireference perturbation theory with improve virtual orbitals: Taming the ground state of F-2, Be-2, and N-2. *J. Comput. Chem.* **2015**, *36*, 907.

(19) S. Sharma, T. Yanai, G. H. Booth, C. J. Umrigar, and G. K.-L. Chan. Spectroscopic accuracy directly from quantum chemistry: Application to ground and excited states of beryllium dimer. *J. Chem. Phys.* **2014**, *140*, 104112.

(20) L. M. Mentel and E. J. Baerends. Can the Counterpoise Correction for Basis Set Superposition Effect Be Justified? *J. Chem. Theory Comput.* **2014**, *10*, 252.

(21) M. El Khatib, G. L. Bendazzoli, S. Evangelisti, W. Helal, T. Leininger, L. Tenti, and C. Angeli. Beryllium dimer: A bond based on non-dynamical correlation. *J. Phys. Chem. A.* **2014**, *118*, 6664.

(22) X. W. Sheng, X. Y. Kuang, P. Li, and K. T. Tang. Analyzing and modeling the interaction potential of the ground-state beryllium dimer. *Phys. Rev. A: At., Mol., Opt. Phys.* **2013**, *88*, 022517.

(23) M. J. Deible, M. Kessler, K. E. Gasperich, and K. D. Jordan. Quantum monte carlo calculation of the binding energy of the beryllium dimer. *J. Chem. Phys.* **2015**, *143*, 084116.

(24) K. P. Huber and G. Herzberg, Molecular Spectra and Molecular Structure, Constants of Diatomic Molecules Vol. 4 (Litton Educational Publishing Inc., 1979).

(25) A. Lagerqvist and R. Westoo, Perturbed bands of beryllium oxide between lambda 8 000 A and lambda 10 000 A. *Ark. Mat., Astron. Fys.* **1945**, *A31*, 14.

(26) A. Lagerqvist. Pertubations in the band spectrum of beryllium oxide. *Nature* **1946**, *157*, 547.

(27) A. Lagerqvist, The energy of dissociation of BeO. *Ark. Fys.* **1954**, *7*, 473.

(28) C. A. Thompson and L. Andrews. NOBLE-GAS COMPLEXES WITH BEO - INFRARED-SPECTRA OF NG-BEO (NG = AR, KR, XE). *J. Am. Chem. Soc.* **1994**, *116*, 423.

(29) G. Verhaegen and W. G. Richards. Valence levels of beryllium oxide. *J. Chem. Phys.* **1966**, *45*, 1828.

(30) W. M. Huo, K. F. Freed, and W. J. Klemperer. Valence excited stated of BeO. *J. Chem. Phys.* **1967**, *46*, 3556.

(31) H. F. Schaefer. ELECTRON CORRELATION IN LOWEST SIGMA-1+ STATE OF BERYLLIUM OXIDE. *J. Chem. Phys.* **1971**, *55*, 176.

(32) S. V. Oneil, P. K. Pearson, and H. F. Schaefer. REPULSIVE SIGMA-3(-) AND LOW-LYING (]=1.9EV) SIGMA-3(+) STATES OF BEO. *Chem. Phys. Lett.* **1971**, *10*, 404.

(33) I. Adamovic, M. Parac, M. Hanrath, and M. Peric. Ab initio study of the electronic spectrum of BeO. *J. Serb. Chem. Soc.* **1999**, *64*, 721.

(34) C. W. Bauschlicher and D. R. Yarkony. MCSCF wavefunctions for excited states of polar molecules- Application to BeO. *J. Chem. Phys.* **1980**, *72*, 1138.

(35) G. H. F. Diercksen, A. J. Sadlej, and M. Urban. Electric properties of ionic diatoms- BeO. *Chem. Phys.* **1991**, *158*, 19.

(36) J. Irisawa and S. Iwata. Abinitio studies of the low-lying states of BeO. *Theor. Chim.* **1992**, *Acta 81*, 223.

(37) T. E. Sorensen and W. B. England. Valence states of BeO Feynman's way. *Int. J. Quantum Chem.* **2000**, *76*, 259.

(38) B. A. Thrush. The ground state of beryllium oxide. *Proc. Chem. Soc., London.* **1960**, *339*.

(39) W. Koch, J. R. Collins, and G. Frenking. ARE THERE NEUTRAL HELIUM COMPOUNDS WHICH ARE STABLE IN THEIR GROUND-STATE - A THEORETICAL INVESTIGATION OF HEBCH AND HEBEO. *Chem. Phys. Lett.* **1986**, *132*, 330.

(40) G. Frenking, W. Koch, J. Gauss, and D. Cremer. STABILITIES AND NATURE OF THE ATTRACTIVE INTERACTIONS IN HEBEO, NEBEO, AND ARBEO AND A COMPARISON WITH ANALOGS NGLIF, NGBN, AND NGLIH (NG=HE,AR) - A THEORETICAL INVESTIGATION. *J. Am. Chem. Soc.* **1988**, *110*, 8007.

(41) G. Frenking, S. Dapprich, K. F. Koehler, W. Koch, and J. R. Collins. Structure and bonding of the remarkable donor-acceptor complexes XBeO (X=NH3, NMe(3), CO, N-2, C2H2, C2H4, H-2, H2CO, O-2). *Mol. Phys.* **1996**, *89*, 1245.

(42) T. Takayanagi, H. Motegi, Y. Taketsugu, and T. Taketsugu. Accurate ab initio electronic structure calculations of the stable helium complex: HeBeO. *Chem. Phys. Lett.* **2008**, *454*, 1.

(43) H. Motegi, A. Kakizaki, T. Takayanagi, Y. Taketsugu, T. Taketsugu, and M. Shiga. Path-integral molecular dynamics simulations of BeO embedded in helium clusters: Formation of the stable HeBeO complex. *Chem. Phys.* **2008**, *354*, 38.

(44) G. L. Gutsev, M. Nooijen, and R. J. Bartlett. Valence and excited dipole-bound states of polar diatomic anions: LiH-, LiF-, LiCl-, NaH-, NaF-, NaCl-, BeO-, and MgO-. *Chem. Phys. Lett.* **1997**, *276*, 13.

(45) K. D. Jordan and R. Seeger. ABINITIO STUDY OF GROUND-STATE ANIONS OF LIF, NAF, BEO AND MGO. *Chem. Phys. Lett.* **1978**, *54*, 320.

(46) D.-Y. Hwang and A. M. Mebel. Theoretical study on the reversible storage of H- 2 by BeO. *Chem. Phys. Lett.* **2000**, *321*, 95.

(47) D. M. Neumark. Slow Electron Velocity-Map Imaging of Negative Ions: Applications to Spectroscopy and Dynamics. *J. Phys. Chem. A*, **2008**, *112*, 13287.

(48) I. Leon, Z. Yang, H.-T. Liu, and L.-S. Wang. The design and construction of a high-resolution velocity-map imaging apparatus for photoelectron spectroscopy studies of size-selected clusters. *Rev. Sci. Instrum.* **2014**, *85*, 083106.

(49) A. T. J. B. Eppink and D. H. Parker. Velocity map imaging of ions and electrons using electrostatic lenses: Application in photoelectron and photofragment ion imaging of molecular oxygen. *Rev. Sci. Instrum.* **1997**, *68*, 3477.

(50) K. J. Mascaritolo, A. M. Gardner, and M. C. Heaven. Autodetachment spectroscopy of the aluminum oxide anion dipole bound state. *J. Chem. Phys.* **2015**, *142*, 114311.

(51) M. A. Duncan. Invited Review Article: Laser vaporization cluster sources. *Rev. Sci. Instrum.* **2012**, *83*, 041101.

(52) W. C. Wiley and I. H. McLaren, *Rev. Sci. Instrum.* **1955**, *26*, 1150.

(53) C. M. Western, PGOPHER version 8.0, University of Bristol Research Data Repository, **2014**.

(54) W. Li, S. D. Chambreau, S. A. Lahankar, and A. G. Suits. Megapixel ion imaging with standard video. *Rev. Sci. Instrum.* **2005**, *76*, 063106.

(55) B. Dick. Inverting ion images without Abel inversion: maximum entropy reconstruction of velocity maps. *Phys. Chem. Chem. Phys.* **2014**, *16*, 570.

(56) C. Blondel, W. Chaibi, C. Delsart, and C. Drag. The fine structure of S and S^- measured with the photodetachment microscope. *J. Phys. B.* **2006**, *39*, 1409.

(57) H. Hotop and W. C. Lineberger. Bonding energies in atomic negative ions.2.2. *J. Phys. Chem.* **1985**, *Ref. Data 14*, 731.

(58) W. C. Martin, R. Zalubas, and A. Musgrove. Energy levels of sulfur, S-I through S-XVI. *J. Phys. Chem.* **1990**, *Ref. Data 19*, 821.

(59) H. J. Werner, P. J. Knowles, G. Knizia, F. R. Manby, and M. Schutz. Molpro: a general purpose quantum chemistry program package. *Wiley Interdiscip. Rev.: Comput. Mol. Sci.* **2012**, *2*, 242.

(60) A. Halkier, T. Helgaker, P. Jorgensen, W. Klopper, H. Koch, J. Olsen, and A. K. Wilson. Basis-set convergence in correlated calculations on Ne, N-2, and H2O. *Chem. Phys. Lett.* **1998**, *286*, 243.

(61) R. J. LeRoy, LEVEL 8.0: A Computer Program for Solving the Radial Schrodinger Equation for Bound and Quasibound Levels, University of, **2007**.

(62) E. P. Wigner, *Phys. Rev.* **1948**, *73*, 1002.

(63) D. B. Dao and R. Mabbs. The effect of the dipole bound state on AgF- vibrationally resolved photodetachment cross sections and photoelectron angular distributions. *J. Chem. Phys.* **2014**, *141*, 7.

Chapter 4

Photoelectron Detachment Spectroscopy of the Beryllium Sulfide Anion, BeS^-

The contents and figures of this chapter are reprinted or adapted with permission from

Dermer, A. R., Green, M. L., Mascaritolo, K. J., & Heaven, M. C. Photoelectron Velocity Map Imaging Spectroscopy of the Beryllium Sulfide Anion, BeS–. *The Journal of Physical Chemistry A*, **2016**, *121*(30), 5645-5650.

Slow electron velocity map imaging (SEVI) spectroscopy was used to examine the BeS^- anion to neutral ground-state transition, $X\ ^2\Sigma^+ \rightarrow X\ ^1\Sigma^+$. Rotational constants, vibrational intervals, and the electron binding energy of BeS^- were determined. Partially resolved rotational contours were seen due to the relatively small moment of inertia of beryllium sulfide. Upon analysis of the rotational contours, it was found that changes in the molecular rotational angular momentum, $\Delta N = -1, -2, -3$, and -4, facilitated photodetachment at near-threshold photon energies. The electron affinity of BeS was found to be 2.3346(2) eV. SEVI spectra recorded using photon energies near the threshold for $\Delta v = -1$ processes exhibited features that were associated with a dipole-bound state (DBS) of BeS^-. Autodetachment spectroscopy was used to probe this state, and rotationally resolved data were obtained for the DBS $^2\Sigma^+$, $v' = 0$ – X $^2\Sigma^+$, $v'' = 0$ transition. Analysis of this structure provided the rotational constants for BeS^- X, $v'' = 0$, and the electron binding energy of the DBS. Electronic structure calculations, performed at the RCCSD(T) and MRCI levels of theory, gave predictions that were in good agreement with the experimental observations.

4.1 Introduction

Diatomic beryllium compounds provide opportunities for investigations of the unusual bonding characteristics of this element.[1–7] We have recently examined the BeO^- anion[4] using the technique of slow electron velocity map imaging (SEVI) spectroscopy.[8,9] Neutral BeO is known to be a strong Lewis acid,[10,11] and its electron affinity was found to be 2.1741 ± 0.0019 eV. The additional electron of BeO^- resides in an antibonding orbital that is primarily a mixture of Be $2s/p_z$ and O $2s/p_z$ hybrid atomic orbitals. Population of this molecular orbital resulted in a slight lengthening of the bond and a decrease in the vibrational frequency. Another point of interest for

BeO^- was the observation of an electric dipole-bound electronically excited state. BeO has a relatively large electric dipole moment (6.26 D) that is sufficient to bind an electron via the charge–dipole interaction.[12] The binding energy for the dipole-bound state (DBS) was found to be 180 ± 20 cm^{-1}, validating an earlier theoretical estimate of 199 cm^{-1}.[13] Comparisons between beryllium oxide and beryllium sulfide (BeS) are of interest, as they yield insights regarding periodic trends. BeS is a potentially useful material for optoelectronic and microelectronic applications. The bulk solid has a wide band gap (~4.26 eV), making it suitable for the production of blue-green laser diodes.[14,15] Theoretical studies predict that solid BeS may be used for the reversible storage of hydrogen.[16] Furthermore, it is predicted that diatomic BeO[10,17] and BeS can form remarkably robust physical bonds with rare-gas atoms. Experimental evidence supporting the latter prediction has been provided by studies of matrix-isolated BeO[19] and BeS.[18]

There have been several spectroscopic and theoretical studies of BeS.[16,18,20–27] The $X\ ^1\Sigma^+$ ground state has been characterized by means of electronic spectroscopy.[25,28] Electronic structure calculations have been used to predict the properties of the ground and lower-energy excited states.[20–24] Of particular interest for the present study, the calculated electric dipole moment for BeS is ~5.0 D.[20,23] This dipole moment is large enough that the BeS^- anion is expected to support at least one DBS. To date, there have been no published reports of experimental or theoretical studies of BeS^-. In the present work, we examined the anion by means of SEVI and autodetachment spectroscopies. These measurements provided the electron affinity of BeS and vibration–rotation constants for the $X\ ^2\Sigma^+$ ground state of the anion. A DBS, located ~140 cm^{-1} below the electron detachment threshold, was characterized by means of both SEVI and autodetachment techniques. Theoretical calculations for BeS^- were performed using coupled cluster and multireference configuration interaction methods.

4.2 Experimental Methods

A complete description of the instrumentation used for these experiments is provided in ref 4, and a summary of details specific to BeS is provided here. Beryllium sulfide anions were formed via pulsed laser ablation[29] of a Be rod in the presence of He (25 psia) seeded with CS_2 (room temperature vapor pressure). Ablation was accomplished using the second harmonic of a Nd:YAG laser (532 nm) operating with a pulse energy of ~8 mJ. The ablation products were supersonically expanded into a differentially pumped vacuum chamber that housed a Wiley–McLaren time-of-flight mass spectrometer[30] (WM-TOFMS). The axis of the mass spectrometer was perpendicular to the direction of the supersonic expansion. Within the mass spectrometer the anions were accelerated into a drift region, where they were directed by an Einzel lens and four sets of deflector plates. A fifth set of deflector plates could be used as a mass gate for selection of the anions of interest.

The anions were directed through the center of a velocity map imaging lens. This 3-electrode component was modeled after the design of Eppink and Parker.[31] Photodetachment of BeS^- was induced by the focused beam from a tunable dye laser (both Nd:YAG and excimer pumped dye lasers were used in these measurements). The laser beam was propagated along an axis that was perpendicular to the direction of the anion beam. Photon energies were chosen to be above the detachment threshold of BeS^- with an energy of 0.5–1 mJ per pulse and beam diameter less than 2 mm. The photodetachment lasers were frequency calibrated using the B–X absorption spectrum of room-temperature I_2 vapor, with line positions provided by the PGOPHER software package.[32]

Following photodetachment, the VMI optics focused the electrons onto a set of imaging quality microchannel plates (MCPs) paired with a phosphor screen. A CCD camera recorded the images,

which were averaged over several hundred thousand laser pulses using the imaging collection software designed by Li et al.[33] The images were analyzed using the MEVELER program.[34] The MCPs were pulsed so that only the detached photoelectrons were detected. Mu-metal shielding surrounding the photodetachment and electron drift regions minimized distortions due to external magnetic and electric fields. A photomultiplier tube (PMT) was positioned off-axis of the phosphor screen to monitor phosphor screen emission. This detection method allowed for the optimization of the anion and photoelectron signals. The BeS^- velocity map images were calibrated using the known detachment transitions of S^-.[35]

SEVI data were recorded using fixed frequency excitation. Owing to the presence of a DBS of BeS^-, we were also able to record an autodetachment spectrum. For this measurement the phosphor screen was masked such that only the light from the center of the screen was observed. The total intensity of this signal was recorded as a function of the excitation laser frequency. Autodetachment spectra were also recorded using an annular mask that selectively detected electrons with energies in the range of 850 ± 200 cm^{-1}. The rationale for this measurement is explained in the following sections.

4.3 Theoretical Calculations

BeS is a closed-shell ionic species with an experimentally verified X $^1\Sigma^+$ ground state. The unpaired electron of BeS^- resides in an orbital that is primarily of Be $2s/p_z$ – S $3s/p_z$ antibonding character, giving rise to a X $^2\Sigma^+$ ground state. Electronic structure calculations were performed on both the anion and neutral beryllium sulfide molecules. These calculations were done to assist in the assignment of the spectra and to evaluate the suitability of the chosen electronic structure methods. For beryllium, the aug-cc-pwCVQZ basis set was employed,

whereas the aug-cc-pCVQZ was used for sulfur. In our studies[4] of BeO/BeO^- we found that it was advantageous to use density functional theory B3LYP wavefunctions as the reference set for the higher-order calculations. Hence, the same approach was taken for BeS/ BeS^-.

All calculations were performed using the MOLPRO suite of programs.[36] Potential energy curves (PECs) were calculated pointwise. One series of calculations used the partially spin-adapted coupled cluster method including single and double excitations and perturbative corrections for triple excitations (RCCSD(T)). The second method employed was a complete active space self-consistent field calculation, followed by multireference configuration interaction (CASSCF+MRCI+Q, denoted as MRCID in the following text) levels of theory. The Davidson correction[37] was applied to partially compensate for the size inconsistency of the MRCI calculations.

All electrons were included in the correlation treatment of the RCCSD(T) calculations. The active space in the CASSCF calculations consisted of the 2s and 2p orbitals of Be and the 2s, 2p, 3s, and 3p orbitals of S. The Be 1s and S 1s orbitals were constrained to be doubly occupied. Their wavefunctions were optimized in the CASSCF procedure to aid convergence. For both the anion and neutral BeS species, all electrons were included in the correlation treatment of the subsequent MRCI calculation, in an attempt to recover the core–valence correlation energy. The PECs of the RCCSD(T) calculations are shown in Figure 4.1. Overall, the MRCID results were of comparable quality, with the exception that the error for the electron binding energy (eBE), as compared to the experimental result, was larger.

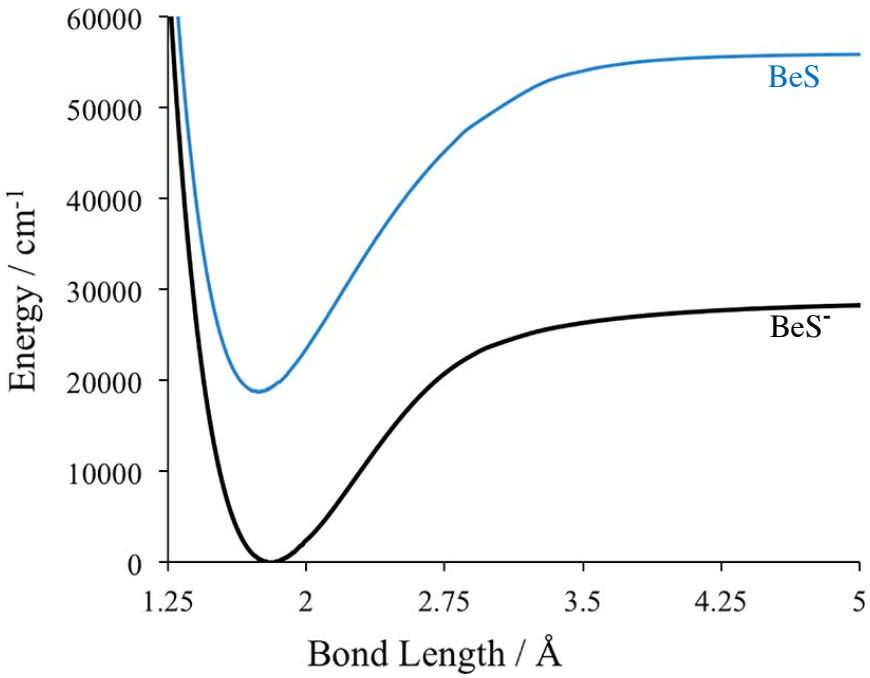

Figure 4.1. PECs for the BeS ground state (black) and BeS ground state (blue). Calculations performed with the CCSD(T) method and the augmented cc-pVQZ basis set. See text for details.

The bound ro-vibrational levels of the PECs were calculated using the LEVEL 8.0 program.[38] The lowest vibrational energy levels were least-squares fit to the standard Morse energy level expression, yielding effective values for ω_e and $\omega_e\chi_e$. The predicted molecular constants are listed in Table 4.1, which includes the experimentally determined constants for BeS. Our calculations are in respectable agreement with the latter, indicating that an appropriate level of theory was applied. As observed for BeO/BeO^-, the addition of an electron to BeS lengthens the bond and reduces the vibrational frequency. Predictions for the electron affinity were made with the inclusion of the zero-point vibrational energies. Franck–Condon factors (FCFs) for the $BeS^- \rightarrow BeS + e-$ detachment transitions were calculated by LEVEL[38] using the RCCSD(T) PECs. The relevant subset of FCFs is presented in Table 4.2.

Table 4.1. Theoretical and Experimental Spectroscopic Parameters[a] for BeS^- and BeS.

BeS			
	Exp.[28]	B3LYP-CCSD(T)	MRCI
ω_e	997.94	1000.4	994.5
$\omega_e x_e$	6.137	6.00	6.02
R_e	1.7415	1.7425	1.7465
B_e	0.79059	0.7897	0.7861
α_e	0.00664	0.0066	0.0066
BeS^-			
	Exp.	B3LYP-CCSD(T)	MRCI
eBE	18830 ± 17	18740.5	17863
ω_e	917.31 ± 1.33	906.7	901.6
$\omega_e x_e$	7.73 ± 0.25	5.83	5.30
$\Delta G_{1/2}$	894 ± 8	895.0	891.0
$\Delta G_{3/2}$	878 ± 15	883.4	880.4
$\Delta G_{5/2}$	864 ± 26	871.7	869.8
R_e	1.806± 0.004	1.8077	1.8093
B_e	0.735 ± 0.003	0.733	0.732
α_e	0.0056 ± 0.001	0.0061	0.0065
D_e	1.97 x 10^{-6}	1.95x10^{-6}	2.0 x 10^{-6}

[a] All values are in units of wavenumbers (cm^{-1}), except R_e, which is in units of Angstroms (Å)

Table 4.2 Franck–Condon Factors for the BeS^- (X, v'') → BeS(X, v') + e– Photodetachment Transition

v'/v''	0	1	2	3	4	5
0	0.691	0.243	0.054	0.010	0.002	0.000
1	0.267	0.274	0.304	0.117	0.004	0.007
2	0.039	0.375	0.073	0.270	0.164	0.058
3	0.003	0.098	0.384	0.004	0.197	0.186
4	0.000	0.010	0.161	0.337	0.009	0.297

4.4 Results and Discussion

4.4.1 SEVI Spectroscopy

Overview SEVI spectra for BeS , recorded using detachment photon energies of 18950 and 19262 cm^{-1}, are shown in Figure 4.2. The horizontal axis of this figure gives the transition energy, which is defined by the photon energy (hν) minus the electron kinetic energy (eKE). The vertical axis is the transformed image intensity, integrated over the angular distribution, and is proportional to photoelectron counts.

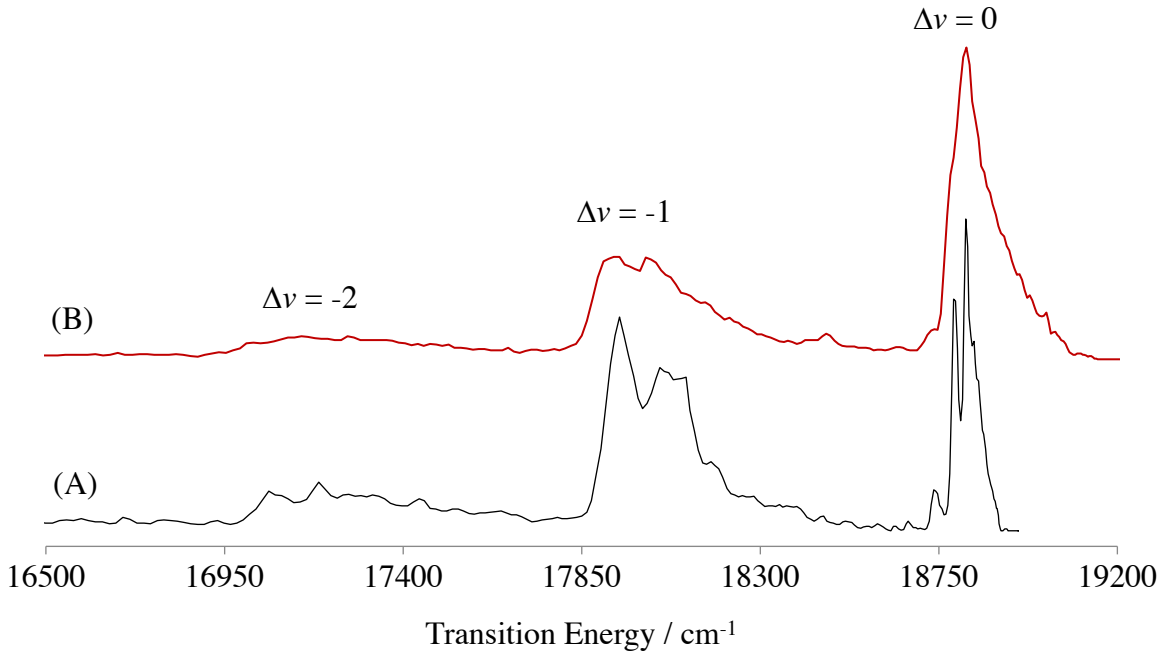

Figure 4.2 Photodetachment spectra for BeS^- recorded using photon energies of 19,262 cm^{-1} (trace (B)) and 18,950 cm^{-1} (trace (A)). The transition energy is equal to hν – eKE.

The images were almost perfectly isotopic, as can be seen in the reconstructed VMI image in Figure 4.3, yielding anisotropy parameters that were close to zero. On the basis of the vibrational constants of Table 4.1, the three main features of these spectra are readily assigned.

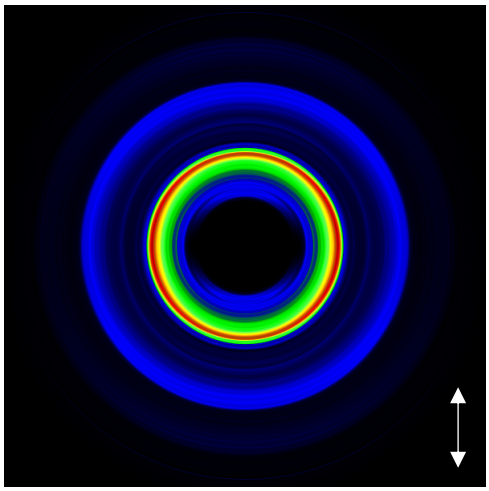

Figure 4.3. Reconstructed velocity map image of BeS- → BeS transitions, corresponding to the 19262 cm^{-1} photodetachment spectrum (Trace B in Figure 4.2). The double headed arrow indicates the polarization of the photodetachment laser.

From high to low energy they consist of $\Delta v = 0, -1$, and -2 photodetachment events. The resolution of SEVI spectroscopy improves with decreasing eKE. This effect is clearly apparent in Figure 4.2, where the structure of the $\Delta v = 0$ feature begins to resolve as the photon energy approaches the detachment threshold. Expanded spectra recorded with near-threshold detachment of the $\Delta v = 0, -1$, and -2 features are presented in Figure 4.4. Here it can be seen that there is a red shift of the main peak in trace A (lower-energy detachment photon), relative to trace B. This same behavior was observed for the $\Delta v = 0$ features of the BeO^- SEVI spectra using comparable above-threshold detachment energies. [4] In the latter study this effect was explained by considering the dependence of the photodetachment cross-section on the energy above threshold.

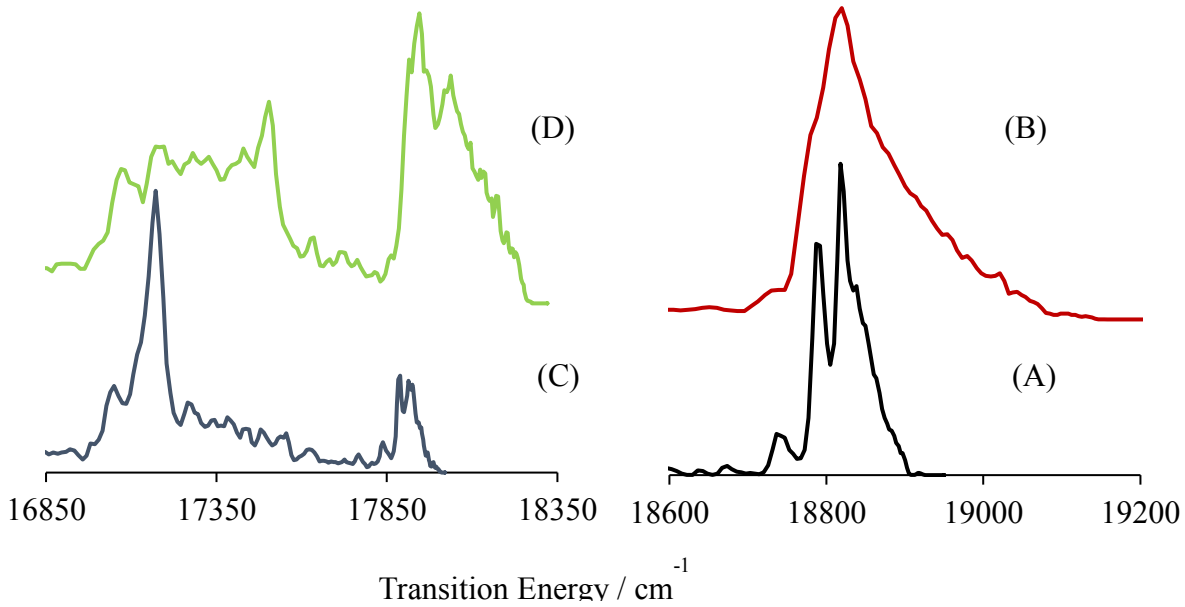

Figure 4.4. SEVI Spectra of BeS^- at various photon energies(A) Black, photon energy = 18949.9 cm^{-1}. (B) Red, 19261.5 cm^{-1}. (C) Blue, 18020.0 cm^{-1}. (D) Green, 18320.1 cm^{-1}. (A, B) $\Delta v = 0$ detachment channels. (C, D) $\Delta v = -1$ and $\Delta v = -2$ detachment channels. The transition energy is equal to $h\nu$ – eKE.

The Wigner threshold law predicts that the cross-section (σ) will be governed by the expression $\sigma \propto eKE^{(l+1/2)}$, where l is the angular momentum of the detached electron.[9] When l is greater than 0 the cross-section drops to very low values just above threshold. However, the transfer of rotational energy can augment the energy available to the electron. When the photon energy is well-above threshold, $\Delta N = 0$ processes dominate (where N is the rotational angular momentum, exclusive of spin). As the photon energy approaches the threshold the $\Delta N < 0$ processes become increasingly more important. As the band heads of the $\Delta N < 0$ rotational branches are below the band origins, their increased contributions result in a red shift of the rotational band contours. A model of the rotational contours that includes this behavior was described in ref 4. This model was applied to the data for BeS^-, and the fit to the $\Delta = 0$ contour is shown in Figure 4.5. The vibration–rotation constants used for BeS(X) were taken from the

literature[28] (Table 4.1). The computed values for the $BeS^-(X)$ molecular constants (Table 4.1, RCCSD(T) results) were used as the starting guess for the simulations. These constants and the electron affinity were systematically refined to obtain the best agreement with the experimental data. Transitions from several vibration levels contributed to the contours, and the data were consistent with a high internal energy content for the anion. Simulations that assumed a Boltzmann distribution for the rotational level populations did not give optimal results. Improved fits were achieved when a two-temperature distribution was assumed, of the form

$$P(N) = (2N+1)(a_1 * e^{-\frac{E(N)}{k_B T_1}} + a_2 * e^{-\frac{E(N)}{k_B T_2}}) \qquad \text{Equation 4.1}$$

Where $E(N)$ is the rotational energy, k_B is the Boltzmann constant, T_1 and T_2 are temperatures and a_1 and a_2 are fractional coefficients. Population distributions of this kind are not uncommon

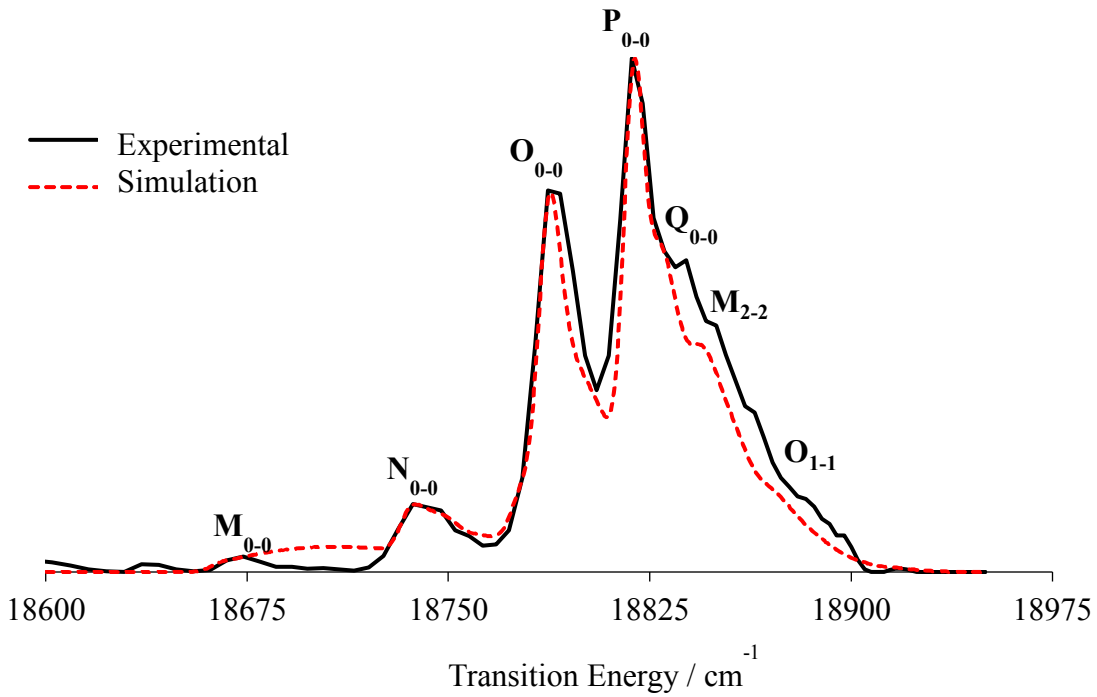

Figure 4.5. SEVI spectrum (solid black line) of the $\Delta v = 0$ region of BeS^- and simulation (broken red line). The photon energy was 18 949.9 cm^{-1}. The transition energy is equal to hν – eKE.

in jet expansions, where cooling of the higher energy rotational states is kinetically limited by the rate of expansion.[39] The simulated contour is compared to the observed spectrum in Figure 4.5. The labels M, N, O, P, Q correspond to the band heads of the $\Delta N = -4, -3, -2, -1$, and 0 rotational branches, respectively. The subscripts provide the upper and lower state vibrational assignments. For this simulation, the rotational temperatures were set to $T_1 = 150$ K and $T_2 = 500$ K. The value for l was set to 3. As in our study of BeO^-, we consider this to be simply a model parameter, not indicative of the electronic angular momentum.[4] Another trend that is evident in Figure 4.4 concerns the widths of the $\Delta v = 0, -1$, and -2 features. The bands become broader as $|\Delta v|$ increases. Inspection of Table 4.2 shows that this is caused by the distribution of the Franck–Condon factors. The BeS electron affinity and BeS^- molecular constants resulting from fitting to all of the contours ($\Delta v = 0, -1$, and -2) are listed in Table 4.1. We speculate that the large number of rotational states populated under the conditions of these measurements, combined with photodetachment channels that convert rotational energy into electron recoil energy, were responsible for the effectively isotropic angular distributions observed in the velocity map images.

In Figure 4.4, traces C and D show SEVI spectra recorded using photon energies (18020 and 18320 cm^{-1}) that were close to the energetic of thresholds of the $\Delta v = -1$ processes. Each trace had a prominent peak imposed on the $\Delta v = -2$ contour, centered at 17172 cm^{-1} in trace C and 17504 cm^{-1} in trace D. Similar peaks were observed for spectra recorded with photon energies within the 17612–18320 cm^{-1} range. The peak was systematically shifted from the photon energy by 850 ± 25 cm^{-1}. We assign this feature to a dipole-bound state of BeS^- (DBS, $v = 1$) that lies 136 ± 25 cm^{-1} below the BeS (X, $v = 1$) + e– detachment threshold. The almost constant shift between the peak center and the photon energy indicates that the vibrational

autodetachment process $BeS^-(DBS, v = 1) \rightarrow BeS\ (X, v = 0) + e-$ was dominated by $\Delta N = 0$ events. This process is illustrated in the energy-level diagram of Figure 4.6.

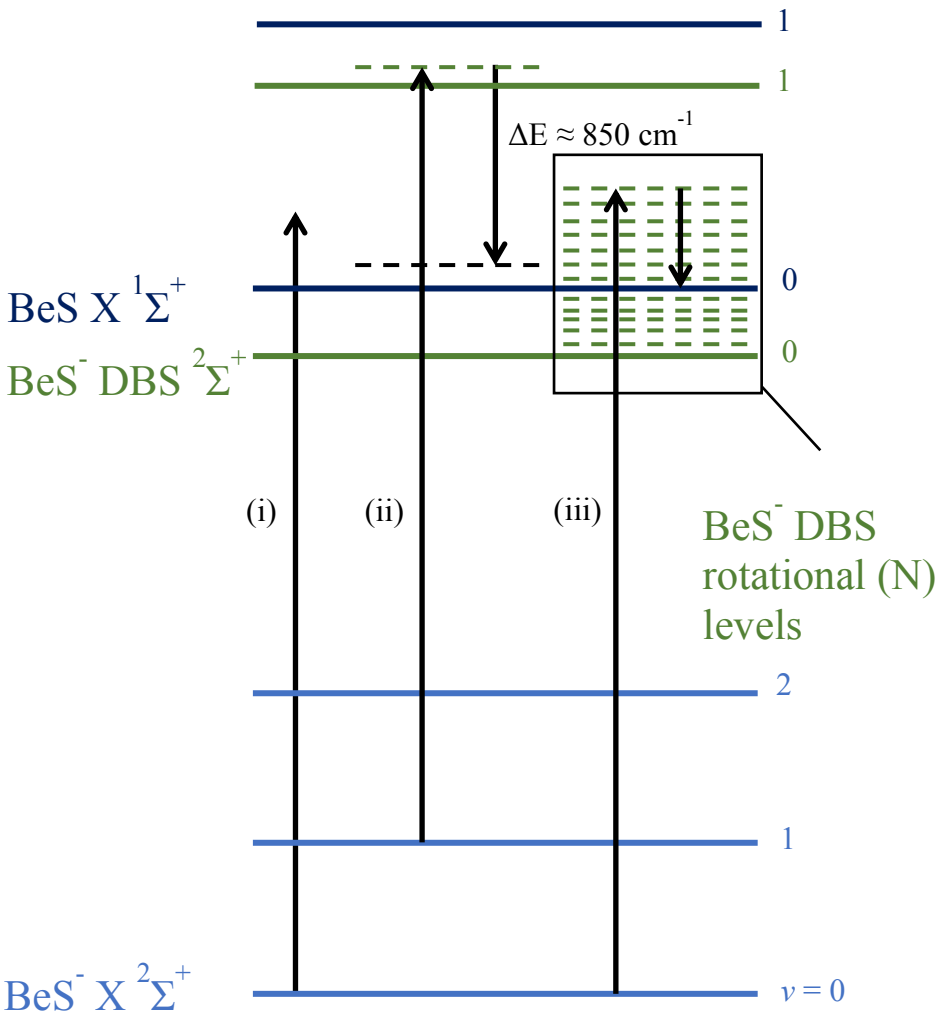

Figure 4.6 Energy-level diagram showing BeS^- photodetachment processes. The vertical transitions labeled (i) and (ii) correspond to the features seen at 17910 and 17172 cm^{-1} in Figure 4.3c. Transition (i) is direct photodetachment via the 0–1 band, while transition (ii) results in excitation of the BeS^- DBS $^2\Sigma^+$, $v = 1$ level. Vibrational autodetachment from this level, with $\Delta N = 0$, produces electrons with a kinetic energy of ~850 cm^{-1}. Transition (iii) represents excitation of rotational levels of BeS^- DBS $v = 0$ that have sufficient energy to undergo rotational autodetachment.

4.4.2 Autodetachment Spectroscopy

To check the assignment of the DBS features, the photodetachment spectrum was examined. This measurement was initially focused on the BeS^- (DBS, v = 0) level. Rotational constants for the DBSs of anions are very close to those of the neutral molecule. Using the constant $B_0 = 0.7873$ cm^{-1} for BeS (X, v = 0) and the observation that the DBS was ~140 cm^{-1} below the detachment threshold, it was estimated that levels with $N \geq 14$ would be subject to rotational autoionization. The resulting electrons would have low kinetic energies. To observe these events, the phosphor screen was masked so that only the signal from a central aperture, corresponding to electrons with kinetic energies in the range of 0–100 cm^{-1}, was registered. This

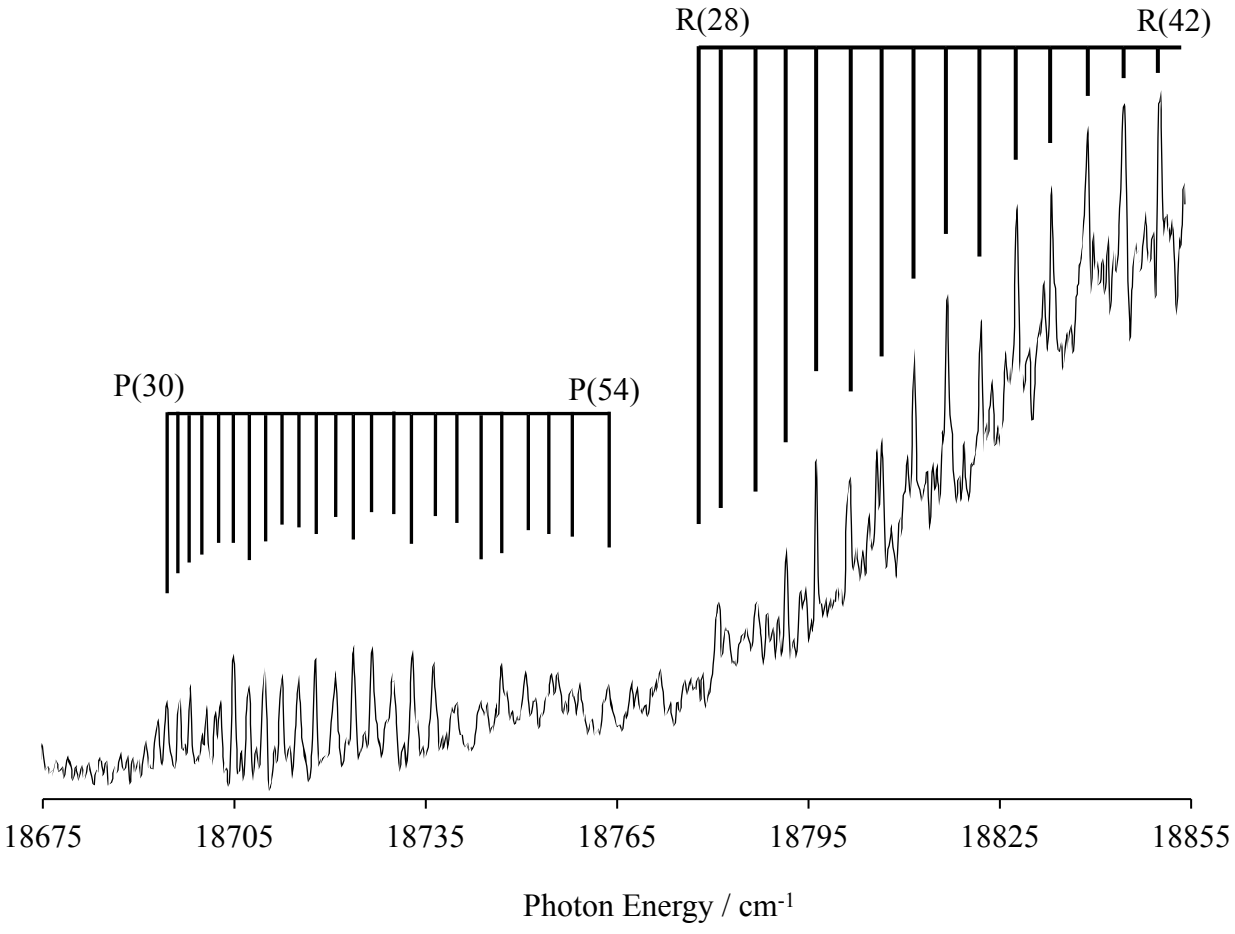

Figure 4.7. DBS $^2\Sigma^+$, $v' = 0$ – X $^2\Sigma^+$, $v'' = 0$ BeS^- photodetachment spectrum

Table 4.3 BeS^- Molecular constants (cm^{-1}) derived from the DBS $^2\Sigma^+$, $v' = 0 \leftarrow X\ ^2\Sigma^+$, $v'' = 0$ transition

State	T_0	B_0	D_0
$X\ ^2\Sigma^+$	0.0	0.731(1)	$1.5(4) \times 10^{-6}$
DBS $^2\Sigma^+$	18689.0(1)	0.7873[a]	2.0×10^{-6} [a]

[a] Fixed at the values for BeS $X\ ^1\Sigma^+$, v = 0 taken from ref 28.

signal was monitored as a function of the excitation laser photon energy. The spectrum obtained is shown in Figure 4.7. This trace consists of sharp autodetachment resonances superimposed on the direct photodetachment background. The resolution of the sharp lines was limited by the laser line width, indicating that rotational autodetachment process was relatively slow. The rotational structure of this band was assigned using upper-state combination differences, followed by a fit to the lower-state rotational constants and band origin energy by means of the program POPHER.[32] The constants obtained from this fit are listed in Table 4.3. Note that the b

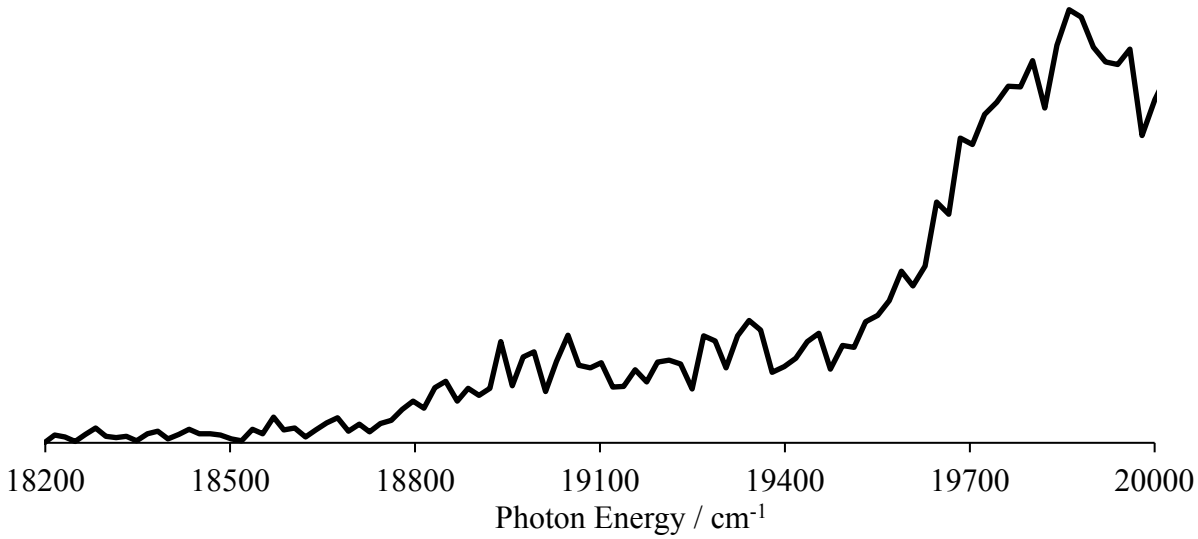

Figure 4.8 DBS $^2\Sigma^+$, $v' = 1 - X\ ^2\Sigma^+$, $v'' = 0$ BeS^- photodetachment spectrum. The noise level for this measurement is indicated by the signal fluctuations evident in the 18200–18500 cm^{-1} range.

and shows only P and R branches, indicating a DBS $^2\Sigma^+$ – X $^2\Sigma^+$ transition. Rotational line assignments are indicated for the 0–0 band. Lines of the 1–1 band are also present, but they were not labeled to avoid congestion. The origin of the 0–0 band is 141 ± 17 cm^{-1} below the detachment threshold, where the uncertainty is defined by our measurement of the latter. This value is consistent with our interpretation of the DBS features of the SEVI spectra, which indicate that the BeS^- (DBS, $v = 1$) level is 136 ± 25 cm^{-1} below BeS (X, $v = 1$) + e–. Finally, we examined the DBS – X 1–0 transition using vibrational autodetachment spectroscopy (BeS^- (DBS, $v = 1$) → BeS (X, $v = 0$) e^-). The electrons produced by this process were expected to be emitted with kinetic energies near 850 cm^{-1}. Consequently, an annular mask was placed on the phosphor screen to limit the detection to electrons with energies within the range of 850 ± 200 cm^{-1}. The photodetachment spectrum resulting from this measurement is shown in Figure 4.8. The intensity contour of this band reflects the same rotational structure as that of Figure 4.7 (again, superimposed on the direct detachment threshold), but the resolution was not high enough to reveal individual rotational lines.

4.5 Conclusions

The electron affinity (EA) of BeS (18830(17) cm^{-1} = 2.3346(2) eV) has been determined for the first time. This value is higher than the EA of BeO (2.174(2) eV), which probably reflects the greater EA of S. SEVI and autodetachment spectroscopy techniques were used to characterize the vibration–rotation constants of BeS^- (X $^2\Sigma^+$). It was found that the bond length of BeS^- was greater than that of BeS, while the vibrational frequency was diminished. These changes were consistent with the outermost electron of BeS^- residing in the Be $2s/p_z$ – S $3s/p_z$ antibonding orbital. High-level electronic structure calculations supported this interpretation,

yielding predictions that were in good agreement with the EA of BeS and the molecular constants of BeS^-.

A dipole-bound state of BeS^- was observed 141(17) cm^{-1} below the electron detachment threshold. The electron binding energy for this state is comparable to those of the first DBSs of BeO^- (180(20) cm^{-1}) and AlO^- (52(6) cm^{-1}).[40] In this series the binding energies correlate with the electric dipole moments of the neutral molecules.

4.6 Chapter 4 References

(1) Couchman, S. A.; Holzmann, N.; Frenking, G.; Wilson, D. J. D.; Dutton, J. L. Beryllium chemistry the safe way: A theoretical evaluation of low oxidation state beryllium compounds. Dalton Trans. **2013**, *42*, 11375–11384.

(2) Iversen, K. J.; Couchman, S. A.; Wilson, D. J. D.; Dutton, J. L. Modern organometallic and coordination chemistry of beryllium. *Coord. Chem. Rev.* **2015**, 297–298, 40–48.

(3) Barker, B. J.; Antonov, I. O.; Merritt, J. M.; Bondybey, V. E.; Heaven, M. C.; Dawes, R. Experimental and theoretical studies of the electronic transitions of BeC. *J. Chem. Phys.* **2012**, *137*, 214313.

(4) Mascaritolo, K. J.; Dermer, A. R.; Green, M. L.; Gardner, A. M.; Heaven, M. C. Photodetachment spectroscopy of the beryllium oxide anion, BeO^-. *J. Chem. Phys.* **2017**, *146*, 054301.

(5) Heaven, M. C.; Merritt, J. M.; Bondybey, V. E. Bonding in beryllium clusters. *Annu. Rev. Phys. Chem.* **2011**, *62*, 375–93.

(6) Heaven, M. C.; Bondybey, V. E.; Merritt, J. M.; Kaledin, A. L. The unique bonding characteristics of beryllium and the Group IIA metals. *Chem. Phys. Lett.* **2011**, *506*, 1–14.

(7) Dutton, J. L.; Frenking, G. New avenues in s-block chemistry: Beryllium (0) complexes. *Angew. Chem., Int. Ed.* **2016**, *55*, 13380– 13382.

(8) Neumark, D. M. Probing chemical dynamics with negative ions. *J. Chem. Phys.* **2006**, *125*, 132303.

(9) Neumark, D. M. Slow electron velocity-map imaging of negative ions: Applications to spectroscopy and dynamics. *J. Phys. Chem. A* **2008**, *112*, 13287–13301.

(10) Veldkamp, A.; Frenking, G. Structures and bond energies of the noble gas complexes NgBeO (Ng = Ar, Kr, Xe). *Chem. Phys. Lett.* **1994**, *226*, 11–16.

(11) Frenking, G.; Dapprich, S.; Koehler, K. F.; Koch, W.; Collins, J.R. Structure and bonding of the remarkable donor-acceptor complexes XBeO (X = NH_3, NMe_3, CO, N_2, C_2H_2, C_2H_4, H_2, H_2CO, O_2). *Mol. Phys.* **1996**, *89*, 1245–1263.

(12) Jordan, K. D. Negative ion states of polar molecules. *Acc. Chem. Res.* **1979**, *12*, 36–42.

(13) Gutsev, G. L.; Nooijen, M.; Bartlett, R. J. Valence and excited dipole-bound states of polar diatomic anions: LiH^-, LiF^-, $LiCl^-$, NaH^-, NaF^-, $NaCl^-$, BeO^-, and MgO^-. *Chem. Phys. Lett.* 1997, *276*, 13–19.

(14) Benosman, N.; Amrane, N.; Mecabih, S.; Aourag, H. Structural and electronic properties of bulk BeS. *Phys. B* 2001, *304*, 214–220.

(15) Heciri, D.; Beldi, L.; Drablia, S.; Meradji, H.; Derradji, N. E.; Belkhir, H.; Bouhafs, B. First-principles elastic constants and electronic structure of beryllium chalcogenides BeS, BeSe and BeTe. *Comput. Mater. Sci.* **2007**, *38*, 609–617.

(16) Hwang, D.-Y.; Mebel, A. M. Theoretical study of the reversible storage of H2 by BeS. *J. Am. Chem. Soc.* **2000**, *122*, 11406–11410.

(17) Takayanagi, T.; Motegi, H.; Taketsugu, Y.; Taketsugu, T. Accurate ab initio electronic structure calculations of the stable helium complex: HeBeO. *Chem. Phys. Lett.* **2008**, *454*, 1–6.

(18) Wang, Q.; Wang, X. Infrared spectra of NgBeS (Ng = Ne, Ar,Kr, Xe) and BeS_2 in noble-gas matrices. *J. Phys. Chem. A* **2013**, *117*, 1508–1513.

(19) Thompson, C. A.; Andrews, L. Noble gas complexes with BeO: Infrared spectra of NG-BeO (NG = Ar, Kr, Xe). *J. Am. Chem. Soc.* **1994**, *116*, 423–4.

(20) De Oliveira-Filho, A. G. S.; Alves, T. V.; Ribas, V. W.; Ferrao, L. F. A.; Roberto-Neto, O.; Machado, F. B. C.; Ornellas, F. R. A CASSCF/MRCI study of the low-lying electronic states of the BeS molecule. *Int. J. Quantum Chem.* **2011**, *111*, 1694–1700.

(21) Larbi, T.; Khadri, F.; Ghalila, H.; Lahmar, S.; Hochlaf, M. Theoretical spectroscopy and metastability of BeS and its cation. *Chem. Phys.* **2010**, *373*, 193–202.

(22) Liu, H.; Xing, W.; Shi, D.-H.; Sun, J.-F. Investigation on spectroscopic parameters and molecular constants of BeS ($X^1\Sigma^+$) using MRCI theory. *Yuanzi Yu Fenzi Wuli Xuebao* **2012**, *29*, 216–222.

(23) Noga, J.; Pluta, T. Coupled cluster calculations of the electric properties of BeS. An analysis of the fifth-order non-iterative corrections. *Chem. Phys. Lett.* **1997**, *264*, 101–108.

(24) Partridge, H.; Langhoff, S. R.; Bauschlicher, C. W., Jr. Theoretical study of the alkali and alkaline earth monosulfides. *J. Chem. Phys.* **1988**, *88*, 6431–7.

(25) Pouilly, B.; Robbe, J. M.; Schamps, J.; Field, R. W.; Young, L. Perturbations in the $A^1\Pi$-$X^1\Sigma^+$ system of the beryllium sulfide molecule. The $a^3\Pi_i$ state. *J. Mol. Spectrosc.* **1982**, *96*, 1–55.

(26) Rai, D. P.; Ghimire, M. P.; Thapa, R. K. A DFT study of BeX (X= S, Se, Te) semiconductor: Modified Becke Johnson (mBJ) potential. *Semiconductors* **2014**, *48*, 1411–1422.

(27) Srnec, M.; Zahradnik, R. Diatomics AB (A = Be, Mg; B = O, S) and oligomers thereof: A theoretical study. Chem. Phys. Lett. **2005**, *407*, 283–288.

(28) Cheetham, C. J.; Gissane, W. J. M.; Barrow, R. F. Electronic spectra of the BeS molecule. *Trans. Faraday Soc.* **1965**, *61*, 1308–16.

(29) Duncan, M. A. Laser vaporization cluster sources. *Rev. Sci. Instrum.* **2012**, *83*, 19.

(30) Wiley, W. C.; McLaren, I. H. Time-of-flight mass spectrometer with improved resolution. *Rev. Sci. Instrum.* **1955**, *26*, 1150–1157.

(31) Eppink, A. T. J. B.; Parker, D. H. Velocity map imaging of ions and electrons using electrostatic lenses: Application in photoelectron and photofragment ion imaging of molecular oxygen. *Rev. Sci. Instrum.* **1997**, *68*, 3477–3484.

(32) Western, C. M. PGOPHER, version 8.0; *University of Bristol Research Data Repository*, **2014.**

(33) Li, W.; Chambreau, S. D.; Lahankar, S. A.; Suits, A. G. Megapixel ion imaging with standard video. *Rev. Sci. Instrum.* **2005**, *76*, 063106.

(34) Dick, B. Inverting ion images without Abel inversion: Maximum entropy reconstruction of velocity maps. *Phys. Chem. Chem. Phys.* **2014,** *16*, 570–80.

(35) Blondel, C.; Chaibi, W.; Delsart, C.; Drag, C. The fine structure of S and S– measured with the photodetachment microscope. *J. Phys. B: At., Mol. Opt. Phys.* **2006**, *39*, 1409–1416.

(36) Werner, H. J.; Knowles, P. J.; Knizia, G.; Manby, F. R.; Schutz, M. Molpro: a general-purpose quantum chemistry program package. *Wiley Interdisciplinary Reviews-Computational Molecular Science* **2012**, *2*, 242–253.

(37) Davidson, E. R.; Silver, D. W. Size consistency in the dilute helium gas electronic structure. *Chem. Phys. Lett.* **1977**, *52*, 403–6.

(38) LeRoy, R. J. LEVEL 8.0, A Computer Program for Solving the Radial Schrödinger Equation for Bound and Quasibound Levels; Chemical Physics Research Report CP-663; *University of Waterloo*, **2007**.

(39) Heaven, M.; Miller, T. A.; Bondybey, V. E. Production and characterization of temperature-controlled free radicals in a free jet expansion. *Chem. Phys. Lett.* **1981**, *84*, 1–5.

(40) Mascaritolo, K. J.; Gardner, A. M.; Heaven, M. C. Autodetachment spectroscopy of the aluminum oxide anion dipole bound state. *J. Chem. Phys.* **2015**, *143*, 114311.

Chapter 5

Dative Bonding Between Closed-Shell Atoms: The BeF^- Anion

The contents and figures of this chapter are reprinted or adapted with permission from Green, M. L., Jean, P., & Heaven, M. C. Dative Bonding between Closed-Shell Atoms: The BeF–Anion. *The Journal of Physical Chemistry Letters*, **2018**, *9(8),* 1999-2002.

Beryllium can exhibit unusually strong attractive interactions under conditions where it is nominally a closed-shell atom. Two prominent examples are the Be_2 dimer and the He–BeO complex. In the present study, we examine the bonding of the closed-shell Be–F^- anion. This molecule preserves the closed-shell character of the individual atoms as the electron affinity of F is high (328.16 kJ/mol^{-1}) while that of Be is negative. Photodetachment spectroscopy was used to determine the vibrational frequency for BeF^- and the electron affinity of BeF (104.2 kJ/mol^{-1}). The latter has been used to determine a lower bound of 343 kJ/mol^{-1} for the bond energy of BeF^-. Electronic structure calculations yielded predictions that were in good agreement with the observed data. A natural bond orbital analysis shows that BeF^- is primarily bound by a dative interaction.

5.1 Introduction

The bonding of beryllium in small molecules often displays characteristics that are notably different from those of the heavier group IIA elements.[1,2] Probably the best-known example is the Be_2 dimer.[3–5] As Be is formally a closed-shell atom, the bond order for the dimer is zero. However, the molecule is bound by 930 cm^{-1} and has a relatively short equilibrium bond length of 2.54 Å.[6] Numerous theoretical papers have been devoted to analyses of the Be–Be bond (recent examples include refs 3, 4, and 7). Electron correlation is critically important and the dimer is predicted to be purely repulsive at the Hartree–Fock level of theory. The He–BeO complex is another example where the binding between two closed-shell moieties is far stronger than expected.[2,8,9] The He atom is predicted to be bound by over 1500 cm^{-1}. In their theoretical exploration of He–BeO, Frenking et al.[8] noted that BeO is a remarkably effective Lewis acid.

Experimental evidence for strong interactions between BeO and rare gas atoms has been provided by cryogenic matrix isolation studies.[10]

Here we examine the substantial bond formed between the closed-shell species Be and F^-. In addition to interest in the bonding mechanism, BeF^- is also of potential use in geochemical analyses. The $^{10}Be/^{9}Be$ ratio can be used to date a variety of geochemical samples. The ratio is usually measured using accelerator mass spectrometry that begins with the BeO^- anion, but experiments with BeF^- show that it has an advantage in that fluoride sources suffer less interference from ^{10}B.[11–13]

We have used anion photoelectron velocity map imaging (aPES-VMI)[14–17] as the means to examine BeF^-. aPES-VMI is an anion photoelectron spectroscopy technique, where kinetic energies and angular distributions of photodetached electrons are measured to determine the energetics of the process

$$A^- \xrightarrow{h\nu} A + e- \qquad \text{Equation 5.1}$$

Consequently, the properties of neutral BeF are of importance for the assignment and interpretation of the data. Previously, BeF has been characterized by means of mass spectrometry[18,19] and high-resolution electronic spectroscopy.[20,21] The spectroscopic data show the ground state of BeF to be of $X^2\Sigma^+$ symmetry, as expected from a simple ionic bonding model (formally, $Be^+(2s^1)F^-(2s^22p^6)$). Accurate vibrational and rotational constants have been determined for the ground state.[20] The bond energy from mass spectrometry measurements is somewhat uncertain, with reported values of 50500[18] and 47200 cm^{-1}.[19] There have been several papers that present electronic structure calculations for BeF,[22–26] but there appears to be just one study that provides predictions for the BeF^- anion. Chen et al.[24] used the CCSD method with

basis sets of 6-311++G(3df,3pd) quality for both Be and F^-. They reported rotational–vibrational constants and a bond dissociation energy of $D_e^- = 28626\ cm^{-1}$.

5.2 Experimental and Theoretical Methods

The aPES-VMI apparatus used in the present work has been described previously.[15,16] BeF^- anions were produced by pulsed laser vaporization of Be metal into a flow of He that was seeded with 0.1% SF_6. The second harmonic from a Nd:YAG laser (532 nm, approximately 5 mJ/pulse) was used for the ablation source. The flux of BeF^- anions produced by the ablation process was sufficient for our measurements, obviating the need for an additional source of electrons. After mass selection of BeF^-, the anions were subjected to photodetachment using the pulses from a Nd:YAG laser (1064 nm) or a tunable dye laser operating at 862.14 nm. The lasers were vertically polarized for these measurements. Energy calibration of the imaging system was achieved by recording images for electrons from S^-, photodetached at energies near 17800 cm^{-1}. All images were processed using the MEVELER program[27] and then reconstructed using the Mathematica computing package.[37] Note that beryllium is a highly toxic material that should be handled with appropriate containment.

Electronic structure calculations were carried out using the CCSD(T) method (RCCSD(T) for BeF) and the AWCV5Z basis sets for both Be[34] and F.[35] A second set of augmented basis functions was incorporated in order to better describe the diffuse nature of the BeF^- frontier orbitals. The exponents of the added basis functions were determined using an

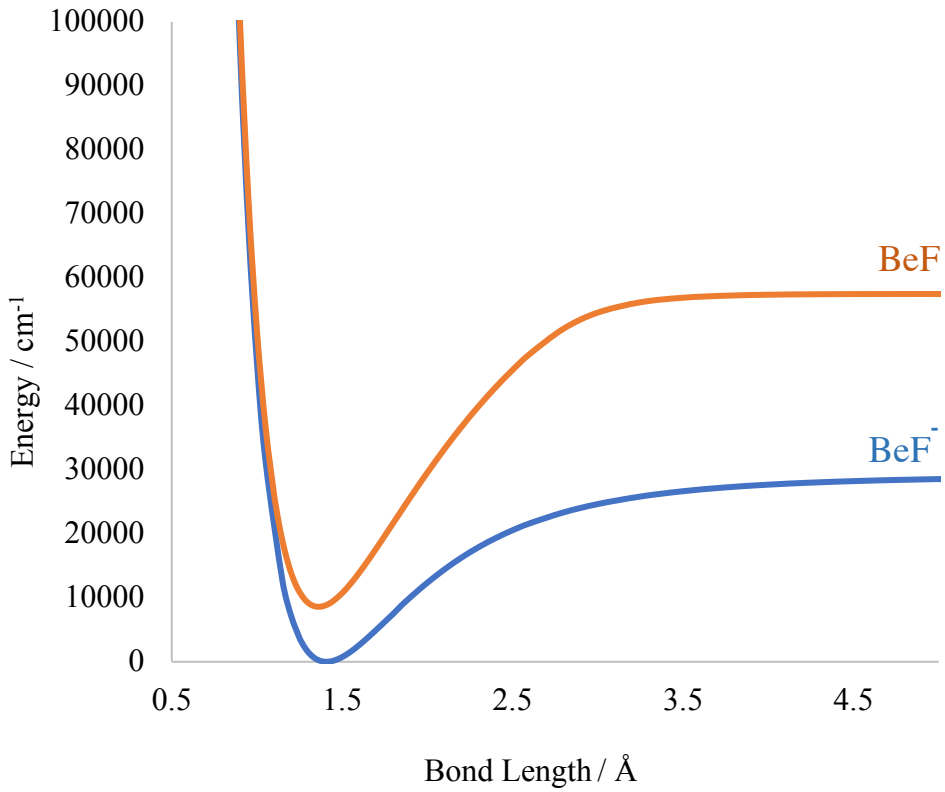

Figure 5.1. PECs of BeF and BeF^-.

even-tempered expansion of the two lowest exponent functions of the AWCV5Z basis sets. These calculations were performed using MOLPRO 2010.1.[36] Potential energy curves were constructed by calculating a series of single-point energies in the region of the equilibrium bond length (R = 1.2–1.6 Å for BeF, R = 1.3–1.7 Å for BeF^-, 0.02 Å step size), and can be viewed in Figure 5.1. Bond dissociation energies were obtained by continuing the single-point energy calculations out to 10 Å with a step size of 0.1 Å. The bound rovibrational levels of the PECs were calculated using the LEVEL 8.0 program.[38]

5.3 Results and Discussion

Figure 5.2 shows a velocity map image for the photodetachment of electrons from BeF^- using 1064 nm photons. The anisotropy of this image is consistent with photodetachment resulting from a parallel transition moment, as expected for a $X\ ^1\Sigma^+ \rightarrow X\ ^2\Sigma^+$ promotion. The value obtained for the anisotropy parameter, 1.95 ± 0.05, was close to the theoretical value of 2 for a purely parallel transition with prompt ejection of the electron.[27]

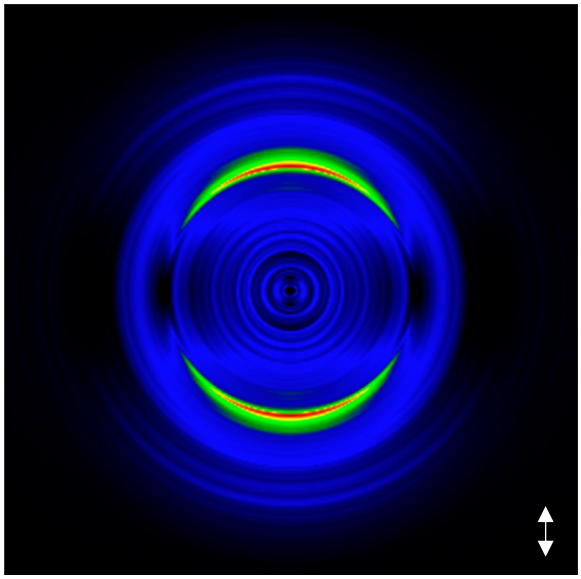

Figure 5.2. Velocity map image of the electrons resulting from photodetachment of BeF^- at 1064 nm. The photons were linearly polarized in the vertical direction.

Figure 5.3 shows kinetic energy release spectra, plotted as the photon energy ($h\nu$) minus the electron kinetic energy (eKE), for 1064 and 862.14 nm photodetachment. The assignment of these data is relatively straightforward. The most intense peak corresponds to $BeF^-(X^1\Sigma^+, \nu^- = 0) + h\nu \rightarrow BeF(X^2\Sigma^+, \nu = 0) + e^-$, defining an electron affinity (EA) of $8697 \pm 6\ cm^{-1}$. The image recorded using 862 nm detachment permitted observation of the 1–0 band at 9965 cm^{-1}, shown in Figure 5.3a. The peak at 7657 cm^{-1} in Figure 5.3b is the $\nu = 0 \leftarrow \nu^- = 1$, transition, and the features between 0–1 and 0–0 are the $\Delta\nu = -1$ sequence bands.

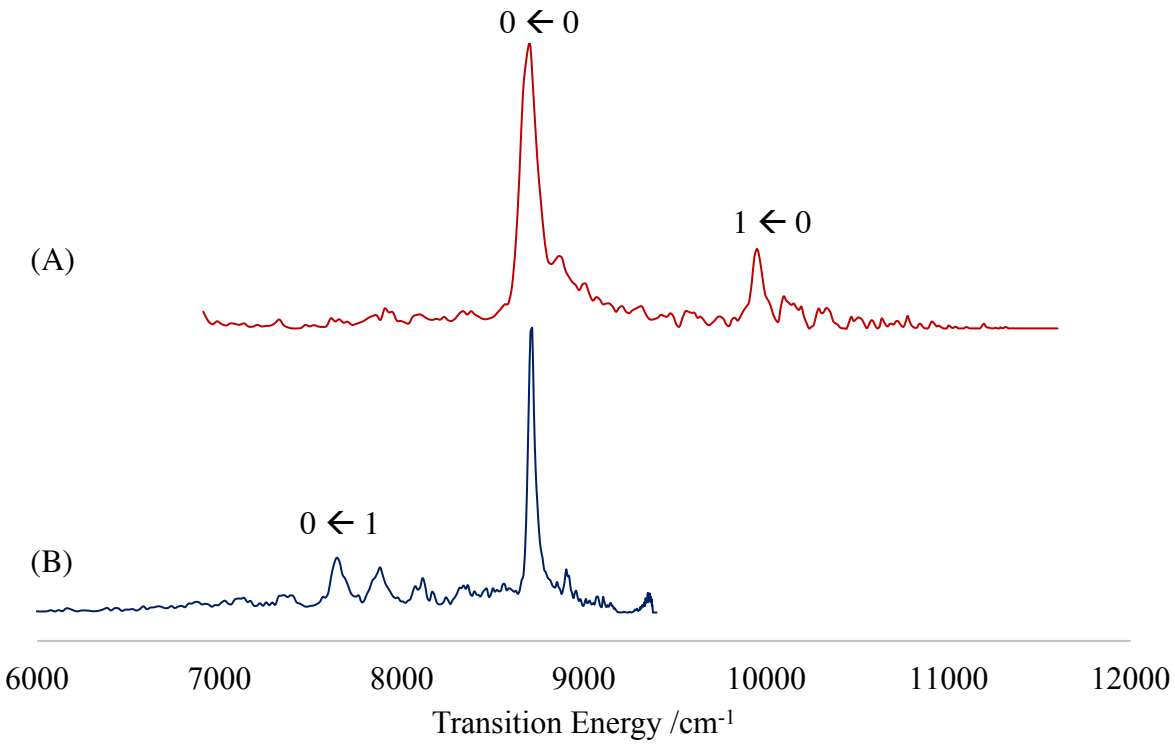

Figure 5.3. Photodetachment spectra of BeF^- at (a) 862.14 nm and (b) 1064 nm.

Refined spectroscopic constants were determined through fitting of the rotational contours, using the diatomic ro-vibrational model used to fit the BeO^- and BeS^- spectra, described in Chapters 3 and 4. Spectroscopic fits of the $\Delta v = 0$ and $\Delta v = -1$ bands are shown in Figure 5.4. The fit of the $\Delta v = 0$ indicates significant contribution from $\Delta N = 0$ (Q-type) rotational transitions. A decrease in photodetachment energy did not immediately reveal a shift to greater contributions of the $\Delta N > 0$ detachment channels as was evident with BeO^- and BeS^-. However, we were limited by our wavelength range, as lower photodetachment energies, closer to the threshold of detachment, could not be accessed. Therefore, it can not be ruled out that this behavior could exist for BeF^-. The fitting of the $\Delta v = -1$ bands provided confirmation of the specific vibrational transitions, but the spectrum was not well enough resolved in this detachment range for adequate rotational

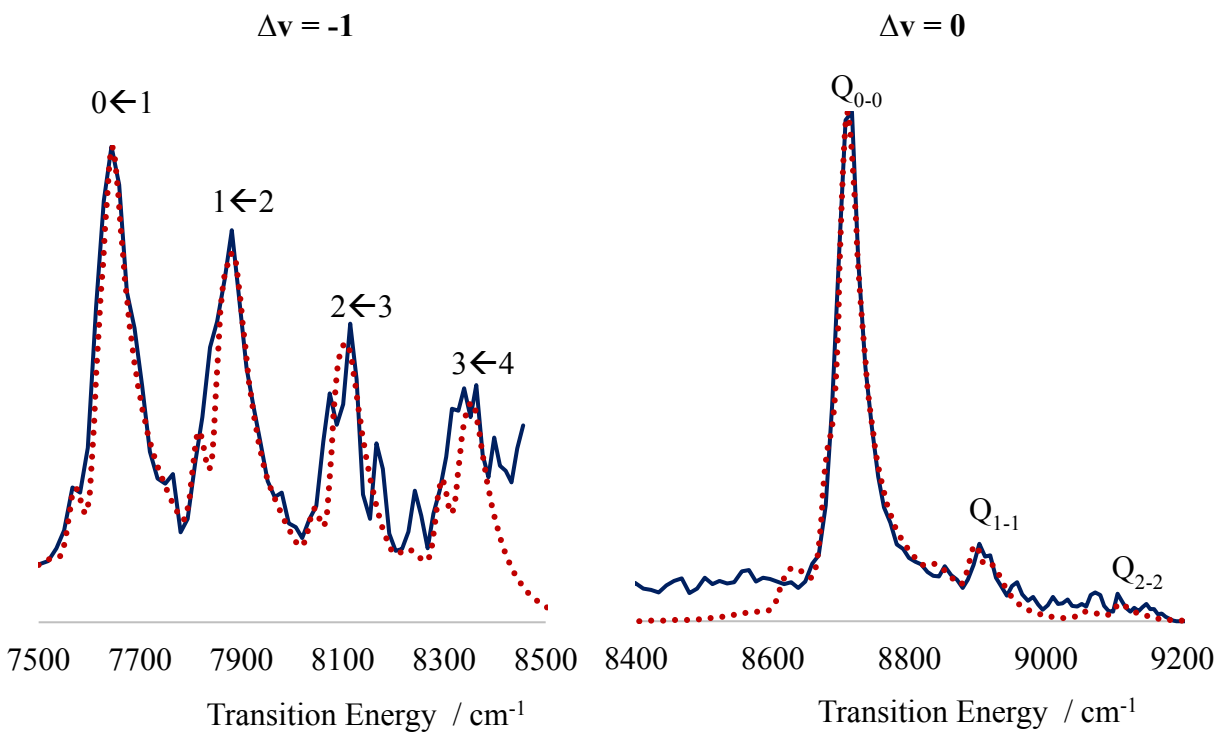

Figure 5.4 Spectral simulation (red dotted line) of the $\Delta v = 0$ and $\Delta v = -1$ bands of trace b (solid dark blue) in Figure 5.2.

assignment. Further resolution could not be achieved, also, due to limitations of laser wavelength range.

The vibrational constants obtained from these data are listed in Table 5.1. The EA for BeF and the established EA for F (27432 cm^{-1})[28] were used to determine the energy difference between the neutral molecule and the anion bond dissociation energies from the relationship $D_0 - D_e^- = EA(F) - EA(BeF) = 18735 \pm 6\ cm^{-1}$. Combined with the previous estimates for D_0,[18,19] this result defines a lower bound for the binding energy of BeF^- of $D_0^- \geq 28460\ cm^{-1}$. Results from the calculations of Chen et al.[24] are listed for comparison with the experimental data in Table 5.1,

Table 5.1. Measured and Calculated Spectroscopic Molecular Constants for BeF and BeF^-. [a]

	BeF^- ($X^1\Sigma^+$)	BeF ($X^2\Sigma^+$)	Method
EA	--	8697 ± 6	aPES-VMI
	--	8692	CCSD(T)/aug-cc-pwCV5Z
	--	8189	CCSD/6-311++ G (3df, 3pd) [24]
ω_e	1059 ± 6	*c*	aPES-VMI
	1073.2	1284.9	CCSD(T)/aug-cc-pwCV5Z
	--	1265.54	ES [20 b]
	1060.8	1258.6	CCSD/6-311++ G (3df, 3pd)
$\omega_e\chi_e$	9.5 ± 1.8	*c*	aPES-VMI
	11.5	11.3	CCSD(T)/aug-cc-pwCV5Z
	--	9.422	ES [20]
	13.4	7.8	CCSD/6-311++ G (3df, 3pd) [24]
$\Delta G_{1/2}$	1040± 7	*c*	aPES-VMI
	1050.2	1262.2	CCSD(T)/aug-cc-pwCV5Z
	--	1246.7	ES [20]
	1021	1232	CCSD/6-311++ G (3df, 3pd) [24]
D_e	28663	47480	CCSD(T)/aug-cc-pwCV5Z
	28626	45443	CCSD/6-311++ G (3df, 3pd) [24]
R_e	1.414	1.368	CCSD(T)/aug-cc-pwCV5Z
	--	1.361	ES [20]
	1.413	1.366	CCSD/6-311++ G (3df, 3pd) [20]

[a] Energies are given in wavenumbers (cm^{-1}), and bond lengths (R_e) are given in Angstroms (Å)

[b] Emission spectroscopy. [20]

[c] Held at the value determined by emission spectroscopy. [20]

and the overall level of agreement is respectable. We have performed additional electronic structure calculations to see if higher-level methods would further improve agreement with the observations and to probe the nature of the bond in BeF^-. The vibration–rotation constants from our calculations were not improved over those obtained by Chen et al.[24] The primary difference was that the current prediction of the EA is closer to the measured value (note that the calculated values in Table 5.1 include the vibrational zero-point energies).

The bond dissociation energies for BeF^- calculated here and by Chen et al.[24] are in mutual agreement and consistent with the lower bound obtained from the EA and mass spectrometry data. To probe the importance of correlation in the bonding of BeF^-, we examined the potential energy curve obtained from a Hartree–Fock calculation with the AWCV5Z basis set. This calculation yielded $D_e^- = 30814\ cm^{-1}$, which was slightly higher than the values obtained from the coupled-cluster calculations. Hence, it appears that electron correlation does not contribute significantly to the bonding.

Further insights were obtained from a natural bond orbital (NBO) analysis.[29] For this calculation, we used the Gaussian 09 [30] suite of programs at the CCSD(T) level with standard aug-cc-AVTZ basis sets. Molecular orbitals were generated at the equilibrium bond length. The population analysis indicates that the natural charges on Be and F are –0.136 and –0.864, respectively. As expected, the extra electron mostly resides on Be in a $2s/2p_z$ hybrid orbital (the natural charge of Be in the neutral molecule is predicted to be +0.805). None of the NBO linear combinations reached the threshold for identification as being bonding. However, a second-order perturbation theory analysis of the Fock matrix provided the key insight. The primary bonding interaction arises from the donation of electron density from a F^- $2s/2p_z$ hybrid orbital into a Be $2s/2p_z$ orbital that is 87% $2p_z$. A smaller but significant contribution is provided by donation from the F $2p_x$ and $2p_y$ orbitals to Be $2p_x$ and $2p_y$. Hence, BeF^- is primarily stabilized by dative bonding. By contrast, the isoelectronic closed-shell pairs BeNe and B^+Ne exhibit only weak van der Waals attractions.[31,32]

We have previously examined the anions BeO^-[15] and BeS^-,[16] and it is of interest to make comparisons with BeF^-. BeO and BeS are quite ionic, such that the structures are between the Be^+X^- and $Be^{2+}X^{2-}$ limits. The extra electron of the anion is accommodated in a Be $2s/2p_z$ orbital

that is polarized away from the negatively charged ligand. The repulsion slightly destabilizes the bond, but the EAs are relatively high, with values of 17534 and 18830 cm^{-1} for BeO and BeS, respectively. For BeF, the $2s/2p_z$ orbital that accommodates the extra electron is already partially occupied, resulting in an EA that is less than half of the values observed for BeO/BeS.

Another difference between BeF^- and BeO^-/BeS^- concerns the stability of dipole-bound excited states, which occur when the dipole moment of the neutral molecule is large enough to bind an electron via the charge–dipole interaction. It has been estimated that the minimum value for the dipole moment needed to sustain a dipole-bound state is 2 D.[33] These states were observed for BeO^-[15] and BeS^-,[16] where the neutral molecules have permanent dipole moments of 6.26 and 5 D. The present calculations for BeF yielded a dipole moment of 1.2 D, and consistent with this subthreshold value, we did not find evidence for the existence of a dipole-bound state in the photodetachment spectra.

5.4 Conclusions

In summary, the BeF^- anion is found to exhibit a substantial bond between two nominally closed-shell atoms. Electronic structure calculations show that a dative interaction resulting from the donation of F 2p electrons into a Be 2s/2p hybrid orbital is the primary source of attraction. The strength of this bond is a manifestation of the high Lewis acidity of beryllium, which is one of the characteristics that differentiates Be from the other group IIA elements.

5.5 Chapter 5 References

(1) Iversen, K. J.; Couchman, S. A.; Wilson, D. J. D.; Dutton, J. L. Modern organometallic and coordination chemistry of beryllium. *Coord. Chem. Rev.* **2015**, *297–298*, 40–48.

(2) Heaven, M. C.; Bondybey, V. E.; Merritt, J. M.; Kaledin, A. L. The unique bonding characteristics of beryllium and the Group IIA metals. *Chem. Phys. Lett.* **2011**, *506*, 1–14.

(3) Kalemos, A. The nature of the chemical bond in Be^+, Be , Be^-, and Be_3. *J. Chem. Phys.* **2016**, *145*, 214302.

(4) Magoulas, I.; Bauman, N. P.; Shen, J.; Piecuch, P. Application of the CC(P;Q) Hierarchy of Coupled-Cluster Methods to the Beryllium Dimer. J. *Phys. Chem. A* **2018**, *122*, 1350–1368.

(5) Heaven, M. C.; Merritt, J. M.; Bondybey, V. E. Bonding in beryllium clusters. *Annu. Rev. Phys. Chem.* **2011**, *62*, 375–393.

(6) Merritt, J. M.; Bondybey, V. E.; Heaven, M. C. Beryllium Dimer- Caught in the Act of Bonding. *Science* (Washington, DC, U. S.) **2009**, *324*, 1548–1551.

(7) Koch, D.; Fertitta, E.; Paulus, B. Calculation of the static and dynamical correlation energy of pseudo-one-dimensional beryllium systems via a many-body expansion. *J. Chem. Phys.* **2016**, *145*, 024104.

(8) Frenking, G.; Koch, W.; Gauss, J.; Cremer, D. Stabilities and nature of the attractive interactions in HeBeO, NeBeO, and ArBeO and a comparison with analogs NGLiF, NGBN, and NGLiH (NG = He, Ar). A theoretical investigation. *J. Am. Chem. Soc.* **1988**, *110*, 8007–8016.

(9) Takayanagi, T.; Motegi, H.; Taketsugu, Y.; Taketsugu, T. Accurate ab initio electronic structure calculations of the stable helium complex: HeBeO. *Chem. Phys. Lett.* **2008**, *454*, 1–6.

(10) Thompson, C. A.; Andrews, L. Noble Gas Complexes with BeO: Infrared Spectra of NG-BeO (NG = Ar, Kr, Xe). *J. Am. Chem. Soc.* **1994**, *116*, 423–424.

(11) Wacker, L.; Grajcar, M.; Ivy-Ochs, S.; Kubik, P. W.; Suter, M. ^{10}Be analyses with a compact AMS facility - are BeF_2 samples the solution? *Radiocarbon* **2004**, *46*, 83–88.

(12) Zhao, X. L.; Soto, C.; Kieser, W. E.; Litherland, A. E.; Tracy, B. L.; Ungar, K.; Stocki, T. Measurement of ^{10}Be in air filters using BeF^- ions from $BaBeF_4$. *Nucl. Instrum. Methods Phys. Res., Sect. B* **2007**, *259*, 345–350.

(13) Ruiz-Gomez, A.; Chamizo-Calvo, E.; Lopez-Gutierrez, J. M.; Garcia-Leon, M.; Mueller, A. M.; Christl, M. On the measurement of **^{10}**Be on the 1MV compact AMS system at the Centro Nacional de Aceleradores (Spain). *Nucl. Instrum. Methods Phys. Res., Sect. B* **2010**, *268*, 733–735.

(14) Hock, C.; Kim, J. B.; Weichman, M. L.; Yacovitch, T. I.; Neumark, D. M. Slow photoelectron velocity-map imaging spectros- copy of cold negative ions. *J. Chem. Phys.* **2012**, *137*, 244201–244201.

(15) Mascaritolo, K. J.; Dermer, A. R.; Green, M. L.; Gardner, A. M.; Heaven, M. C. Photodetachment spectroscopy of the beryllium oxide anion, BeO. *J. Chem. Phys.* **2017**, *146*, 054301–054301.

(16) Dermer, A. R.; Green, M. L.; Mascaritolo, K. J.; Heaven, M. C. Photoelectron Velocity Map Imaging Spectroscopy of the Beryllium Sulfide Anion, BeS. *J. Phys. Chem. A* **2017**, *121*, 5645–5650.

(17) Leon, I.; Yang, Z.; Liu, H.-T.; Wang, L.-S. The design and construction of a high-resolution velocity-map imaging apparatus for photoelectron spectroscopy studies of size-selected clusters. *Rev. Sci. Instrum.* **2014**, *85*, 083106–083106.

(18) Farber, M.; Srivastava, R. D. Dissociation energies of beryllium fluoride (BeF) and beryllium chloride (BeCl) and heat of formation of beryllium chlorofluoride (BeClF). *J. Chem. Soc., Faraday Trans. 1* **1974**, *70*, 1581–1589.

(19) Hildenbrand, D. L.; Murad, E. Mass-spectrometric determination of the dissociation energy of beryllium monofluoride. *J. Chem. Phys.* **1966,** *44*, 1524–1529.

(20) Tai, G.; Verma, R. D. The UV spectrum of BeF. *J. Mol. Spectrosc.* **1995**, *173*, 1–7.

(21) Walker, T. E. H.; Barrow, R. F. A $^2\Pi$-X $^2\Sigma^+$ system of beryllium monofluoride. *J. Phys. B: At. Mol. Phys.* **1969**, *2*, 102–106.

(22) Machado, F. B. C.; Ornellas, F. R. A theoretical study of the beryllium fluoride (BeF) molecule in the X $^2\Sigma^+$ state. *Mol. Phys.* **1989**, *67*, 1129–1140.

(23) Ornellas, F. R.; Machado, F. B. C.; Roberto-Neto, O. A theoretical study of beryllium fluoride and fluoroberyllium(1+) (BeF and BeF^+) in their lowest-lying electronic states. *Mol. Phys.* **1992**, *77*, 1169–1185.

(24) Chen, H.-j.; Wang, Q.-w.; Yang, T.-y.; Yang, Y.-h. Investigation of analytic potential energy function and molecular spectroscopic constants of BeF^x(x = 0,±1). *Chongqing Keji Xueyuan Xuebao, Ziran Kexueban* **2010**, *12*, 194–196.

(25) Lane, I. C. Ultracold fluorine production via Doppler cooled BeF. *Phys. Chem. Chem. Phys.* **2012**, *14,* 15078–15087.

(26) Yu, H.; Truhlar, D. G. Components of the Bond Energy in Polar Diatomic Molecules, Radicals, and Ions Formed by Group-1 and Group-2 Metal Atoms. *J. Chem. Theory Comput.* **2015**, *11*, 2968–2983.

(27) Dick, B. Inverting ion images without Abel inversion: maximum entropy reconstruction of velocity maps. *Phys. Chem. Chem. Phys.* **2014**, *16*, 570–580.

(28) Blondel, C.; Delsart, C.; Goldfarb, F. Electron spectrometry at the μeV level and the electron affinities of Si and F. *J. Phys. B: At., Mol. Opt. Phys.* **2001**, *34*, L281–L288.

(29) Weinhold, F.; Landis, C. R.; Glendening, E. D. What is NBO analysis and how is it useful? *Int. Rev. Phys. Chem.* **2016**, *35*, 399–440.

(30) Frish, M. J. et al. Gaussian 09, revision 1A; Gaussian Inc.: Wallingford, CT, **2009**.

(31) Harris, J. P.; Gardner, A. M.; Wright, T. G.; Breckenridge, W. H.; Viehland, L. A. Interactions in the B^+-RG Complexes and Comparison with Be^+-RG (RG = He-Rn): Evidence for Chemical Bonding. *J. Phys. Chem. A* **2012**, *116*, 4995–5007.

(32) Wong, M. W.; Nobes, R. H.; Bouma, W. J.; Radom, L. Isoelectronic analogs of molecular nitrogen: tightly bound multiply charged species. *J. Chem. Phys.* **1989**, *91*, 2971–2979.

(33) Jordan, K. D.; Wang, F. Theory of dipole-bound anions. *Annu. Rev. Phys. Chem.* **2003**, *54*, 367–396.

(34) Prascher, B. P.; Woon, D. E.; Peterson, K. A.; Dunning, T. H., Jr.; Wilson, A. K. Gaussian basis sets for use in correlated molecular calculations. VII. Valence, core-valence, and scalar relativistic basis sets for Li, Be, Na, and Mg. *Theor. Chem. Acc.* **2011**, *128*, 69–82.

(35) Peterson, K. A.; Dunning, T. H., Jr. Accurate correlation consistent basis sets for molecular core-valence correlation effects: The second row atoms Al-Ar, and the first row atoms B-Ne revisited. *J. Chem. Phys.* **2002**, *117*, 10548–10560.

(36) Werner, H.-J.; Knowles, P. J.; Lindh, R.; Manby, F. R.; Schütz, M.; et al. MOLPRO, version 2010.1, a package of ab initio programs; **2010**.

(37) Mathematica, version 11.3; Wolfram Research, Inc.: Champaign, IL, **2018**.

(38) LeRoy, R. J. LEVEL 8.0, A Computer Program for Solving the Radial Schrödinger Equation for Bound and Quasibound Levels; Chemical Physics Research Report CP-663; University of Waterloo, **2007**.

Chapter 6

Characterization of the Ground States of BeC_2 and BeC_2^- via Photoelectron Velocity Map Imaging Spectroscopy

The contents and figures of this chapter are reprinted or adapted with permission from

Green, M. L., Jaffe, N. B., & Heaven, M. C. Characterization of the Ground States of BeC2 and BeC2–via Photoelectron Velocity Map Imaging Spectroscopy. *The Journal of Physical Chemistry Letters*, **2019**, *11*(1), 88-92.

Due to their potentially unique properties, beryllium carbide materials have been the subject of many theoretical studies. However, experimental validation has been lacking due to the difficulties of working with Be. Neutral beryllium dicarbide has been predicted to have a T-shaped equilibrium structure (C_{2v}), while previous quantum chemistry calculations for the structure of the anion had not yielded consistent results. In this study, we report photoelectron velocity map imaging spectra for the BeC_2^- X $^2A_1 \rightarrow BeC_2$ X $^1A_1$ transition. These data provide vibrational frequencies and the electron affinity of BeC_2. *Ab initio* electronic structure calculations, validated against the experimental data, show that both the anion and the neutral form have C_{2v} equilibrium geometries with polar covalent bonding between Be and the C_2 subunit. Computed vibrational frequencies and the electron affinity, obtained at the CCSD(T) level of theory, were found to be in good agreement with the measurements.

6.1 Introduction

Metallized carbides exhibit a range of useful properties, not manifested by pure carbon materials, due to the unique characteristics of the doped metals. Beryllium is a very distinctive element known to exhibit more covalent bonding, as compared to other Group IIA metals.[1–7] Beryllium carbides are of interest as graphene alternatives[8] and metallo-carbohydrenes.[9] Beryllium carbide clusters have been identified as promising materials for hydrogen storage in nanomaterials.[9] Also, there is interest in beryllium-doped carbon clusters as they have been found to be beneficial for the creation of thin films for use in nuclear and plasma sciences.[10] Under high pressures, BeC_2 has been shown to behave more as an insulator than an electrical conductor, counter to the behavior of the other alkaline earth metal dicarbides.[11] Given this

background, interest in this molecule can lead to a better understanding of bonding within the larger class of clusters and bulk materials.

Many dicarbide species have been investigated to explore the factors influencing bonding and equilibrium geometries. SiC_2 [12] and GeC_2[13,14] have been found to exhibit bent (T-shaped) structures with predominantly $M^+–(C_2^-)$ ionic bonding (where Si and Ge are considered to be metalloids). This is a marked difference from the geometry of the non-metal–non-metal bonding of C_2P and C_2As, where the heteroatom bonds to the C_2 moiety in an end-on scheme, producing a covalent linear $C_{\infty v}$ molecule.[15] Many metallic dicarbides have been predicted to exhibit T-shaped structures with ionic character, including the heavier alkaline earth metals.[16,17] However, due to beryllium's tendency toward covalent bonding, there is the possibility that BeC_2 might not show the same degree of metallic bonding character as the other Group IIA metals.

Motivated by the quest to find the smallest cyclic molecule that could stabilize a C-C triple bond, Frenking[6] carried out a careful theoretical analysis of the bonding in BeC_2. He found that the singlet T-shaped geometry was the minimum-energy configuration, with a C–C bond order close to 3. However, BeC_2 was not the example of a cyclic π-bonded system for which they had hoped. Instead, Frenking[6] concluded that the $Be–C_2$ bond was markedly ionic. He also noted that T-shaped BeC_2 would be stable in the gas phase. Subsequent theoretical studies have been consistent with these conclusions.[18–23] By contrast, there is very little information concerning the structure of the anion. Chen et al.[20] used hybrid B3LYP density functional theory to examine beryllium-doped linear carbon chains. Geometry optimizations were carried out using the Pople 6-31G* basis sets. They reported the ground state of BeC_2^- to be a linear structure, similar to that of the nonmetallic C_2P and C_2As.[15] Ghouri et al.[19] used the B3PW91 method with 6-31G* basis functions to investigate neutral Be_nC_m clusters, and they also reported vertical electron

affinities (EAs) for the equilibrium geometries. For T-shaped BeC_2, they obtained a value near 2 eV, but they did not explore the minimum-energy structure for the anion. The density functional theory (DFT) calculations of Patrick et al.[22] (B3PW91 with large Pople-style basis sets of triple-ζ quality) predicted that linear geometry for the anion was not stable, and they obtained an adiabatic EA of 1.99 eV for T-shaped BeC_2. In this study, we have used anion photodetachment spectroscopy and *ab initio* electronic structure calculations to examine the bonding and equilibrium geometries of both the neutral form and the anion. High-level electronic structure calculations were carried out to facilitate interpretation of the spectroscopic data and further analyses of the bonding.

6.2 Experimental Methods

Photoelectron spectra of the BeC_2^- $X\ ^2A_1 \rightarrow BeC_2$ $X\ ^1A_1$ transition were obtained using a velocity map imaging spectrometer, described previously.[24–27] Anions were generated through pulsed laser ablation of a beryllium rod into a flow of helium buffer gas, using the fundamental output of a Nd:YAG Minilite laser (1064 nm). The buffer gas was seeded with 1% acetylene to provide a source of carbon. Anions from the ablation plume were mass selected and subjected to photodetachment by a frequency-doubled Nd:YAG laser (532 nm) or an excimer-pumped tunable dye laser operating in the wavelength range of 532–643 nm. For all measurements, the lasers were vertically polarized.

Accumulated photoelectron images were processed using MEVELER.[28] Energy calibrations were conducted using the known electron detachment transitions of S^-, for photodetachment wavelengths ranging from 532 to 580 nm.

6.3 Experimental Results and Discussion

Figure 6.1 shows four photoelectron spectra taken at varying photon energies, as well as their corresponding processed velocity map images. Spectrum A, taken at the highest photon energy (18363 cm^{-1}) of all shown spectra, reveals all 10 major spectral features seen for the photodetachment of BeC_2^- → BeC_2. Subsequent spectra were taken at lower photon energies to

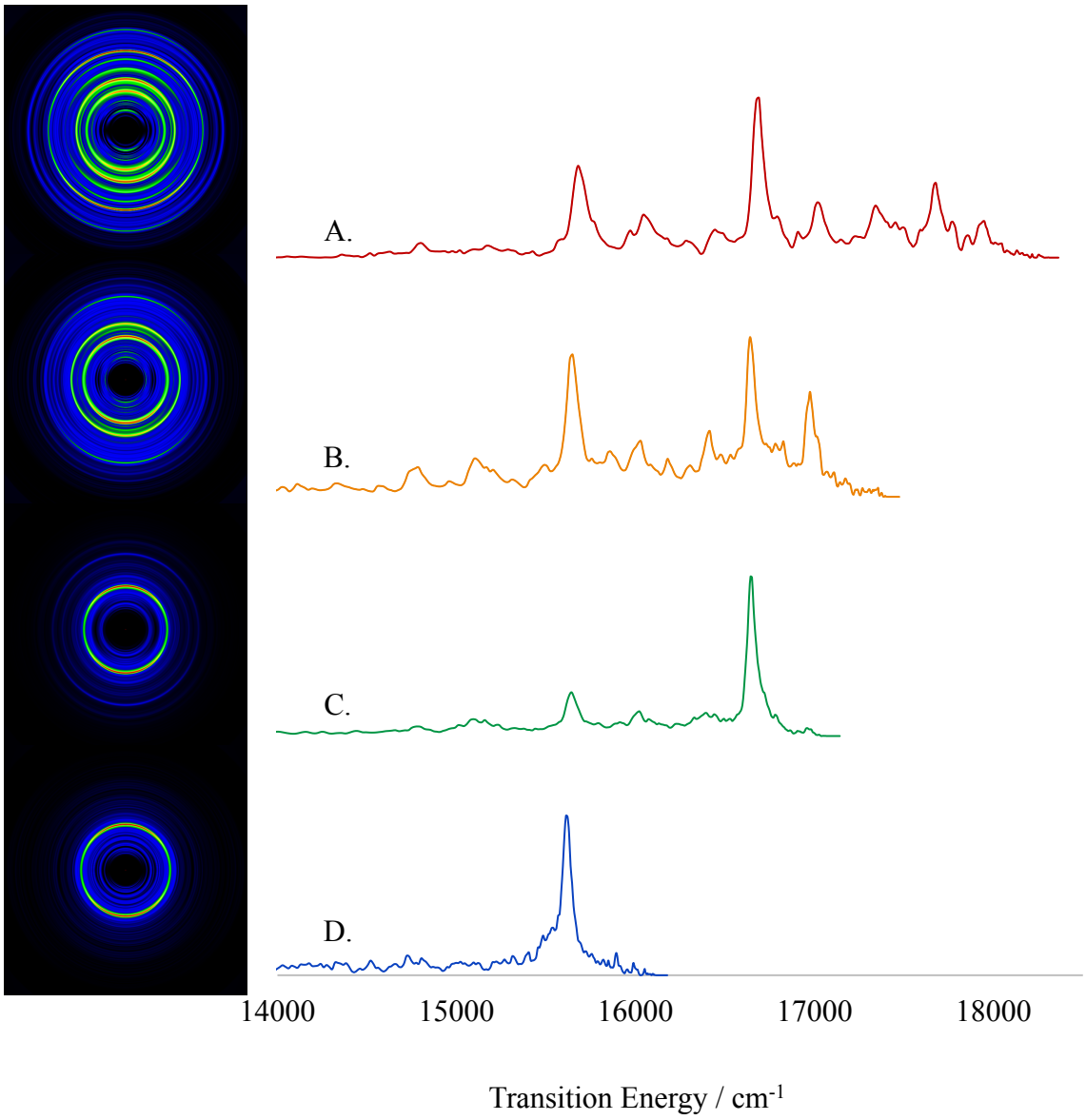

Figure 6.1. Photodetachment spectra and corresponding velocity map images for BeC_2^- recorded using photon energies (A) 18363 cm^{-1}, (B) 17473 cm^{-1}, (C) 17141 cm^{-1}, and (D) 16177 cm^{-1}.

further resolve the lower transition energy features. All lower photon energy spectra produced increased resolution for the features closest to the threshold of detachment. Spectrum C resulted in a noticeable decrease in intensity for the lower energy peaks, in comparison to the highest energy peak of the spectrum. This phenomenon was not further investigated.

By examining the velocity map images, it appears that some transitions exhibited some anisotropic character. In order to further understand this character, the β- parameter for each transition was evaluated as a function of the eKE for each different photon energy spectrum. Unfortunately, no trend in the β- parameter could be identified for any transition. As, no two spectra taken for this study had the same photon energy, further investigations into the reproducibility of anisotropy for differing eKE's, and differing image signal, might be necessary to make future conclusions about images with convoluted anisotropy.

Figure 6.2 shows the assignment of the photoelectron spectrum recorded using 18363 cm^{-1} (Figure 6.1, spectrum A) detachment photons. Assignment of this spectrum was guided by

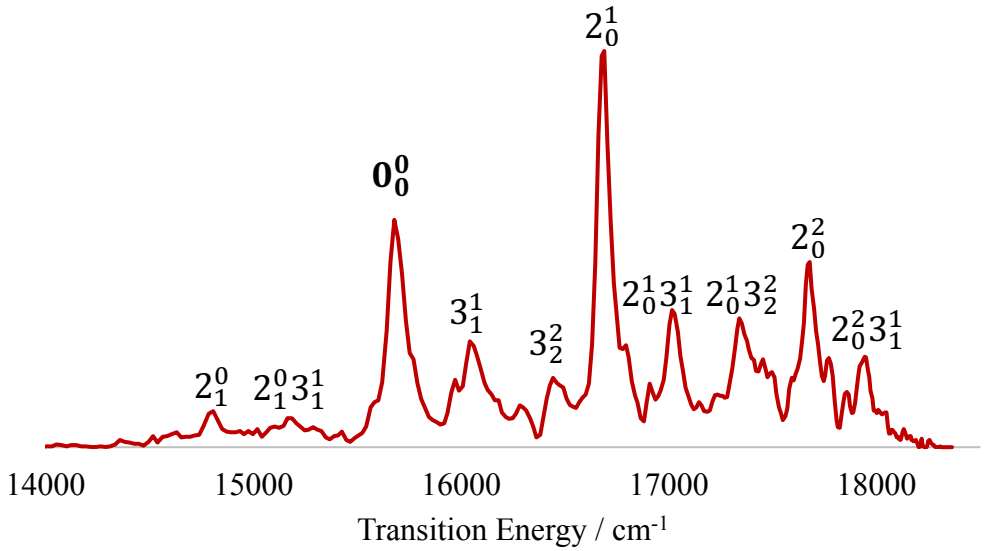

Figure 6.2. Assigned photoelectron spectrum for the $BeC_2^- \rightarrow BeC_2$ transition, taken at a photodetachment energy of 18363 cm^{-1}.

the results from electronic structure calculations that are described below. The numbering of the vibrational modes corresponds to the CC stretch (v_1), the Be–C_2 stretch (v_2), and the bending mode (v_3).

Table 6.1.Peak positions, offsets from origin (bold) and vibronic assignments for the $BeC_2^- \rightarrow BeC_2$ spectra.

Transition Energy (cm^{-1})	Offset (cm^{-1})	Assignment
14788	-861	2_1^0
15099	-550	$2_1^0 3_1^1$
15649	**0**	$\mathbf{0_0^0}$
16031	382	3_1^1
16416	767	3_2^2
16640	991	2_0^1
16975	1326	$2_0^1 3_1^1$
17357	1708	$2_0^1 3_2^2$
17653	2004	2_0^2
17942	2293	$2_0^2 3_1^1$

Table 6.1 lists the assigned vibronic transitions. The energy for each assigned transition was obtained from an image recorded with the detachment photon energy set just above the specific transition threshold to achieve the best resolution. The peak located at 15649 cm^{-1} was identified as the origin band, given its intensity and proximity to the predicted value of the

electron affinity for T-shaped neutral BeC_2 (see Table 6.2). The other strong bands, located at relative energies of 991 and 2004 cm^{-1} from the origin, are assigned to the Be–C_2 stretch fundamental (v_2) and first overtone ($2v_2$) of the neutral. The two peaks directly above the origin are the first and second $\Delta v = 0$ bending sequence bands. Note that the v_3 vibrational mode transforms as the B2 irreducible representation in C_{2v} symmetry, so detachment events that involve odd changes in the v_3 quantum number are symmetry forbidden.

The peaks located at 16975, 17357, and 17942 cm^{-1} are assigned to bend–stretch combination modes. The transitions at energies below the origin are the stretch hot band $v^- = 1$ and the bend–stretch combination hot band, respectively. The C–C stretch was not active in this spectrum, indicative of a very small difference in the C–C bond length between the neutral form and the anion. The experimentally and computationally determined electron affinities and vibrational constants are listed in Table 6.2.

Table 6.2. Comparison of the experimentally determined and calculated vibrational constants for BeC_2.

		Experimental	CCSD(T)/avtz
BeC_2	EA	15656 ± 34	15618
	v_1	not active	1739
	v_2	1011 ± 26	1054.1
	$^1A_1$ (v_3) – $^2A_1$ (v_3)	318 ± 38	398

6.4 Theoretical Analysis of BeC_2^- and BeC_2

Electronic structure calculations were carried out for the linear and bent geometries of the doublet states of the BeC_2^- anion and the singlet states of the BeC_2 neutral form, using RCCSD(T)/ CCSD(T) methods with aug-cc-pVQZ basis sets.[29] The Molpro 2010.1

computational package[30] was used for these predictions. Optimized geometries and vibrational frequencies of the anion and neutral species are listed in Table 6.3. This table also includes the electron affinity for the T-shaped and linear geometries of the neutral molecule, with zero-point

Table 6.3. Calculated relative energies, optimized geometries, and vibrational frequencies of the linear and bent confirmations of BeC_2 and BeC_2^-.

	Sym.	State	EA_{vert} (cm^{-1})	E_{rel} (cm^{-1})	r_{BeC} (Å)	r_{CC} (Å)	Bond Angle (degrees)[a]	ν_1 (cm^{-1})	ν_2 (cm^{-1})	ν_3 (cm^{-1})
BeC_2	$C_{\infty v}$	$^1\Sigma^+$	24223	10062	1.562	1.267	180	1714.7	823.6	102.9
	C_{2v}	$^1A_1$	15361	0	1.616	1.275	46.4	1739.4	1054.1	674.1
BeC_2^-	$C_{\infty v}$	$^2\Sigma^+$	--	1200	1.591	1.269	180	1910.6	931.5	151.2
	C_{2v}	$^2A_1$	--	0	1.724	1.272	43.3	1784.0	893.7	275.7

[a] The bond angle for linear $C_{\infty v}$ structures is defined as ∠ CCBe and the bond angle for bent C_{2v} structures is defined as ∠ CBeC.

energies taken into account. The C_{2v} structure was found to be the most stable isomer of the neutral form, by approximately 10000 cm^{-1}. This calculation was in good agreement with previous work.[6,16,18,19,21–23] The C_{2v} structure was found to be the most stable isomer for anion, which contradicts the findings of Chen et al.[20] The linear structure of the anion was predicted to exist only 1200 cm^{-1} above the bent geometry, for the anion.

To determine the barrier for conversion from the linear to the bent geometry, angular cuts through the potential energy hypersurface were constructed. Point-wise energies were calculated for variation of the ∠BeCC angle from 180° to 90° (linear to L-shaped, respectively). These curves are shown in Figure 6.3. For the anion, there is a barrier of approximately 640 cm^{-1},

indicating that the linear geometry could be stable at low temperatures. However, the neutral

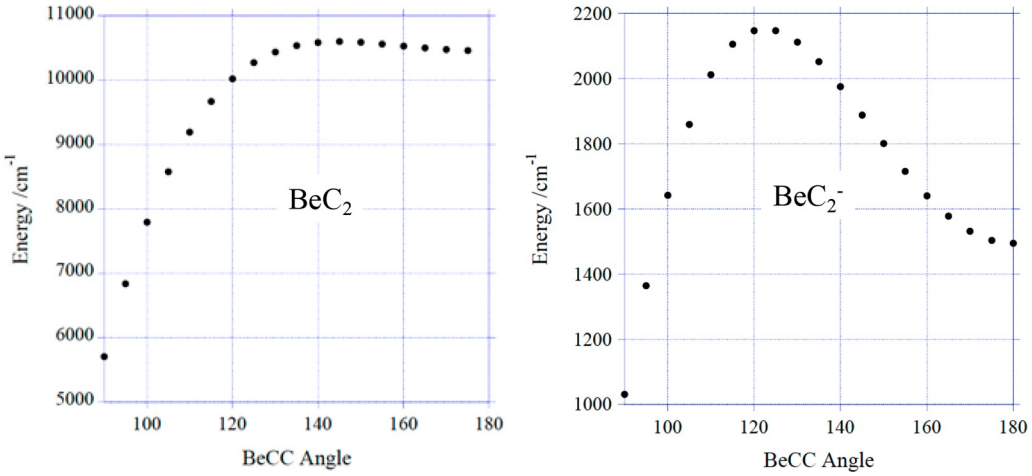

Figure 6.3. Angular cuts of the potential energy surfaces of BeC_2 and BeC_2^-. Energies are relative to the global minimum for each potential energy surface. The bond lengths were fixed at r_{CC} = 1.27 Å and r_{BeC} = 1.60 Å.

BeC_2 curve reveals a much smaller barrier supporting the linear geometry, suggesting that the linear neutral molecule is not stable. The work of Patrick et al.[22] gave similar relative energies for the neutral form but indicated that the linear state was slightly lower in energy, relative to the T-shaped minimum. Dissociation energies for the $BeC_2 \rightarrow Be + C_2$ and $BeC_2^- \rightarrow Be + C_2^-$ processes (under C_{2v} symmetry) were predicted by the present coupled cluster calculations to be 40920 and 29890 cm^{-1}, respectively.

To examine the bonding characteristics of the anion and neutral form, natural bond orbital (NBO)[31] analyses were performed and localized orbital locator function (LOL)[32,33] surfaces were constructed. NBO analyses of the anion and neutral ground states were implemented using the Gaussian 09 program, using DFT with the B3LYP functional and 6-311++G Pople basis sets.[34] NBO results for the neutral molecule indicated a triple bond between the two carbon atoms and a single bond from each carbon to the beryllium atom. The Be–C bonds were primarily comprised of carbon hybrid orbitals, as the bonds were > 80% C

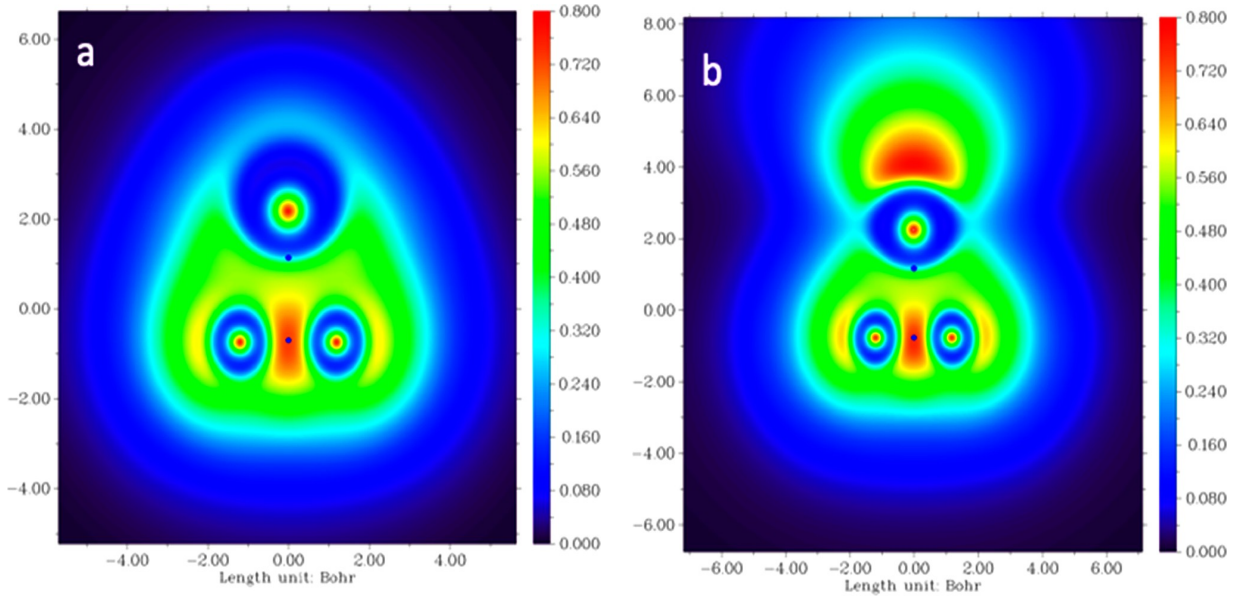

Figure 6.4 Cross section of the LOL surfaces for (a) BeC_2 and (b) BeC_2^-. The two bond critical points on the C_{2v} rotation axis are indicated.

2s/2p and < 20% Be 2s/2p character. The NBO analysis of the anion also indicated a C-C triple bond, but the level of bonding to the Be atom was decreased to the point where the effective Be–C bond order was 0.75.

A more nuanced picture of the bonding was obtained by using the Multiwfn software package[33] to analyze the wave functions. Panels a and b of Figure 6.4 show plots of the localized orbital locator function for the neutral form and the anion, respectively. The bond critical points are also shown as dots that are located on the C_2 rotation axis. For both the neutral molecule and the anion, there is an obvious build-up of electron density between the carbon atoms with the expected bond critical point between them. For the neutral molecule, the C–C bond orders obtained from the Mayer and Fuzzy Bond Order (FBO)[33,35] indices were 1.6 and 2.3, respectively. Note that the calculated vibrational frequency was consistent with a double bond. The frequency was lower than that of diatomic C_2 (ω_e = 1845.71 cm^{-1}) by just 106 cm^{-1}. The Mulliken and Hirshfeld atomic charges were –0.24 and –0.23 for C and 0.48 and 0.46 for Be,

respectively (the electron-depleted region around Be is evident in Figure 6.4a). This charge distribution and the position of the second bond critical point indicate that the bonding between Be and the C_2 moiety is of a polar covalent type, with a large contribution from the electrostatic interactions. These conclusions are in agreement with the analysis given by Frenking [6] and differ only in the rather model-dependent matter of the C–C bond order. Animation of the vibrational modes further supports the model of polar covalent bonding for the Be atom. The bending vibration involves a minimal change in the C–C bond length and is best described as a liberation of the C_2 subunit, such that Jacobi coordinates are the appropriate choice for discussion of the vibrational motions.

In our previous studies of the BeO^- and BeS^- anions, we found that the additional electron of the anion was accommodated by Be 2s/2p hybrid orbitals that were polarized away from the negatively charged O or S atom.[24,25] BeC_2 is similar to BeO/BeS in that the ionic bonding can be formally represented as $Be^{2+}X^{2-}$. In keeping with this view, we found that the additional electron of BeC_2^- resides in a back-polarized, Be-centered, in-plane 2s/2p hybrid orbital. This can be seen in Figure 6.4b, where there is increased electron density localized above the Be atom, with some additional negative charge that has been pushed onto C_2. The charge distribution has become (Mulliken and Hirshfeld) –0.12 and –0.18 on Be and –0.44 and –0.41 on each C, respectively. The partial negative charge on Be diminishes the attraction to C_2, resulting in a lengthening of the Be–C_2 Jacobi distance from 1.49 to 1.60 Å. This change is accompanied by significant decreases in the Be–C_2 stretch and bend frequencies. The transfer of charge into the LUMO of C_2 results in a slightly higher C–C stretch frequency but almost no change in the C–C bond length (cf. Table 6.3). Overall, these changes in geometry explain why the Be–C_2 stretch was active in the photodetachment spectrum while the C–C stretch was not.

Note that the bond critical points are in similar positions for both BeC_2 and BeC_2^-, indicating that the $Be–C_2^-$ bond is still polar covalent with strong electrostatic contributions. The bond orders for the anion were 1.6 (C–C) and 0.75 (Be–C) for the Mayer model and 1.2 (C–C) and 0.48 (Be–C) for the FBO model. The decrease in the C–C bond order (as compared to that of the neutral form) for the FBO was unexpected and may be an artifact of the application of this approximation to an open-shell system.

6.5 Conclusions

In conclusion, anion photodetachment measurements have provided the first experimental data for BeC_2 and the BeC_2^- anion. In accordance with previous theoretical studies, the structure of BeC_2 is found to be T-shaped, with a polar covalent bond between Be and C_2 with strong electrostatic contributions. The structure of the anion was also found to be T-shaped, resolving a previous disagreement between predictions. *Ab initio* coupled calculations, validated against the experimental data, indicted a double bond for the C_2 subunit for both the neutral molecule and the anion. The $Be–C_2$ bond of the anion was also found to be polar covalent but weakened (relative to that of the neutral form) by the additional negative charge. The calculated EA was found to be in excellent agreement with the measured value of 1.905 eV.

6.6 Chapter 6 References

(1) Green, M. L.; Jean, P.; Heaven, M. C. Dative Bonding Between Closed-Shell Atoms: The BeF^- Anion. *J. Phys. Chem. Lett.* **2018**, *9*, 1999–2002.

(2) Heaven, M. C.; Merritt, J. M.; Bondybey, V. E. Bonding in Beryllium Clusters. *Annu. Rev. Phys. Chem.* **2011**, *62*, 375–93.

(3) Heaven, M. C.; Bondybey, V. E.; Merritt, J. M.; Kaledin, A. L. The Unique Bonding Characteristics of Beryllium and the Group IIA Metals. *Chem. Phys. Lett.* **2011**, *506*, 1–14.

(4) Merritt, J. M.; Bondybey, V. E.; Heaven, M. C. Spectroscopy, Structure, and Ionization Energy of BeOBe. *J. Phys. Chem. A* **2009**, *113*, 13300–13309.

(5) Merritt, J. M.; Bondybey, V. E.; Heaven, M. C. Beryllium Dimer- Caught in the Act of Bonding. *Science* **2009**, *324*, 1548–1551.

(6) Frenking, G. Carbon-Carbon Triple-Bond Stabilization in Three- Membered Ring Compounds: Boriryne, Dilithiumcyclopropyne and Berylliryne. *Chem. Phys. Lett.* **1984**, *111*, 529–32.

(7) Frenking, G.; Koch, W.; Gauss, J.; Cremer, D. Stabilities and Nature of the Attractive Interactions in HeBeO, NeBeO, and ArBeO and a Comparison with Analogs NGLiF, NGBN, and NGLiH (NG = He, Ar). A Theoretical Investigation. *J. Am. Chem. Soc.* **1988**, *110*, 8007–16.

(8) Zaleski-Ejgierd, P.; Hakala, M.; Pyykko, P. Comparison of Chain Versus Sheet Crystal Structures for Cyanides MCN (M = Cu-Au) and Dicarbides MC_2 (M = Be-Ba; Zn-Hg). Alternatives to Graphene? *Phys. Rev. B: Condens. Matter Mater. Phys.* **2007**, *76*, 094104.

(9) Tuerker, L. Hydrogen Storage Capacity of Be@C115 System. *J. Mol. Struct.: THEOCHEM* **2005**, *723*, 105–110.

(10) Xie, Y.; Morosoff, N. C.; James, W. J. XPS Characterization of Beryllium Carbide Thin Films Formed via Plasma Deposition. *J. Nucl. Mater.* **2001**, *289*, 48–51.

(11) Du, H.; Feng, W.; Li, F.; Wang, D.; Zhou, D.; Liu, Y. Nonmetallization and Band Inversion in Beryllium Dicarbide at High Pressure. *Sci. Rep.* **2016**, *6*, 26398.

(12) Michalopoulos, D. L.; Geusic, M. E.; Langridge-Smith, P. R. R.; Smalley, R. E. Visible Spectroscopy of Jet-Cooled Silicon Dicarbide: Geometry and Electronic Structure. *J. Chem. Phys.* **1984**, *80*, 3556– 60.

(13) Koput, J. Ab Initio Potential Energy Surface and Vibration- Rotation Energy Levels of Germanium Dicarbide, GeC_2. *J. Comput. Chem.* **2018**, *39*, 1327–1334.

(14) Zingsheim, O.; Martin-Drumel, M.-A.; Thorwirth, S.; Schlemmer, S.; Gottlieb, C. A.; Gauss, J.; McCarthy, M. C. Germanium Dicarbide: Evidence for a T-Shaped Ground State Structure. *J. Phys. Chem. Lett.* **2017**, *8*, 3776–3781.

(15) Sunahori, F. X.; Wei, J.; Clouthier, D. J. Spectroscopic Identification of C_2P and C_2As, Two New Main Group Dicarbides. *J. Am. Chem. Soc.* **2007**, *129*, 9600–9601.

(16) Fuentealba, P.; Savin, A. Electronic Structure and Bonding of the Ground State of Alkaline-Earth-Metal Monoxides and Carbides. *J. Phys. Chem. A* **2000**, *104*, 10882–10886.

(17) Boldyrev, A. I.; Simons, J. Structures of Small Magnesium Carbide Clusters: MgC_2, $(MgC_2)_2$, and $(MgC_2)_4$. *J. Phys. Chem. A* **1997**, *101*, 2215–2217.

(18) Koch, W.; Frenking, G.; Gauss, J.; Cremer, D.; Sawaryn, A.; Schleyer, P. v. R. Structures, Stabilities, and Bonding in CBe_2, C_2Be, and C_2Be_2. *J. Am. Chem. Soc.* **1986**, *108*, 5732–7.

(19) Ghouri, M. M.; Yareeda, L.; Mainardi, D. S. Geometry and Stability of Be_nC_m (n = 1–10; m = 1, 2, ..., to 11 - n) Clusters. *J. Phys. Chem. A* **2007**, *111*, 13133–13147.

(20) Chen, M. D.; Li, X. B.; Yang, J.; Zhang, Q. E.; Au, C. T. Parity Alternation in the Linear Ground-State Beryllium-Doped Carbon Clusters BeC_n^- (n = 1–8). *Int. J. Mass Spectrom.* **2006**, *253*, 30–37.

(21) Lee, T. J.; Kobayashi, R.; Handy, N. C.; Amos, R. D. Comparison of the Brueckner and Coupled-Cluster Approaches to Electron Correlation. *J. Chem. Phys.* **1992**, *96*, 8931–7.

(22) Patrick, A. D.; Williams, P.; Blaisten-Barojas, E. Energetics and Bonding in Beryllium Metalized Carbon Clusters. *J. Mol. Struct.: THEOCHEM* **2007**, *824*, 39–47.

(23) Ramondo, F.; Sanna, N.; Bencivenni, L. Ab Initio Geometries and Vibrational Frequencies of Coordination Structures of Inorganic Ion-Pairs. *J. Mol. Struct.: THEOCHEM* **1992**, *258*, 361–78.

(24) Mascaritolo, K. J.; Dermer, A. R.; Green, M. L.; Gardner, A. M.; Heaven, M. C. Photodetachment Spectroscopy of the Beryllium Oxide Anion, BeO^-. *J. Chem. Phys.* **2017**, *146*, 054301.

(25) Dermer, A. R.; Green, M. L.; Mascaritolo, K. J.; Heaven, M. C. Photoelectron Velocity Map Imaging Spectroscopy of the Beryllium Sulfide Anion, BeS^-. *J. Phys. Chem. A* **2017**, *121*, 5645–5650.

(26) Leon, I.; Yang, Z.; Liu, H.-T.; Wang, L.-S. The Design and Construction of a High-Resolution Velocity-Map Imaging Apparatus for Photoelectron Spectroscopy Studies of Size-Selected Clusters. *Rev. Sci. Instrum.* **2014**, *85*, 083106.

(27) Hock, C.; Kim, J. B.; Weichman, M. L.; Yacovitch, T. I.; Neumark, D. M. Slow Photoelectron Velocity-Map Imaging Spectroscopy of Cold Negative Ions. *J. Chem. Phys.* **2012**, *137*, 244201.

(28) Dick, B. Inverting Ion Images Without Abel Inversion: Maximum Entropy Reconstruction of Velocity Maps. *Phys. Chem. Chem. Phys.* **2014**, *16*, 570–580.

(29) Peterson, K. A.; Dunning, T. H., Jr Accurate Correlation Consistent Basis Sets for Molecular Core-Valence Correlation Effects: The Second Row Atoms Al-Ar, and the First Row Atoms B-Ne Revisited. *J. Chem. Phys.* **2002**, *117*, 10548–10560.

(30) Werner, H.-J.; Knowles, P. J.; Knizia, G.; Manby, F. R.; Schuetz, M. Molpro: a general-purpose quantum chemistry program package. *Wiley Interdisciplinary Reviews: Computational Molecular Science* **2012**, *2*, 242–253.

(31) Weinhold, F.; Landis, C. R.; Glendening, E. D. What is NBO Analysis and How is it Useful? *Int. Rev. Phys. Chem.* **2016**, *35*, 399– 440.

(32) Schmider, H. L.; Becke, A. D. Chemical Content of the Kinetic Energy Density. *J. Mol. Struct.: THEOCHEM* **2000**, *527*, 51–61.

(33) Lu, T.; Chen, F. Multiwfn: A Multifunctional Wavefunction Analyzer. *J. Comput. Chem.* **2012**, *33*, 580–592.

(34) Frish, M. J.; et al. Gaussian 09, revision 1A; Gaussian Inc.: Wallingford, CT.

(35) Mayer, I.; Salvador, P. Overlap Populations, Bond Orders and Valences for 'Fuzzy' Atoms. *Chem. Phys. Lett.* **2004**, *383*, 368–375.

Chapter 7

Preliminary Work on Various Anionic Species

The work detailed in this chapter involves the anions attempted to be studied with our instrument, but could not be fully elucidated, due to various scientific hurdles. The methods for generation, and preliminary spectroscopic and theoretical work will be detailed. Also, commentary on possible future solutions is included, herein.

7.1 Beryllium Dichalcogenides, BeX_2^- (X = O, S)

Due to our new understanding of BeO^- [1] and BeS^-,[2] investigation in the beryllium dichalcogenides anions can provide insight into beryllium cluster evolution. Also, the interpretation of BeO_2 and BeS_2 molecular structure has been known to be theoretically challenging. Reactions between molecular oxygen (O_2) and beryllium are expected to lead to three different products. The first product that can be formed is a metallic superoxide ($^3A_2$), where the Be atom donates a 2s electron into the in-plane π^* orbital of the O_2, where the attraction is mainly electrostatic in nature ($Be^+O_2^-$), to form a C_{2v} molecule. The second product is another C_{2v} symmetry species, where both 2s electrons of the beryllium are donated to the O_2 ($Be^{2+}O_2^{2-}$) , resulting in a $^1A_1$ ground state. This second C_{2v} molecule is expected to have a much longer O_2 bond length, due to accommodation of the additional electron. Finally, a linear $D_{\infty h}$ structure is possible, where the beryllium is centered between the two oxygen atoms (O-Be-O). The nature of the bonding in this form lies along a continuum of bonding, between a pure ionic and covalent form of bonding. [4,5] It can be expected that BeS_2 would have the same bonding character.

The determination of the most preferential geometry has been pursued by theory and experiment, alike. [4-8] The two C_{2v} structures are simply described by a single configuration, however, the linear geometry has numerous low lying excited states, which make theoretical

interpretation difficult. At the current time, BeO_2 has been studied theoretically using coupled cluster methods and multireference methods with mixed results. [3,5,6] Additionally, BeO_2, BeO_2^-, and BeS_2 have been investigated by means of matrix isolation infrared studies. [4,7,8] Currently, there still exists a gap in knowledge in understanding of these molecules, which can be addressed using gas phase techniques, and additional *ab initio* calculations.

Before approaching the BeS_2/BeS_2^- system theoretically, it was thought to be prudent to try to determine an effective theoretical approach for the smaller, and more heavily characterized BeO_2 molecule. Of the three bonding schemes described earlier, due to beryllium's small size and tendency for covalent bonding, it is expected that BeO_2 will take on the linear structure.[3] This indicates careful consideration must be paid to the expected multiconfigurational nature. The electron affinity of BeO_2 was calculated using three different method/basis set combinations, as detailed in Table 7.1. Like BeO^- and BeS^-, a coupled cluster method (CCSD(T)) and a multiconfigurational methods (MRCI) were both employed to provide comparisons of the efficacy of the various methods. Additionally, a Hartree-Fock (HF) method was used to act as a baseline. Comparing the computational results, the HF and MRCI calculations are marginally similar, with only a difference in 7000 cm^{-1} in the computed electron affinities. However, the geometry optimization of the linear OBeO did predict uneven Be-O bond lengths, leading to a break in degeneracy. The coupled cluster calculation produced a result that was unquestionably inaccurate. This is not unexpected, upon evaluation of the T_1 diagnostic value of > 0.02, which suggest this molecule is significantly multireference, and, therefore, coupled cluster methods are not well suited for the investigation of these molecules. Differences in the RHF/aug-cc-pCV5Z calculations of the optimized geometries of BeS_2 and BeS_2^- suggested a BeS_2 electron affinity of 23318 cm^{-1}.

Table 7.1. Calculated electron affinities (EA) of BeO_2, using a Hartree Fock (HF), a Coupled Cluster with Singles Doubles and Pertubative Triples Excitations (CCSD(T)), and a Multireference Configuration Interaction (MRCI) method.

		HF/pVTZ	CCSD(T)/ aug-cc-pVQZ	MRCI/ aVTZ
BeO_2	EA (cm^{-1})	27292	150840	20167
	T1 Diagnostic	--	0.0225	--

In our studies of BeO^- and BeS^-, BeO_2^- and BeS_2^- were identified in our mass spectrum. However, when the focus of experimentation shifted to the dichalcogenides, it was found beneficial to increase the amount of oxidant in our gas source, to increase the specific signal of the dichalcogenides compared to the monochalcogenides. For BeO_2^-, a gas mix of 10% O_2 in a helium balance was used to produce significant BeO_2^- molecular signal. For BeS_2, the backing pressure of the helium buffer gas through a bomb containing CS_2 produced an increase in signal. All other experimental parameters were comparable to generation of BeO^- and BeS^-. It is important to note that higher order beryllium oxide/sulfide clusters which have been seen for neutral studies, have not yet been seen as anions in our instrument.

Given our theoretical results, the onset of photodetachment was believed to be between 20000-30000 cm^{-1} for BeO_2^- and BeS_2^-. At photon energies below 24000 cm^{-1}, no photodetachment was observed for BeO_2^-. However, BeS_2^- was found to photo-detach at this energy. Figure 7.1 shows photoelectron spectra for $BeS_2^- \rightarrow BeS_2$ at photon energies of 23696 (a) and 23980 cm^{-1} (b). The spectra for BeS_2, show a broad, mostly featureless distribution. There is

a significant increase in intensity at energies near threshold, but given the apparent shift in intensity with photon energy, this is expected to be artificial.

For BeO_2^-, onset of electron photodetachment was not apparent until photon energies closer to 30000 cm^{-1} were used. Figure 7.2 displays the photoelectron spectra of BeO_2^- → BeO_2 at different photodetachment energies. Similar to BeS_2^-, the BeO_2^- spectra did not reveal much structure. However, there are consistent features in the range of 28000 cm^{-1} to 29000 cm^{-1} evident in both traces. The feature at ~ 28150 cm^{-1} is tentatively assigned to the origin, and defining the electron affinity of BeO_2. Additionally, the feature at ~28800 cm^{-1} is similar to a predicted vibrational mode of BeO_2 (722 cm^{-1}). [4] Interestingly, when comparing the current experimental

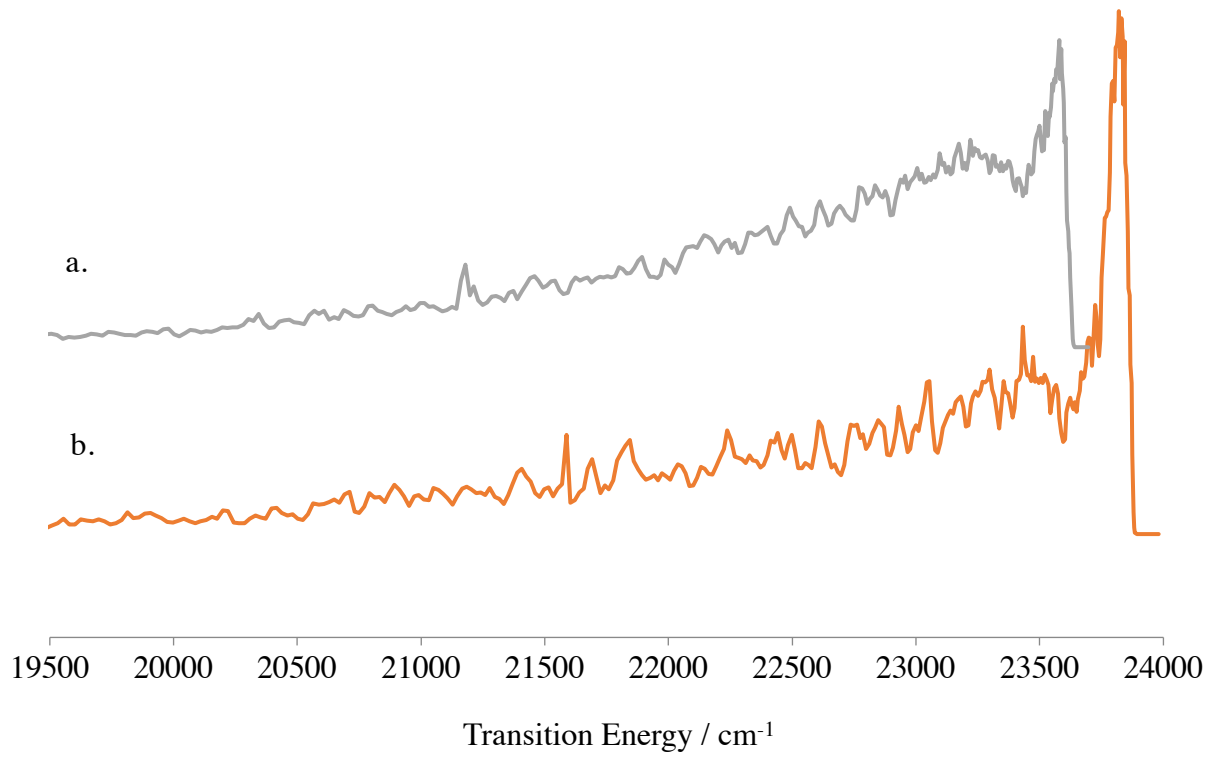

Figure 7.1. Photoelectron spectra for BeS_2^- → BeS_2 at photon energies of (a) 23696 cm^{-1} and (b) 23980 cm^{-1}.

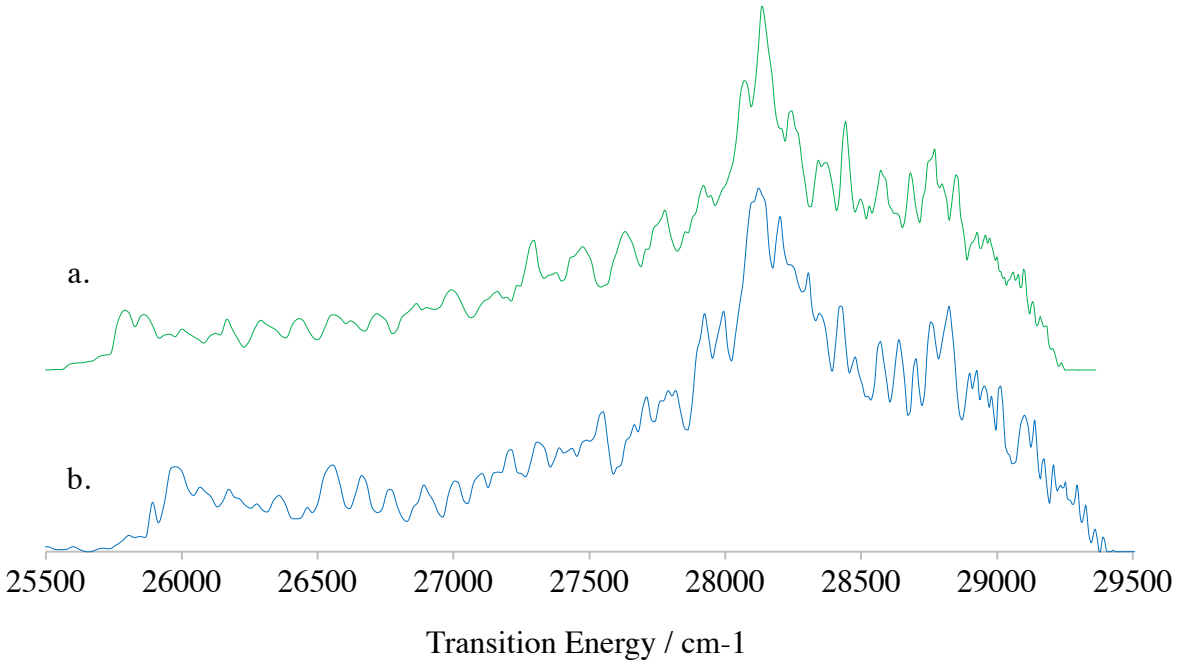

Figure 7.2. Photoelectron spectra for BeO_2^- → BeO_2 at photon energies of (a) 29363 cm^{-1} and (b) 29537 cm^{-1}.

results with our various theoretical calculations, it appears that the Hartree Fock calculation has produced the best agreement.

The lack of resolution in the spectra of these relatively small molecules is an indication of molecules that are not sufficiently cooled within our instrument. Hot band structure has been seen for all of the species we have studied, to date. Additional population in higher vibrational and rotational levels, combined with the already complicated electronic structure, due to numerous low-lying electronically excited states of linear BeO_2 and BeS_2, could be causing too much spectral congestion for our instrument to deconvolute. The addition of a cold trap could reduce vibrational population and rotational broadening enough to provide higher resolution spectra for BeO_2^- and BeS_2^-.

7.2 Beryllium Hydroxide, $BeOH^-$

The neutral BeOH is another example of beryllium's propensity to deviate from the characteristics of the other Group IIA metals.[9] The alkaline earth metal hydroxides are all predicted to all be linear systems, with the exception of BeOH, which was expected to be a bent structure. [9-12] Past experimental studies include infrared external reflection spectroscopy (ERS), [13] infrared spectroscopy in a matrix isolation , [7] and electronic spectroscopy of jet cooled BeOH, [9] but these studies did not provide confirmation of the ground state geometry. Two-color photoionization of BeOH and BeOD provided rotationally resolved spectra which did confirm the ground state geometry of BeOH as bent. [14] The $BeOH^-$ has yet to be investigated, but is expected to also be a stable bent structure. Experimental investigation of $BeOH^-$ enables to confirmation of the predicted EA (0.812 eV). [11]

In the study of neutral BeOH/BeOH by multiphoton ionization, BeOH was generated via laser ablation of a beryllium rod and a helium buffer gas seeded with nitric acid, HNO_3. [14] Nitric acid is considered a sufficient OH^- source, as HNO_3 readily decomposes to NO_2^+ and OH^-. Therefore, nitric acid was used in order to generate $BeOH^-$ with great success. However, continual flow of the strong acid through the Jordan pulse valve caused damage to the internal components of the pulse valve, leading to inconsistent pulses, and over-currenting of driver unit. Investigations into $BeOH^-$ using HNO_3 were discontinued to prevent further damage to experimental components. Other oxidant sources (H_2O and methanol) were attempted, but did not provide the necessary molecular signal required for imaging.

Before the study of $BeOH^-$ was discontinued, photodetachment of electrons was observed in an energy range near the predicted electron affinity (0.812 eV). Figure 7.3 shows the photoelectron spectra taken for $BeOH^- \rightarrow$ BeOH, in the photodetachment energy range of

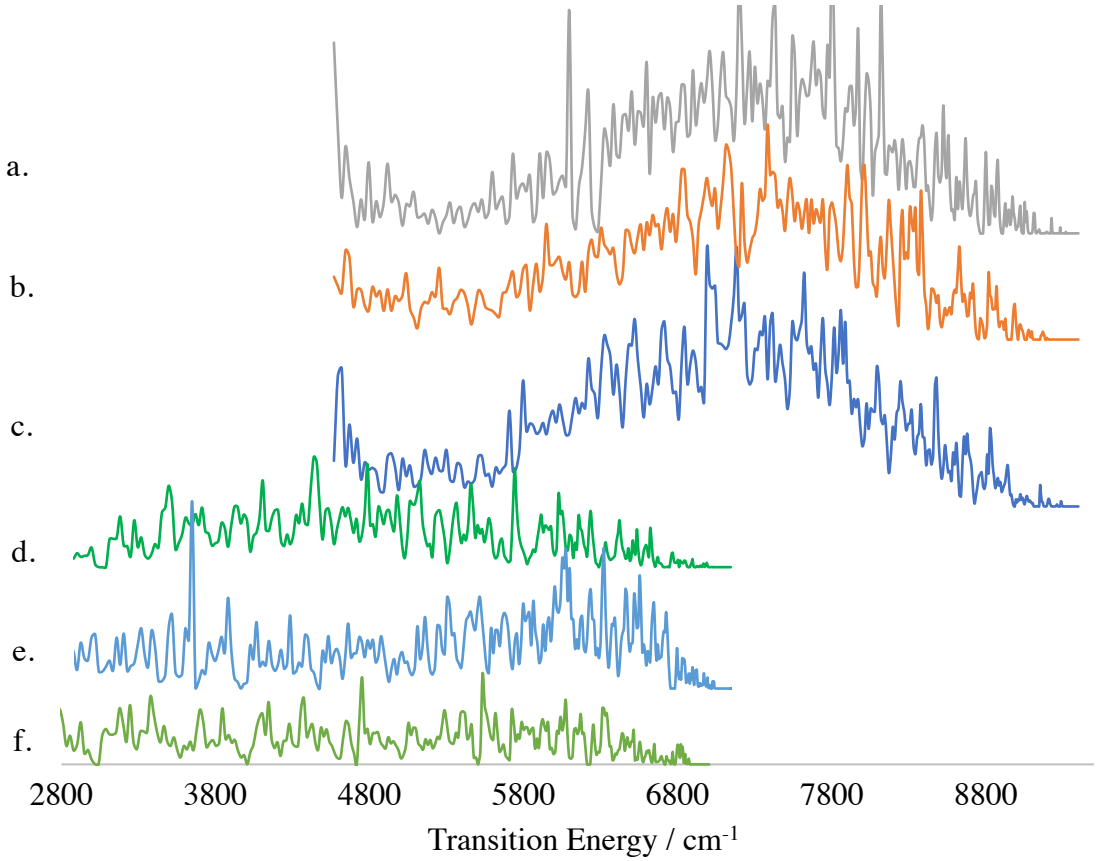

Figure 7.3. Photoelectron spectra for $BeOH^-$ → BeOH at photon energies of (a, b, c) 9398 cm^{-1} , (d, e) 7143 cm^{-1}, and (f) 7002 cm^{-1}.

7000 cm^{-1} – 9400 cm^{-1} (0.89 eV – 1.17 eV). The spectra display a broad distribution, but resolution is not high enough to see the presence of individual transitions. For example, the sharp peaks that appear in Figure 7.3a, taken at hν = 9348 cm^{-1}, are not reproduced in 7.3b, or 7.3c, which were also, taken at hν = 9348 cm^{-1}, therefore, the peaks are considered to be artificial. The lack of resolution could be an effect of a competing isomer, HBeO. Although $HBeO^-$ has not been studied, the neutral species is known to be stable, [15] leading to the possibility of two different molecules being photodetached.

The lower energy spectra had very little electron signal. This lower amount of signal could have been a result of too low of photodetachment energy employed, or could be an effect of lower initial molecular production, as these spectra were taken later in the investigation, when issues with the pulse valve were first being observed.

Continued work on $BeOH^-$ will require a softer method of anion generation, to prevent damage to the instrument. Also, given this broad structure has been present for multiple species (BeO_2^-, and BeS_2^-), further investigation into the nature of this behavior should be conducted. Although, it is expected to be associated with the inadequate thermalization of our anions, confirmation of this theory will be provided with the addition of a cooling ion trap.

7.3 Beryllium Halides

7.3.1 Beryllium Monohalides, BeX^- (X = Cl, Br)

With our discovery of dative bonding in BeF^-, [16] there was interest in examining the heavier beryllium monohalides, BeCl and BeBr, to see if this bonding character continued down the periodic table. The neutral BeCl and BeBr have been studied theoretically, [17-20] but no theoretical work has been conducted on the anions, $BeCl^-$, and $BeBr^-$. One infrared matrix isolation study has been performed to analyze the cations and anions of beryllium halides (Be+F_2 and Be+HCl), but there was no indication of $BeCl^-$ in the spectrum. [21]

Electronic structure calculations were performed to evaluate the electron affinities, anion dissociation energies and anion bond lengths of BeCl and BeBr, for comparison with those of BeF. Results of these calculations can be found in Table 7.2. For determination of the electron affinities, geometry optimizations were performed on BeBr and $BeBr^-$ using a (R)CCSD(T) methodology and B3LYP starting wavefunction, with aug-cc-pwCV5Z basis set, comparable to

Table 7.2 Electron affinities (EA), anion bond dissociation energies (D_e^-), and anion bond lengths (R_e^-) of BeX (X = F, Cl, Br). Values for EA and D_e^- are given in units of wavenumbers (cm^{-1}), and values for R_e^- are given in Angstroms (Å) .

	EA	D_e^-	R_e^-
BeF [a]	8697	28460	1.414
BeCl	9644	12640	1.920
BeBr	10359	9358	2.128

[a] Values for BeF (BeF^-) are included from Ref [16].

those used for BeF/BeF^-. In order to determine the D_e^- for $BeBr^-$, another energy calculation was conducted for a bond length of 15 Å, where $BeBr^-$ would be assumed to be dissociated. The difference in energy of $BeBr^-$ at its optimized geometry and at 15 Å, provided an estimate for the D_e^- of $BeBr^-$.

For BeCl, point wise potential energy curves for the anion and neutral were constructed using the same (R)CCSD(T)/aug-cc-pwCV5Z method and basis set, but an RHF wavefunction was used as an initial starting point for the coupled cluster calculation. For the neutral, at longer bond lengths, (R > 3.5 Å) the coupled cluster calculation would not converge. This behavior was evident for the construction of PECs for BeO^-/BeO, as well, and it is believed that implementation of the B3LYP starting wavefunction in construction of the BeCl PECs, would bypass this failure. The PECs for BeCl/$BeCl^-$ can be found in Figure 7.4. The EA_{vert} of BeCl and D_e^- of $BeCl^-$ were determined directly from the PECs.

When comparing the electron affinities of BeF with BeCl and BeBr, it is evident that the electron affinity of BeX increases as you move down the periodic table. Unlike the case of BeO and BeS, where an increase in electron affinity from BeO to BeS was attributed to the increase in elemental EA as you move down the column of the periodic table, the ordering for halogen EAs

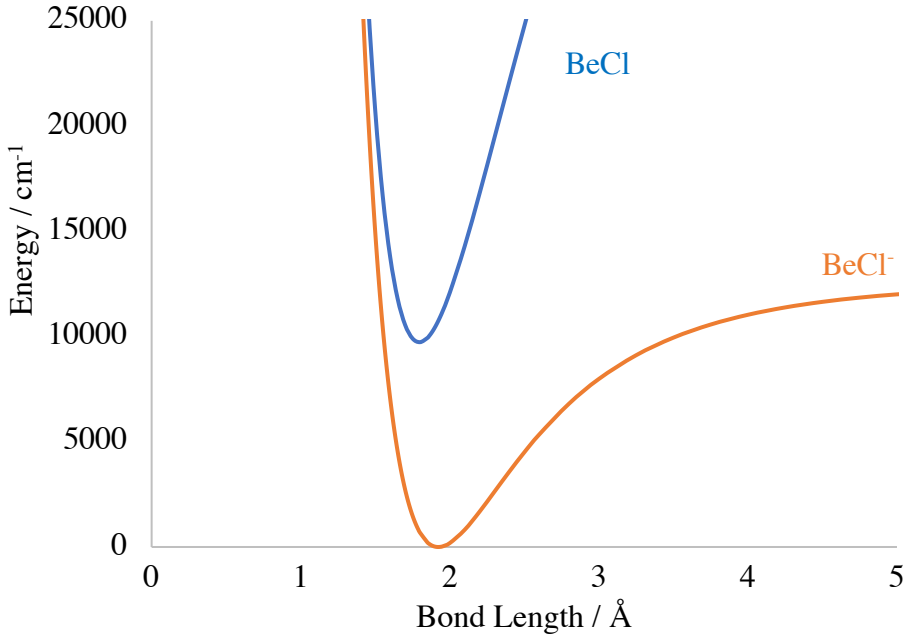

Figure 7.4 PECs for BeCl (blue) and $BeCl^-$ (orange). Note: the BeCl PEC only converged for the bond length range 0.5 Å- 3.5 Å.

does not directly correlate with atomic size. Therefore, it is interesting to still see an increase in EA as you go from BeF to BeBr.

An increase in EA for the heavier beryllium monohalides would typically indicate a higher probability of forming the anion in the gas phase, suggesting $BeCl^-$ and $BeBr^-$ could be viable targets for photoelectron spectroscopy. However, consideration must be made also to the stability of the bond upon addition of an electron. Although the calculations indicated an increase in EA with halogen size, the bond energy exhibited an opposite trend. With increasing halogen size, the bond energy for BeX grows weaker. A weakening of the bond could lead to difficulty in forming these molecules, which has been supported with the search of $BeCl^-$ in our instrument. The formation of BeF^- in our instrument is very straightforward, but creation $BeCl^-$ was attempted using various chlorine sources (chloroform, dichloromethane, benzyl chloride), with

much less production of molecular signal. Deliberate searches for $BeBr^-$ with our instrument have not been conducted, but mass calibrations conducted with bromine did not suggest the formation of $BeBr^-$ was occurring. It is expected that the dative bonding apparent with BeF^- is unique to this system as fluorine's small size allows for the effective back donation of electron density.

7.3.2 Beryllium Superhalogens BeX_3^- (X = F, Cl, Br)

Superhalogens are an intriguing class of molecules marked with very high electron affinities. A superhalogen is comprised of a metallic center, M, with a maximal formal valence, k, bound to halogen atoms, X, of the form MX_{k+1}. The resulting polyatomic species has a much higher electron affinity than its constituent halogen (MX_{k+1} EA >> X EA). Due to their high electron affinities, superhalogens can oxidize species with extremely high ionization potentials, such as O_2 and noble gases. [22,23] Additionally, they are of interest for production of superconductors. [23]

Photoelectron spectroscopy has been used to probe various superhalogens, [23,24] but no experimental studies on the beryllium superhalogens have been conducted yet. In our exploration of BeF^-, a peak consistent with the mass of BeF_3^- was evident in our mass spectrum. Also, although $BeCl^-$ was not easily generated in our ablation, there were indications that $BeCl_3^-$ was present. With optimization of ablation settings, it is possible to produce enough molecular signal to image these species.

The predicted electron affinities of BeF_3^- and $BeCl_3^-$ are 7.630 eV and 6.171 eV. [22] Photodetachment at these high energies requires the use of a F_2 excimer laser at 157 nm (7.89 eV) or an ArF excimer laser at 193 nm (6.42 eV). Propagation of light through air at these

wavelengths is minimal, due to photolysis of O_2 with high UV light. A channel that can connects the laser window to the window of the instrument chamber, which can be purged with N_2, to allow for use of these photon energies is currently underway.

7.4 Thorium Oxide Clusters ($Th_nO_m^-$)

Thorium oxides are of interest for the purpose of nuclear fuel sources. Many studies have been conducted on the smallest neutral thorium oxide, ThO.[25-28] Much of the theoretical work on the larger clusters has been avoided due to thorium's large atomic size, which requires treatment with a relativistic Hamiltonian. As such, there has been a push to apply simpler chemical bonding models to the thorium species, such as ligand field theory. [28, 29]

Although studies of neutral thorium oxide clusters are currently underway, anionic species have not been as well studied. The work conducted on the anions includes a few theoretical studies, a matrix isolation study, [30] which indicated the presence of ThO_2^- as well as photoelectron spectroscopy studies on the smallest thorium oxide anion clusters, ThO^-, [31] ThO_2^-, and ThO_3^-. [32] Here we would like to continue to search for $Th_nO_m^-$ clusters for spectroscopic investigation. Additionally, due to thorium's large mass, pursuit of these species provides the opportunity to calibrated our instrument for heavier masses, which we have yet to see with the beryllium species.

Thorium oxide clusters were generated using laser ablation of a thorium rod target, with a helium buffer gas seeded with 10% O_2. Average ablation laser settings were used, but it was found that generation of thorium oxide clusters required much earlier (~ 100 μs earlier) pulse valve timings, and higher backing pressures (65 psia). Additionally, the timing of the mass spectrometer pulses needed to be ~30 μs later in comparison to BeO^-. The resulting

mass spectrum of thorium oxide anionic clusters can be found in Figure 7.5, and a table of the labeled mass peaks is located in Table 7.3. Thorium clusters as large as $Th_9O_m^-$ were apparent in the mass spectrum. Mass resolution of the heavier peaks could be achieved with increasing the voltage difference between the MS repeller and MS extractor electrodes, and adjusting the timing difference between pulsing the voltages of the mass spectrometer electrodes.

To perform photodetachment spectroscopy on the thorium oxide clusters, photodetachment of ThO^- and ThO_2^- was attempted, first. As was previously stated, ThO^- and ThO_2^- have already been characterized by means of photoelectron velocity map imaging spectroscopy. [31,32] Comparison to previously characterized spectra would allow for the evaluation of our instrument's ability to image larger species, with more complicated electronic structure, as well as, provide confirmation of our assignment of our mass spectrum, to allow for mass calibration for heavier mass anions. Both ThO^- and ThO_2^- have been shown to have detachment transitions accessible by the fundamental (1064 nm) and second harmonic (532 nm) of a Nd:YAG laser. Therefore, photoelectron spectra were taken at these photon energies for the mass peaks tentatively assigned to ThO^- and ThO_2^-. Although photodetachment was evident at these energies, the spectra produced were unresolved, and did not match the spectra obtained by Li et. al. [31,32] Although we have already determined the anions we are producing are very hot, which could lead to spectral congestion, it is also possible that for the thorium species, different ion focusing voltages will need to be employed, to better focus the heavier beam into the interaction region of the VMI. It should be noted that energy range for a given image obtained by Li et. al. was much greater that what we can achieve with our instrument, indicating they use much higher VMI voltages.

Figure 7.5. Mass Spectrum of $Th_nO_m^-$ clusters. Peaks are labelled by their number of thorium atoms.

Table 7.3. Mass assignments for the mass spectrum shown in Figure 7.5.

Mass Spectrum Assignment	Timing (μs)	Expected Species	Mass Spectrum Assignment	Timing (μs)	Expected Species
1A	66.62	ThO	3	116.15	Th_3O_y
1B	68.65	ThO_2	4	137.09	Th_4O_y
1C	70.68	ThO_3	5	153.81	Th_5O_y
1D	74.43	ThO_4	6	169.12	Th_6O_y
1E	76.15	ThO_5	7	182.40	Th_7O_y
1F	78.50	ThO_6	8	194.58	Th_8O_y
2	94.90	Th_2O_y	9 [a]	~206	Th_9O_y

[a] Peak not shown in Figure 7.5.

When a greater voltage difference was applied to the electrodes of the mass spectrometer, separation of the individual mass peaks of Feature 2 in Figure 7.5 was possible. Upon separation, there was a prominent peak midway through the series, assigned to $Th_2O_4^-$. Stochiometric progressions of Th_nO_{2n} have been observed before experimentally, [30] and have recently been characterized by theoretical means. [33] $Th_2O_4^-$ is expected to detach between 0.8-1.15 eV, so photodetachment was performed using the fundamental frequency of a Nd:YAG laser. Also, greater VMI voltages (V_R = -725 V, V_E = -525 V) were used to capture a larger range of energies. Figure 7.6 shows the resulting spectrum obtain for detachment at 1064 nm. There is an overall broad structure, but there appears to be sharp features protruding from the broad background, indicating structure in this region. More work is currently underway to confirm the results of this spectrum.

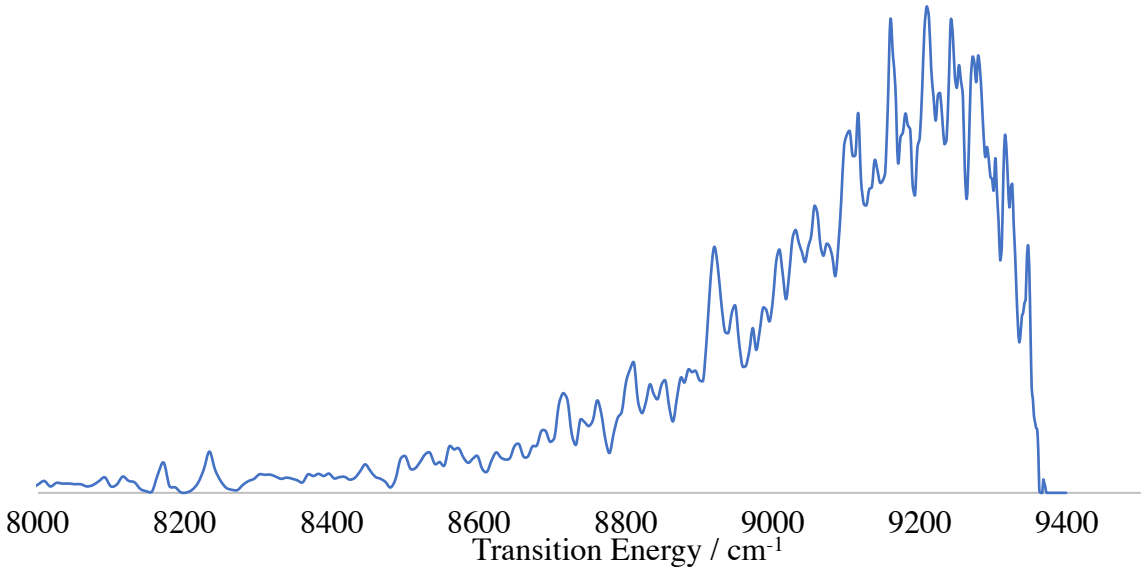

Figure 7.6 Photoelectron spectrum of the expected $Th_2O_4^- \rightarrow Th_2O_4$ transition at a photon energy of 9398 cm^{-1}.

7.5 Chapter 7 References

(1) Mascaritolo, K. J., Dermer, A. R., Green, M. L., Gardner, A. M., & Heaven, M. C. Photodetachment spectroscopy of the beryllium oxide anion, BeO^-. *The Journal of Chemical Physics*, **2017**, *146*(5), 054301.

(2) Dermer, A. R., Green, M. L., Mascaritolo, K. J., & Heaven, M. C. Photoelectron Velocity Map Imaging Spectroscopy of the Beryllium Sulfide Anion, BeS^-. *Journal of Physical Chemistry A*, **2017**, *121*(30), 5645-5650.

(3) Bauschlicher, C. W.; Partridge, H.; Sodupe, M.; Langhoff, S. R., THEORETICAL-STUDY OF THE ALKALINE-EARTH METAL SUPEROXIDES BEO2 THROUGH SRO2. *Journal of Physical Chemistry* **1992,** *96* (23), 9259-9264.

(4) Andrews, L.; Chertihin, G. V.; Thompson, C. A.; Dillon, J.; Byrne, S.; Bauschlicher, C. W., Infrared spectra and quantum chemical calculations of group 2 MO(2), O(2)MO(2), and related molecules. *Journal of Physical Chemistry* **1996,** *100* (24), 10088-10099.

(5) Charkin, O. P.; Klimenko, N. M.; Schleyer, P. V., Ab initio calculations of linear and cyclic forms of molecules and ions of MY2 dichalcogenides with 16 valence electrons. *Russian Journal of Inorganic Chemistry* **2002,** *47* (2), 231-239.

(6) Lee, T. J.; Kobayashi, R.; Handy, N. C.; Amos, R. D., COMPARISON OF THE BRUECKNER AND COUPLED-CLUSTER APPROACHES TO ELECTRON CORRELATION. *Journal of Chemical Physics* **1992,** *96* (12), 8931-8937.

(7) Thompson, C. A.; Andrews, L., REACTIONS OF LASER-ABLATED BE ATOMS WITH O-2 - INFRARED-SPECTRA OF BERYLLIUM OXIDES IN SOLID ARGON. *Journal of Chemical Physics* **1994,** *100* (12), 8689-8699.

(8) Wang, Q.; Wang, X. F., Infrared Spectra of NgBeS (Ng = Ne, Ar, Kr, Xe) and BeS2 in Noble-Gas Matrices. *Journal of Physical Chemistry A* **2013,** *117* (7), 1508-1513.

(9) Heaven, M. C., Bondybey, V. E., Merritt, J. M., & Kaledin, A. L. The unique bonding characteristics of beryllium and the Group IIA metals. *Chemical Physics Letters*, **2011**, *506*(1-3), 1-14

(10) Koput, J., Ab Initio Potential Energy Surface and Vibration-Rotation Energy Levels of Beryllium Monohydroxide. *Journal of Computational Chemistry* **2017,** *38* (1), 37-43.

(11) Kas, M.; Loreau, J.; Lievin, J.; Vaeck, N., Ab initio study of the neutral and anionic alkali and alkaline earth hydroxides: Electronic structure and prospects for sympathetic cooling of OH. *Journal of Chemical Physics* **2017,** *146* (19).

(12) Kalemos, A., The nature of the chemical bond in BeO0,-, BeOBe+, 0,-, and in their hydrogenated products HBeO0,-, BeOH, HBeOH, BeOBeH+, 0,-, and HBeOBeH. *Journal of Chemical Physics* **2017,** *146* (10).

(13) Brom, J. M.; Weltner, W., ESR-SPECTRUM OF BEOH MOLECULE. *Journal of Chemical Physics* **1976,** *64* (9), 3894-3895.

(14) Mascaritolo, K. J.; Merritt, J. M.; Heaven, M. C.; Jensen, P., Experimental and Theoretical Characterization of the 2(2)A '-1(2)A ' Transition of BeOH/D. *Journal of Physical Chemistry A* **2013,** *117* (50), 13654-13663.

(15) Zaidi, A.; Lahmar, S.; Ben Lakhdar, Z.; Rosmus, P.; Chambaud, G., Theoretical study of HBeO. *Chemical Physics* **2006,** *321* (1-2), 41-47.

(16) Green, M. L.; Jean, P.; Heaven, M. C., Dative Bonding between Closed-Shell Atoms: The BeF- Anion. *Journal of Physical Chemistry Letters* **2018,** *9* (8), 1999-2002.

(17) Wan, M. J.; Shao, J. X.; Huang, D. H.; Jin, C. G.; Yu, Y.; Wang, F. H., Laser cooling of BeCl and BeBr molecules in an ab initio method. *Physical Chemistry Chemical Physics* **2015,** *17* (40), 26731-26739.

(18) Novikov, M. M.; Tunitsky, L. N., Vibrational Constants And The Dissociation Energy Of Becl Molecule. *Optika I Spektroskopiya* **1960,** *8* (6), 752-760.

(19) de Lima, J. C. B.; Ornellas, F. R., The low-lying electronic states of BeCl: Potential energy curves, transition moments, transition probabilities, and radiative lifetimes. *Journal of Molecular Spectroscopy* **2013,** *283*, 22-28.

(20) Liu, D. M.; Zhang, S. D., MRCI calculations for BeCl electronic excited states. *Acta Physica Sinica* **2012,** *61* (3).

(21) Yu, W. J.; Andrews, L.; Wang, X. F., Infrared Spectroscopic and Electronic Structure Investigations of Beryllium Halide Molecules, Cations, and Anions in Noble Gas Matrices. *Journal of Physical Chemistry A* **2017,** *121* (46), 8843-8855.

(22) Anusiewicz, I.; Skurski, P., An ab initio study on BeX3- superhalogen anions (X = F, Cl, Br). *Chemical Physics Letters* **2002,** *358* (5-6), 426-434.

(23) Elliott, B. M.; Koyle, E.; Boldyrev, A. I.; Wang, X. B.; Wang, L. S., MX3- superhalogens (M = Be, Mg, Ca; X = Cl, Br): A photoelectron spectroscopic and ab initio theoretical study. *Journal of Physical Chemistry A* **2005,** *109* (50), 11560-11567.

(24) Wang, X. B.; Ding, C. F.; Wang, L. S.; Boldyrev, A. I.; Simons, J., First experimental photoelectron spectra of superhalogens and their theoretical interpretations. *Journal of Chemical Physics* **1999,** *110* (10), 4763-4771.

(25) Dewberry, C. T.; Etchison, K. C.; Cooke, S. A., The pure rotational spectrum of the actinide-containing compound thorium monoxide. *Physical Chemistry Chemical Physics* **2007,** *9* (35), 4895-4897.

(26) Edvinsso.G; Selin, L. E.; Aslund, N., ON BAND SPECTRUM OF THO. *Arkiv for Fysik* **1965,** *30* (4), 283-&.

(27) Edvinsson, G.; Lagerqvist, A., ROTATIONAL ANALYSIS OF YELLOW AND NEAR-INFRARED BANDS IN THO. *Physica Scripta* **1984,** *30* (5), 309-320.

(28) Kaledin, L. A.; Kaledin, A. L.; Heaven, M. C., The electronic structure of thorium monoxide: Ligand field assignment of states in the range 0-5 eV. *Journal of Computational Chemistry* **2019,** *40* (2), 430-446.

(29) Heaven, M. C., Probing actinide electronic structure using fluorescence and multi-photon ionization spectroscopy. *Physical Chemistry Chemical Physics* **2006,** *8* (39), 4497-4509.

(30) Andrews, L.; Gong, Y.; Liang, B. Y.; Jackson, V. E.; Flamerich, R.; Li, S. G.; Dixon, D. A., Matrix Infrared Spectra and Theoretical Studies of Thorium Oxide Species: ThOx, and Th2Oy. *Journal of Physical Chemistry A* **2011,** *115* (50), 14407-14416.

(31) Li, Y. L.; Zou, J. H.; Xiong, X. G.; Su, J.; Xie, H.; Fei, Z. J.; Tang, Z. C.; Liu, H. T., Probing Chemical Bonding and Electronic Structures in ThO- by Anion Photoelectron Imaging and Theoretical Calculations. *Journal of Physical Chemistry A* **2017,** *121* (10), 2108-2113.

(32) Li, Y. L.; Zou, J. H.; Xiong, X. G.; Xie, H.; Tang, Z. C.; Ge, M.; Zhao, Y. F.; Liu, H. T., Anion photoelectron spectroscopy and chemical bonding of ThO2- and ThO3. *Journal of Chemical Physics* **2018,** *148* (24).

(33) Aguirre, N.F., Julie Jung, J., and Ping Yang, P. Unraveling the structural stability and the electronic structure of ThO2 nanoclusters. *Physical Chemistry Chemical Physics*, **2020** [In Press]

Chapter 8

Dissertation Conclusions and Future Directions

In order to reveal the unique chemical bonding of beryllium containing molecules, photoelectron velocity map imaging spectroscopy was utilized to study several small beryllium-containing anions in the gas phase. In conjunction with spectroscopic exploration, high level computational methods were employed to aid in the understanding of the chemical bonding of these species, as well as, to provide comparison to experimental results, for refinement of said quantum chemical models. Many of the anions investigated, herein, were studied for the first time spectroscopically. Of the molecules characterized, previously unknown electron affinities and anion spectroscopic constants were established. Our theoretical predictions were in good agreement with our experimental results.

The study of the $X\ ^2\Sigma^+ \rightarrow X\ ^1\Sigma^+$ electronic transition of BeO^- was used to benchmark our photoelectron velocity map imaging spectrometer. The electron affinity (17535 cm^{-1} = 2.174(2) eV) and vibrational and rotational constants of BeO^- were established, experimentally, for the first time. Spectrometer resolution was such that rotational contours could be observed in our spectra. Analysis of these rotational contours for spectra of differing photodetachment photon energies revealed a dependence of electron detachment characteristics on the electron kinetic energy. For detachment near threshold, transitions involving multiple quanta changes in the rotational angular momenta were prominent. However, as the photon energy increased, increasing the kinetic energy available to the detached electron, these $\Delta N > 0$ transitions, leaving $N = 0$ as the dominant channel.

A molecular system similar to BeO^-, the $BeS^- \rightarrow BeS$ ($X\ ^2\Sigma^+ \rightarrow X\ ^1\Sigma^+$) transition was studied for the purpose of establishing periodic trends. The established electron affinity of BeS (18,830(17) cm^{-1} = 2.3346(2) eV) was higher than the EA of BeO (2.174(2) eV), which is expected to reflect the greater EA of S. A strong feature was observed in the $\Delta v = -2$ band was

attributed to dipole bound excited state of BeS^-. Autodetachment spectroscopy revealed that the DBS was located 141 cm^{-1} below the electron detachment threshold. A similar state was, also, observed for BeO^-.

The beryllium fluoride anion, BeF^-, demonstrated the unusual behavior of beryllium to participate in bonding of closed shell atoms. Although Be ($^1S_0$) and F^- ($^1S_0$) are considered closed-shell, they form a strong bond, D_0^- >28460 cm^{-1}. Electronic structure calculations show donation of F 2p electrons into a Be 2s/2p hybrid orbital, to form a dative bond. The formation of this molecule is very unique, as other molecules of its isoelectronic series, BeNe and BNe^+, only show weak van der Waals attractions. Additionally, the electron affinity of BeF (8697 cm^{-1}) is much lower than the EA of either BeO or BeS.

Of the anions discussed within this dissertation, BeC_2^- was the only triatomic species where resolved spectra could be obtained. We confirmed previous theoretical studies, in the assignment of the structure of BeC_2 to be T-shaped, with a polar covalent bond between Be and C_2. The structure of the anion was also found to be T-shaped, resolving a previous disagreement between predictions. Similar to BeO^- and BeS^-, accommodation of the additional electron in BeC_2^- is centered on the beryllium atom, and the addition of the electron leads to a weakening of the Be-X (O, S, C_2) bond, in the anion.

Many other small anions were explored using this spectrometer, but produced results with limited resolution. Due to the presence of hot vibrational structure in the species that were elucidated, it is expected that high thermal population could be inhibiting spectral resolution of these species. Addition of a cooling ion trap should allow for further studies of small beryllium anions, beryllium clusters, and other abnormal metallic species.